AN ABSTRACT OF THE THESIS OF

Hamad A Al Tuaimi for the degree of Master of Science in Electrical and Computer Engineering presented on March 14, 2005.
Title: Detection of Incipient Rotor Bar Faults and Air-Gap Asymmetries in Squirrel-Cage Motors Using Stator Current Monitoring.

Abstract approved:

Annette von Jouanne Alan K. Wallace

Preventative motor fault detection is of prime importance for modern plant management. During research into rotor faults, performed at the Motor Systems Resource Facility (MSRF), an optimized rotor fault detection and classification method was proposed.

In critical process applications, the suggested method would provide the foundation for continually monitoring a machine in a noninvasive way and enhancing the ability of maintenance systems to identify impending rotor failures. This would then drive maintenance schedules more efficiently since the diagnosis data can be made available to a conventional operator interface station over an open network. With the advent of a current signature analysis algorithm, many industries will be driven toward on-line, noninvasive diagnostic solutions.

The proposed method can provide the information to diagnose problems accurately and quantitatively using motor dynamic eccentricity sidebands as a universal rotor fault detection and classification index. Also, related research into the effects of rotor fault isolation from load torque will enable a determination of the relative severity of a broken rotor bar or any type of air-gap asymmetries.

The objective of this work is to implement a proof of concept laboratory test of the suggested method. Three induction machines were tested on a dynamometer at twenty-eight loading points and different source and load conditions, verifying detection accuracy of the implemented technique.

Detection of Incipient Rotor Bar Faults and Air-Gap Asymmetries in Squirrel-Cage Motors Using Stator Current Monitoring

by
Hamad A Al Tuaimi

A THESIS

Submitted to

Oregon State University

In partial fulfillment of
the requirement for the
degree of

Master of Science

Presented March 14, 2005
Commencement June 2005

ACKNOWLEDGMENTS

I would like to express my sincere gratitude to my co-major professors, Alan K. Wallace and Annette von Jouanne for their encouragement and guidance throughout the study. I also would like to thank my minor professor, Lawrence S. Marple, for his valuable contribution. A special thanks goes to Manfred Dittrich, a developmental engineer from ECE, for his help during the experimental stage of this work.

I wish to thank my company, Saudi Aramco for sponsoring my study program. Special thanks are due to my department Consulting Services Department (CSD) for their continuous support. My special thanks and appreciation goes to my CSD colleagues, Majed M. Al Hamrani and Dr. Mansour Sultan, for their inspirations and useful advice.

Appreciations go also to my research team members, Ghassan A. Bin Eid and Ali S. Al Shahranni from Saudi Aramco Company, not only for their partnership in this study but for their friendship in the course of development of this thesis.

Finally, I would like to thank my career development advisor, Adnan S. Jamal from Aramco Services Company and his colleagues, for granting the support for the equipment of this research.

Table Of Contents

Table Of Contents (Continued)

List Of Figures

List Of Figures (Continued)

List Of Figures (Continued)

List Of Figures (Continued)

List Of Figures (Continued)

List Of Tables

Detection of Incipient Rotor Bars Fault and Air-Gap Asymmetries in Squirrel-Cage Motors Using Stator Current Monitoring

1. Introduction

1.1. Relevance of on-line condition monitoring and predictive maintenance

There are many initiatives in progress toward a motor/drive diagnostic system that will optimize electrical system automation and particularly enhance motor and drive fault determination. This research system will provide the foundation for advanced condition-based maintenance (CBM). Another objective is to realize a power system that can anticipate problems and quickly recover from disruptive events.

Substation automation is a new challenge for many petrochemical plants and similar high-volume, high-cost processing facilities. The ultimate goal of this research is to enhance electrical substation automation and to utilize the recent standards of substation Ethernet communication. Additionally, it seeks opportunities to implement an on-line diagnosis system utilizing the existing electrical infrastructure and to implement a cost-effective system design that will contribute to substation automation.

Monitoring three-phase induction machines via more effective techniques can promote the newly evolved predictive maintenance. This will provide opportunities to overcome the barriers to CBM, namely the inability to continually monitor a machine in a noninvasive way, and to eliminate the lack of maintenance systems to learn and identify impending motor failures and then recommend what action should be taken.

Fig.1.1 depicts the relative induction motor (IM) fault incidences. Early detection of those various induction machine faults and the provision of useful diagnostic information requires easy and quick access to machine-monitored quantities. Success will consequently facilitate efficient signature analysis without any limitation on motor location or size.

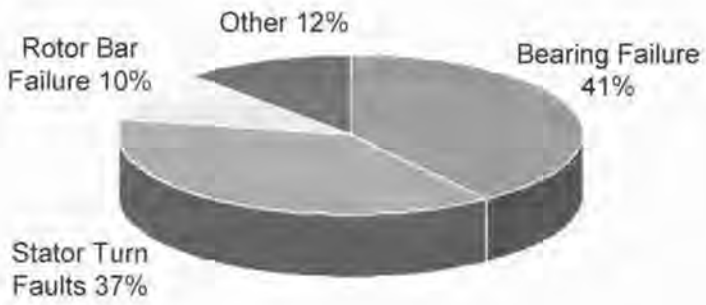

Fig.1.1: Relative IM fault incidences.

1.2. Function of the fault detection and classification system

A fault can be regarded as (or result in) the abnormal behavior of a machine. In general, incipient fault detection and classification systems carry out the following tasks:

- *Fault detection*: The process of pinpointing anomalous situations in the monitored machine.
- *Fault classification*: The process of determining the exact location and severity of the fault. In many situations, "diagnosis" is used as a synonym to "classification."

High-quality fault detection and classification systems for three-phase IM's should consider some important features, as shown in Table 1.1. The table lists these elementary features based on a distinction between high and low inertial applications and against design and data processing parameters.

Table 1.1
Features of effective motoring and diagnosis fault systems based on machine size as functions of design and data processing parameters

	Large-size machines (High inertia application)	**Small-size machines** (Low inertia application)
Load spectral content and inertial damping	Damp load effects and magnify broken bar torque pulses.	Do not damp load effects and magnify broken bar speed ripples.
Slip values	Typically operate with small slip values that require high spectral resolution.	Typically operate with larger slip values that require less spectral resolution.
Frequency range monitoring	Monitor fault frequencies sufficiently at both low and high harmonic components.	Monitor fault frequencies sufficiently at low harmonic components.

	General Requirements (regardless of size and inertia)
Design parameters	Should eliminate any dependence on knowledge of motor parameters.
High sampling frequency	Maximize the cancellation of load torque effect from the monitored quantities.
Three-phase current monitoring versus one-phase	Three-phase current monitoring to enable load torque isolation compared to single-phase monitoring.
Three-phase voltage monitoring	Three-phase voltage monitoring to enable load torque isolation and/or to verify integrity of source voltage.

1.3. Literature survey and previous works

Rotor fault Detection, fault severity and removal of load effects from the monitored quantity:

Cruz and Cardoso [1] used the total instantaneous power spectral analysis for diagnosing the occurrence of rotor cage faults in induction machines. Their experimental and simulation results show that rotor cage faults can be effectively detected by the identification of a characteristic component in the total instantaneous power spectrum at a

frequency of *2sf,* where s is the motor slip ($=\frac{N_s - N_r}{N_s}$) and *f* is the applied stator frequency. They demonstrated that the amplitude of this characteristic component is directly related to the amplitude of the two motor current spectral components, at frequencies of $(1 \pm 2s)f$. Due to the relationship between these motor current spectral components and the motor-load inertia, the characteristic component of the total instantaneous power already incorporates the effect of this parameter in the diagnostic process. A normalized severity factor, defined as the ratio of the amplitude of the *2sf* component and the DC level of the total instantaneous power, proves to be a good indicator of the extent of the fault since it takes into account the influence of parameters such as the magnetizing current, motor rating, and the motor-load inertia. However, this fault indicator is not a fully independent index from any induced load torque oscillation.

Kral and Pirker [2] compared the torque values from the voltage model and current model respectively. The voltage model evaluates the voltage and current space phasors, whereas the current model processes the current space phasor in the rotor reference frame. The transformation of values from the stator to the rotor fixed reference frame is performed with the help of instantaneous rotor position. For the conventional Vienna Monitoring Method (VMM) rotor position has been measured, while the sensorless approach presented in this contribution estimates the rotor angle. The torque values are measured according to the double slip frequency modulation of the shaft torque - caused by the rotor fault – which presents a reliable and load-independent rotor fault detection scheme without a position sensor. However, applicability of this method depends on the operating range of load torque.

Schoen and Habetler [3] suggested a model reference estimation for removing the load effects from the monitored quantity of the induction machine. Fault conditions in induction machines cause the magnetic field in the air-gap of the machine to be nonuniform. This results in harmonics in the stator current of the motor which can be measured in order to determine the health of the motor. However, variations in the load torque which are not related to the health of the machine typically have exactly the same effect on the load current. Previously presented schemes for current-based condition monitoring ignored the load effect or assumed it is known. Therefore, a scheme for

determining machine health in the presence of a varying load torque requires some method for separating the two effects. Schoen and Habetler accomplished that by measuring the three-phase currents and voltages of the machine instead of just a single phase of the stator current. The additional information provided by these measurements allowed for the estimation of the *d-axis* current of an ideal machine operating under the same load conditions. When this estimated value is subtracted from the actual measured current, the resulting spectrum (the "difference current") contains only the fault-induced portions. This improved spectral representation increases the ability of any system that utilizes the current spectrum to detect an incipient fault condition by emphasizing the changes produced by a fault anomaly. Their simulation and experimental results showed the effectiveness of this model reference estimation scheme at removing the load torque effects from the monitored spectra and illustrated the feasibility of the proposed system. They demonstrated that the characteristic spectral components are present in the difference current and that the load effects can effectively be removed from the monitored spectrum to improve their detectability. However, the synchronous reference frame transformation they used is generally avoided due to its inherent integration errors.

Long Wu et al. [4] suggested another model reference estimation for separating load torque oscillation and rotor fault effects in stator current-based motor condition monitoring. They developed a simplified method to detect rotor faults effectively in the presence of a load torque oscillation by utilizing a new fault frequency reference frame. This state-of-the-art initiative optimizes the process of fault severity evaluation and eliminates any integration errors that arise from a flux-oriented synchronous reference frame. Their simulation of a two-pole induction machine provides a discernible and reliable rotor fault indicator. This indicator is crucial to separating the interaction between the negative-sequence harmonics from rotor faults and the positive-sequence harmonics from a load oscillation.

Fault classification:

Hajiaghajani [5] derived a fuzzy logic Baysian classifier for the purpose of diagnosing rotor bar faults. It is the ratio of the integral of a window around the broken

bar harmonic to that obtained from the fundamental. Also, another classifier feature has been derived from the induced slot harmonics that occur due to rotor or stator asymmetries and from an eccentric harmonic near *(2-s)f*. This feature respectively determines rotor speed and diagnoses rotor eccentricity.

1.4. Research objectives and contributions

The primary goal of this research is to seek a reliable and pure surveillance technique for rotor faults and to decide which anomaly behavior is of concern. This result can mandate maintenance scheduling in a predictive manner and effectively implement a condition-based maintenance (CBM) tool for three-phase IM. Practically, detecting a precise characteristic spectral component is the key element in the fault detection and classification/diagnosis processes. The measure of fault severity independent from any arbitrary supply or load conditions, is vital and is the primary focus of this research.

This thesis suggests a universal rotor fault index, that utilizes the dynamic eccentricity sideband behavior that results from machine incipient rotor faults and which also occurs during precisely maintained loading points. This will ensure exact fault detection and classification accuracies.

There are many factors that complicate any fault prediction scheme. Torque oscillation, speed ripple, inertial damping effects, load spectral content, source unbalances and loading level conditions are well-known factors that can heavily impact fault detection accuracy. In this research, load torque effects on the stator current spectrum will be analyzed. Also, separation methods of fault and other external no-fault related effects due to supply and load effects in the stator current spectrum will be thoroughly investigated.

This research aims to:

- Study and simulate rotor bar defects, air-gap anomalies and arbitrary supply and load condition effects and behaviors.

- Implement an accurate speed estimation technique using a current signature method.
- Extract a universal rotor fault index using dynamic eccentricity sidebands.
- Extract a reliable and pure (supply and load independent) rotor fault severity indicator utilizing the mean negative-sequence components of the stator current aligned with the *d-axis* as a rotor fault indicator filtered from load fluctuations.
- Implement and evaluate an on-line rotor fault detection, separation and classification system.

2. Rotor Failure Investigations

2.1. Broken rotor bar fault

2.1.1. Analytical background

Large-size cage motors are manufactured from copper rotor bars and end-rings, while small-size cage motors are typically manufactured by using die-cast aluminum technology. Manufacturing die-cast rotors can raise several technical problems, such as rotor asymmetry and melting of bars and end-rings. Nevertheless, failure occurs in copper rotor bars due to many reasons. When the bar is smaller than the slot, slot harmonics will appear that consequently cause radial movement of the bar, especially during starting, which can lead to weakness or breaking of the bar. Thermal stress is another problem, occurring when the bar cannot move longitudinally in the slot. Also, motor overloading or an excessive number of consecutive direct on-line starts which develops large currents, resulting in large mechanical and thermal stress that can affect not only the rotor but also the stator through rotor-stator rubbing.

Bar failure mechanisms involved in producing current sideband frequencies are complex. Fig 2.1 shows broken bar sidebands. At low voltage or very high inertia, the lower sideband at frequency (f_s - f_{sb}) dominates due to torque ripple produced by the defective bar. At high voltage or low inertia, the upper sideband at frequency ($f_s + f_{sb}$) dominates due to speed ripple produced by the defective bar. Air-gap space harmonics can develop the upper sideband, namely the third time harmonic flux, due to tooth or core saturation. Some experiments suggest that both sidebands will be affected by speed ripples [6]. Vibration frequencies around the fundamental frequency can cause confusion with upper and lower sidebands if the slip frequency is not known. Testing the motor at various loading points can help in diagnosing the real situation of the rotor bars since vibration sidebands will not have any frequency movements due to load variation.

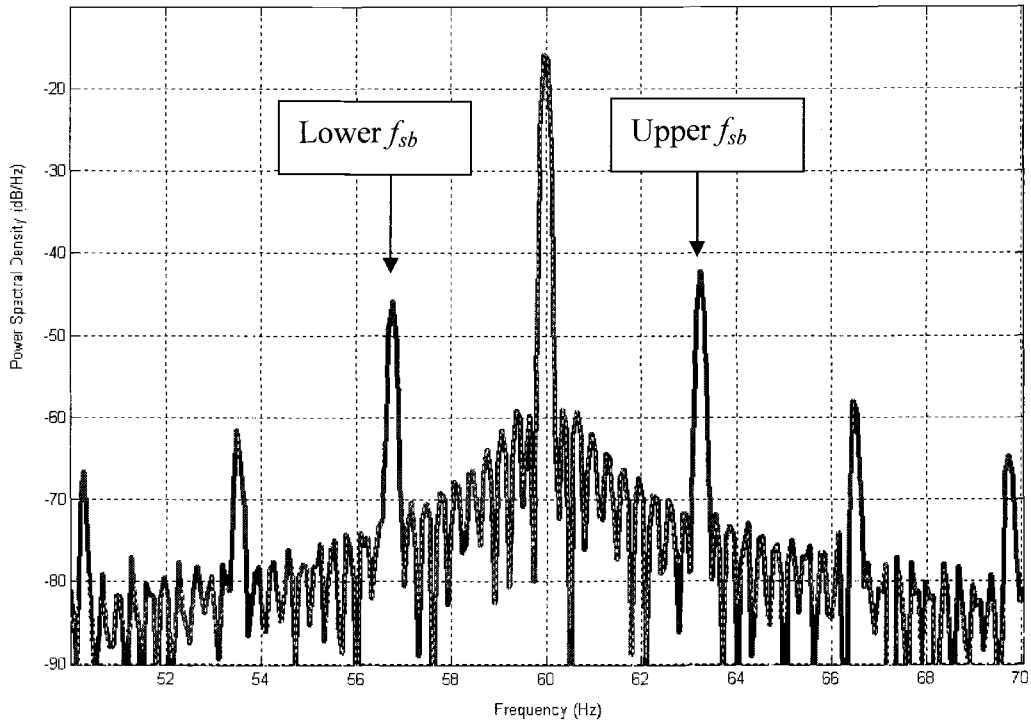

Fig. 2.1: Upper and lower broken bar sidebands

In this section, the nature of sideband frequency will be explained mathematically and physically. Sideband frequency is sometimes referred to as Pole Pass frequency [7] by condition monitoring practitioners; however, the term "sideband frequency" will be used in this research to eliminate any confusion.

Mathematically, the sidebands of a broken rotor bar can be explained by the amplitude modulation:

$$i_s = I\cos(2\pi f_s t) * \cos(2\pi f_{sb} t) \qquad (2.1)$$

The trigonometrical relationship *cos u*cos v = ½ [cos (u+v) + cos (u-v)]* shows frequency components at ($f_s + f_{sb}$) and ($f_s - f_{sb}$) as in (2.2).

$$i_s = I/2\left[\cos 2\pi t(f_s + f_{sb}) + \cos 2\pi t(f_s - f_{sb})\right] \qquad (2.2)$$

where i_s is the instantaneous stator current, I is the peak value of the stator current, f_s is the stator or supply frequency and f_{sb} is the sideband frequency due to the broken bar. The (2.2) relation proves that, conceptually, every two identical sideband harmonics associated with one or more broken rotor bar are equal in magnitude. However, this is not the situation in practice. The sideband frequencies can also be seen around other negative-sequence harmonics, like the 5th, 11th, 17th, 23rd, etc., which rotate counter to the fundamental frequency.

The physical behavior of a broken rotor bar can be explained by analyzing the rotor torque, which is physically produced by two equal and opposite tangential forces 180-degrees apart on the rotor shaft. In a normal rotor, there is no net radial force produced by these factors, since they are equal and opposite. However, the broken bar is incapable of producing torque, so the bar 180 degrees across from the broken bar has a tangential force which is not radially balanced by an equal and opposite tangential force at the position of the broken bar. The net result is a radial force (in addition to torque). The magnitude of that radial force changes at *2sf* as that 180^{O}-opposite bar moves in and out of the air-gap field. The direction of that radial force changes at f_s as the rotor rotates. By considering the tangential direction to a rotor, the result in (2.1), the $\cos(2\pi f_s t)$ component comes from consideration of the tangential component of rotating radial force. The $\cos(2\pi f_{sb} t)$ comes from the 180^{O}-opposite bar passing in and out of the field. This time pattern results in the frequencies ($f_s + f_{sb}$)and ($f_s - f_{sb}$).

As discussed, the defective bar is not capable of producing torque but the intact bars contribute their torques to the shaft with a torque equal to the summation for all N rotor bars [8]:

$$T = \xi \sum_{i=1}^{i=N} sA^2 k_i \left(1 - \cos(4\pi st + \frac{4i\pi p}{N})\right) \qquad (2.4)$$

where $k_i = 1$ if the bar is intact, $k_i = 0$ if the bar is broken (open-circuited), ξ is a proportionality constant, s is the slip, A is the magnitude of the magnetic field, p is the number of pole pairs and N is the total number of rotor bars.

In practice, bars adjacent to the broken bar carry more current than normal which also increases the degree of asymmetry in the air gap flux and basically induces more mechanical stress on those bars. Fig. 2.2 depicts the backwards flux field, which rotates at a frequency equal to $-sf_s$ with respect to the rotor frequency. The severity of failure will be increased when the opposite flux path increases due to the excessive current flowing in the adjacent bars.

Negative-sequence current due to rotor bar defects can equally be seen at the lower and upper sideband components around the fundamental frequency, shifted by $2sf_s$ as will be shown in the next section.

Tensional asymmetries created by the uneven distribution of current, as in Fig. 2.3 (b), affect the pattern and amplitudes of the line frequency harmonics and sidebands present in the current signatures. High resistance joints and cracked shorting rings (end rings) can have a similar, though usually much less pronounced, effect since the asymmetry level of any of these factors can be quite low.

The broken bar different reactions will be discussed in the next experimental section.

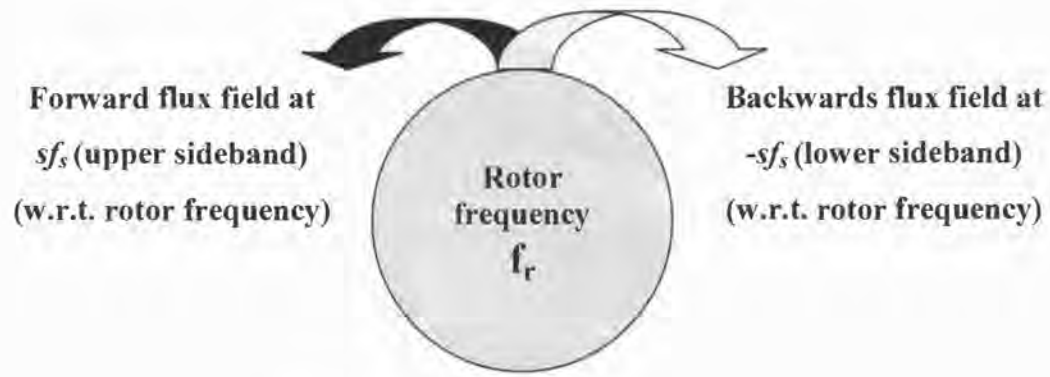

Fig. 2.2: Flux wave directions

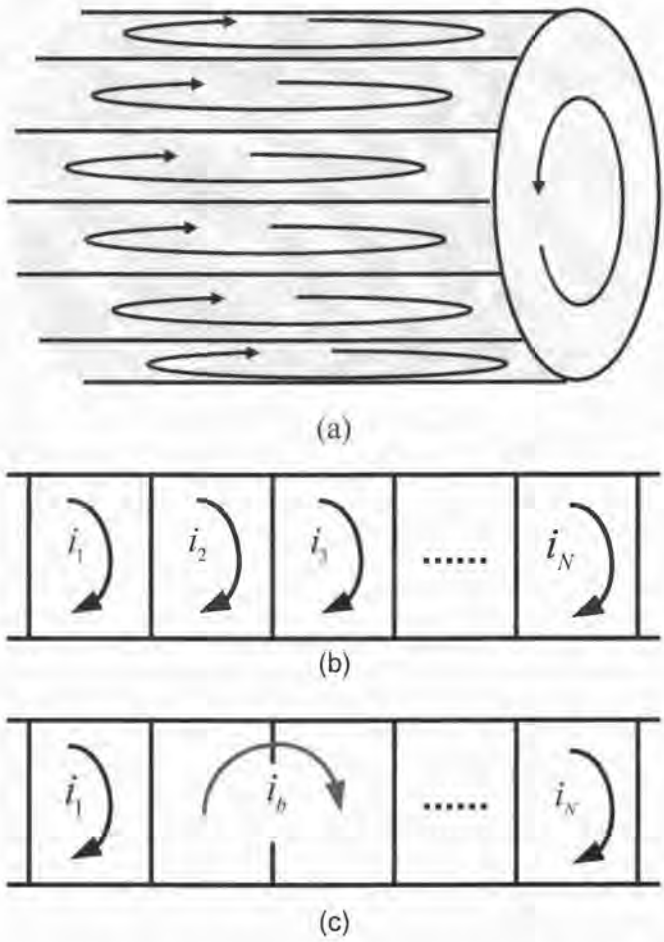

Fig. 2.3: (a) rotor current loops, (b) circuit representation of healthy rotor bars, and (c) one broken rotor bar

2.1.2. Experimental results

Broken bars of the rotor can be detected by monitoring the ratio of the amplitude of abnormal frequency to the fundamental frequency. The amplitude of abnormal frequency varies with the number of broken bars. The accuracy of the detection process can be optimized by capturing the relative fault frequencies at rated loading level, since the detection of sidebands at no-load is not possible because the current in the rotor bars is negligible. However, this section includes experimental results that investigate the possibility of detecting bar defects at about 30% of machine rated full-load. A correction factor has to be applied to estimate the number of broken bars when the motor is

operating at a reduced load [7]. Different tests have measured the sideband amplitude rate of change as a function of the machine loading level. This broken bars experiment simulated and detected four adjacent broken bars. Fig. 2.4 shows the rotor of the IM that was used for this experiment. The fault simulation is based on drilling one hole in a bar in order to vary rotor resistance and have the same symptoms as a real broken rotor bar in a large-size IM. Four adjacent broken rotor bars (out of a total of 42) were created in the Toshiba motor of specification as illustrated in Appendix A.

Knowing that broken rotor bars and end rings give rise to fault specific harmonic components (sidebands at f_{sb}) in the current spectrum at a respective frequency distance from the fundamental (frequency f_s) that is twice the slip frequency (slip s):

$$f_{sb} = (1 \pm k2s) f_s \qquad (2.5)$$

The broken bar sidebands are occurring at descending and ascending rates with respect of the fundamental frequency as shown in Fig 2.5. The lower sideband at 57.6 Hz is the so-called broken bar harmonic, which is mainly used for broken bar fault detection.

Fig. 2.6 depicted a pool of spectral data for different load conditions varying from 30% to 120% of the nominal load. This test verifies that the possibility for detecting bar defects is limited by machine loading. It shows that 30% of rated torque is the minimum loading point possible to enable rotor bar fault detection as will be proved by Fig. 2.7. [7] suggested a correction factor that has to be applied to estimate the number of broken bars when the motor is operating at a reduced load.

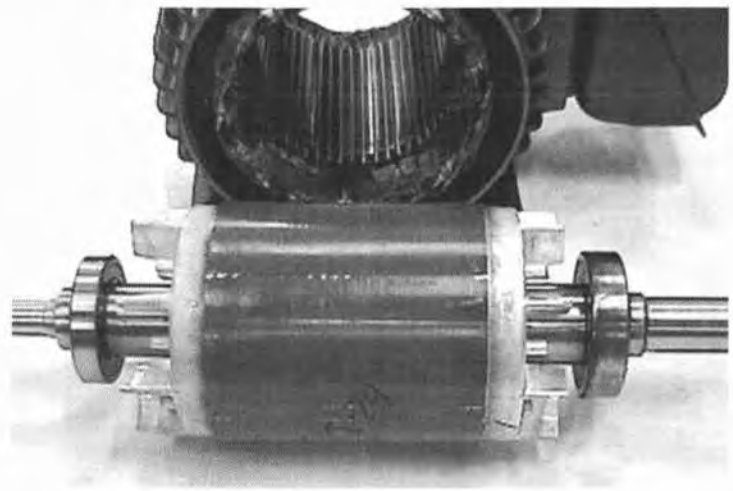

(a)

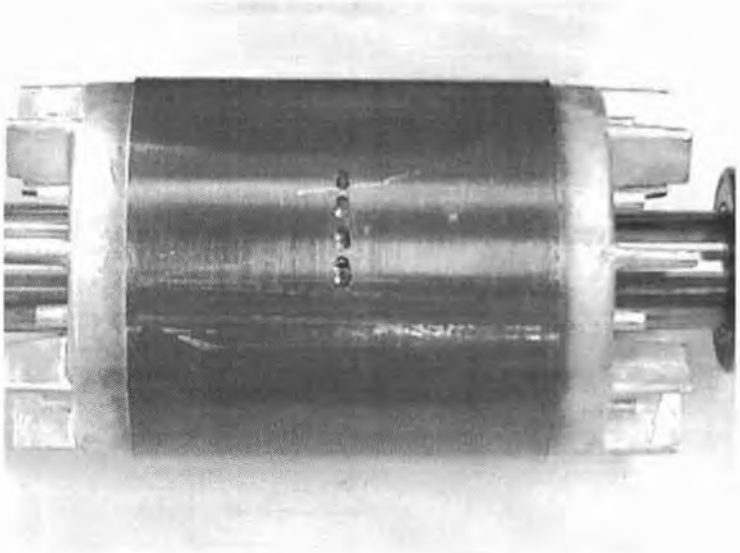

(b)

Fig. 2.4: (a) The IM being used for this experiment
(b) The broken rotor bars

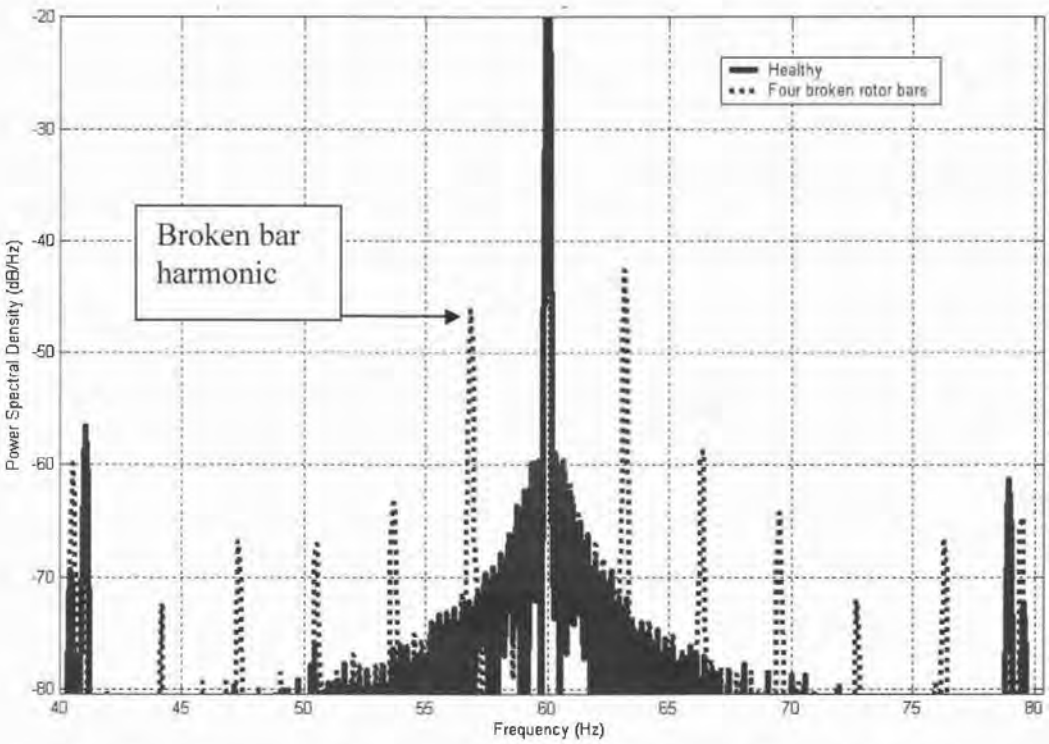

Fig. 2.5: Power spectrum density of broken bar sidebands around the fundamental frequency

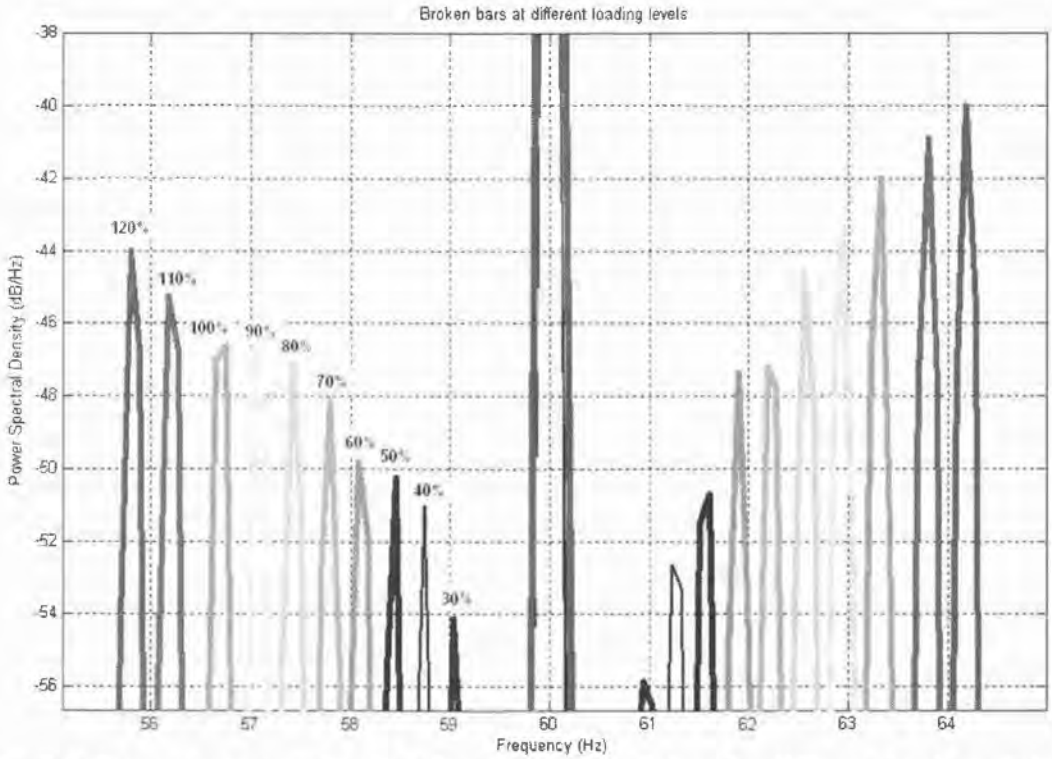

Fig. 2.6: Power spectrum density of pool of Spectral data for different load conditions varying form 30% to 120% of the nominal load

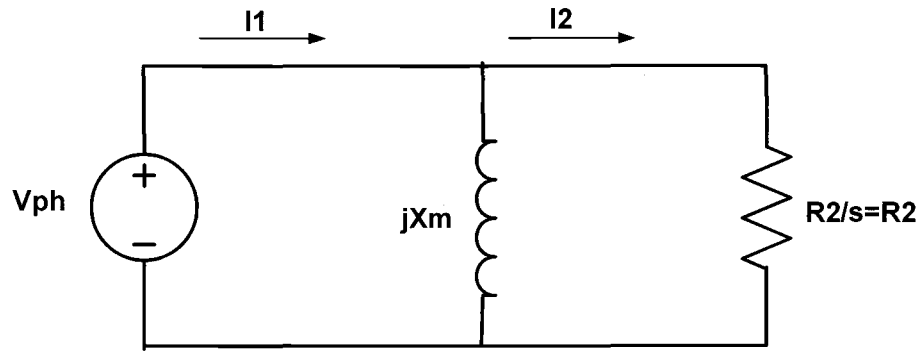

Fig. 2.7: Motor per-phase equivalent circuit

The dependency of bar fault detection on the level of machine loading can conceptually be explained by considering the IM to consist of only two parallel impedances driven by a voltage source (V_{ph}) as in Fig. 2.7. The rotor resistance ($R_2 = 2.217\Omega$ for the tested motor) has been calculated via the test sequence given in appendix A,. The in operation effective rotor resistance is inversely proportional to slip value. Therefore, the effective rotor resistance at full-load slip is equal to 82.11 Ω (= R_2/full load slip), and this is the optimum value for detecting any impeding rotor bar breakage in the tested motor. The minimum effective rotor resistance for that purpose is at 30% loading point that is equal to 267.11 Ω (= R_2/30% load slip). Since rotor resistance is a function of slip value, the higher resistance value means that the created rotor MMF wave is of small amplitude, negating the capture of an effective stator current sideband.

Interestingly, the current through the mutual inductance path is not affected by slip (or vice versa). The implication is that the field would have the same orientation and magnitude on-load as with no-load (analogous to a transformer). While the motor is running on-load, the slip value increases, making the rotor impedance smaller and drawing more current through the rotor branch of the equivalent circuit. However, the field produced by the extra stator current is cancelled out by the reaction field from the equal and opposite currents induced in the rotor.

In the air-gap, MMF produces a predictable stator current due to the broken rotor bar at the following frequencies:

$$f_{brb} = f_s\left[k\left(\frac{1-s}{p/2}\right)\pm s\right] \qquad (2.6)$$

where f_{brb} is the broken rotor bar frequency, f_s is the stator frequency, $k/(p/2)$ = 1,5,7, 11, 13, ..., and p is the number of motor poles. The tested motor operates at a slip equal to about 2.75% at full-load speed 1167 rpm, therefore the set of predicted frequencies are as shown in Table 2.1 and Fig. 2.8.

Table 2.1
Broken bar sidebands around slot harmonics (slip = 0.027, poles = 6)

$k/(p/2)$	f_{brb} (Hz)	
1	60	57.6
5	295.2	292.8
7	412.8	410.4
11	648	645.6
13	765.6	763.2
17	1000.8	998.4
19	1118.4	1116
23	1353.6	1351.2
.....	.....	.....

Generally, a less than 50% difference between fundamental and sideband frequencies requires careful monitoring due to the appearance of potential failure symptoms, with special concern needed when the difference keeps decreasing with time. In that case, corrective action should be made.

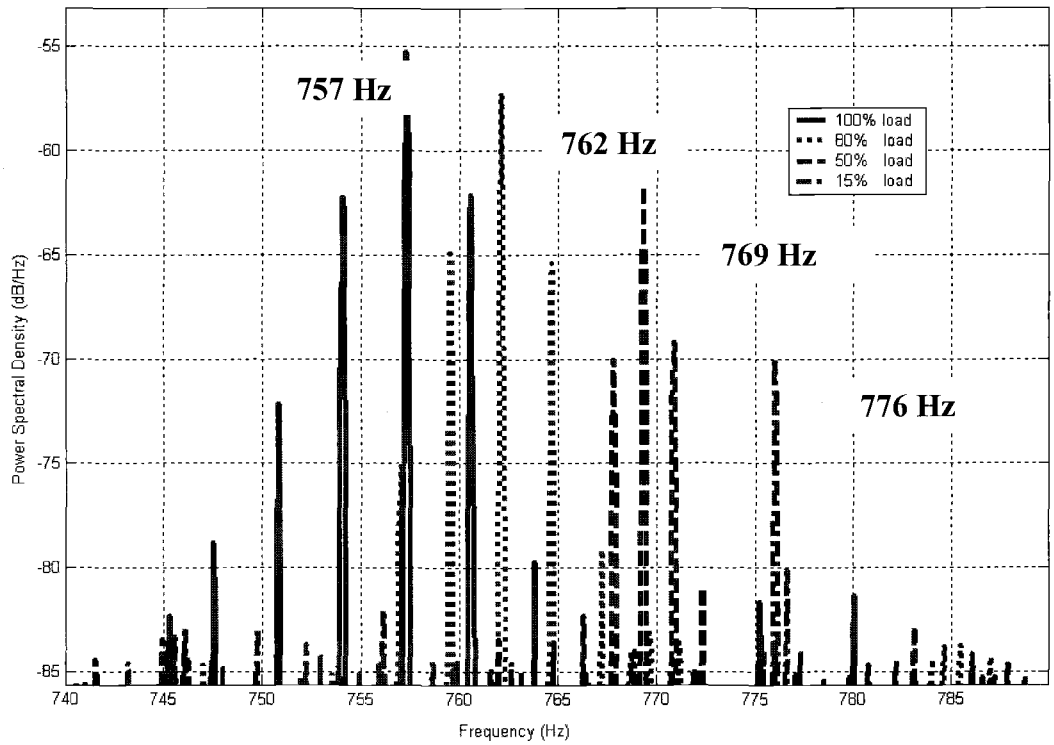

Fig. 2.8: Example of broken bar sidebands around slot harmonic at different loading points where k/(p/2) = 13

An estimate of the number of broken bars (the broken bar factor) can be obtained from the following equation [7]:

$$n = \left\lceil \frac{2R}{10^{N/20} + p} \right\rceil \qquad (2.7)$$

where n is the estimate of broken bar numbers, R is the number of rotor slots, N is the average dB difference between the lowest sideband components and the supply frequency component, and p is pole pairs.

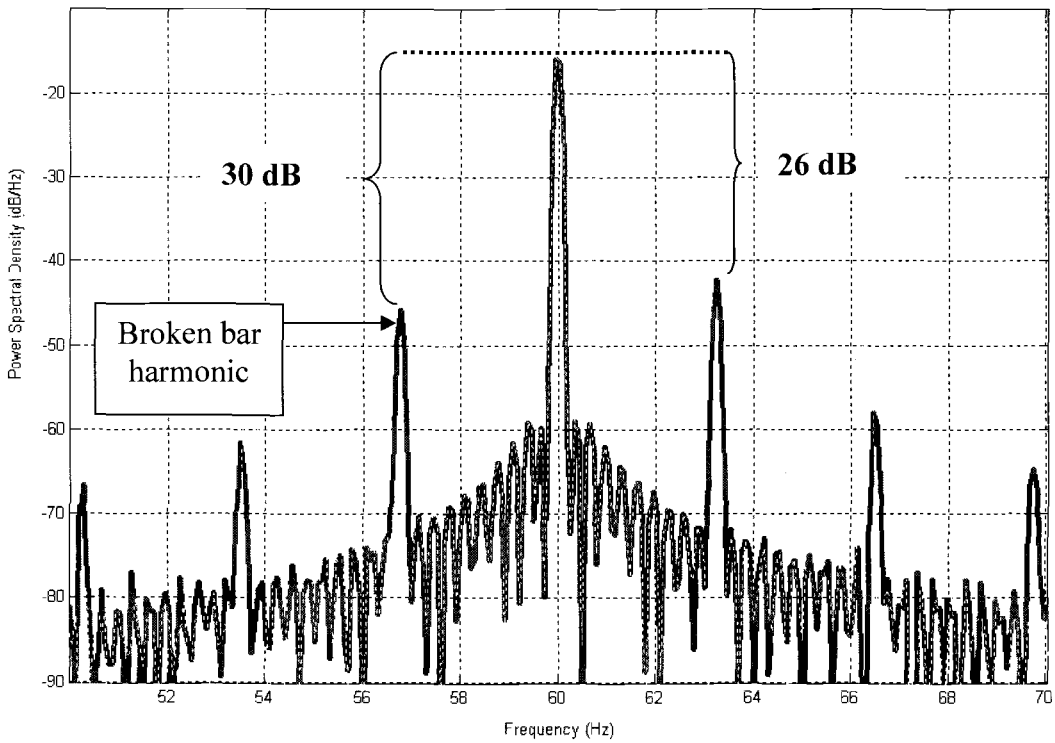

Fig. 2.9: Power spectral density of stator current at 100% load condition of a 6-pole IM (R= 42 and slip = 0.027)

Example 2.1:

From Fig.2.9, the number of broken bars can be estimated by equation (2.7) as the following:

the average dB difference between lowest sideband components and supply frequency component at full-load condition is (26+30)/2 = 28, so n = 2.43 which implies that the number of broken bars is approximately equal to three broken bars. However, the actual number of broken bars is equal to four which indicates the approximate nature of the technique.

A large number of induction machine faults produce anomalies in the air-gap flux density by affecting either the air-gap MMF or the air-gap permeance of the motor. The air-gap flux density is defined to be the product of the air-gap MMF and the air-gap permeance:

$$\phi = P.\,MMF \tag{2.8}$$

where ϕ is the air-gap flux density, P is the air-gap permeance and MMF is the stator magneto-motive force. Variations in either term will produce sinusoidal variations in the air-gap flux density. In addition to inherent flux irregularities, a broken bar fault primarily influences the rotor MMF wave, and hence the rotor MMF, as shown in Fig. 2.10. Since the mutual inductances of the machine are calculated from the air-gap flux density, any rotational variation produced by a fault condition causes the inductances to vary with respect to the mechanical rotor position or the mechanical rotational speed of the motor. Principally, fault severity dramatically increases when the defective bars belong to a small group of rotor bars, since the rotor current (I_r) is shared equally in all N intact bars with I_r /N in each.

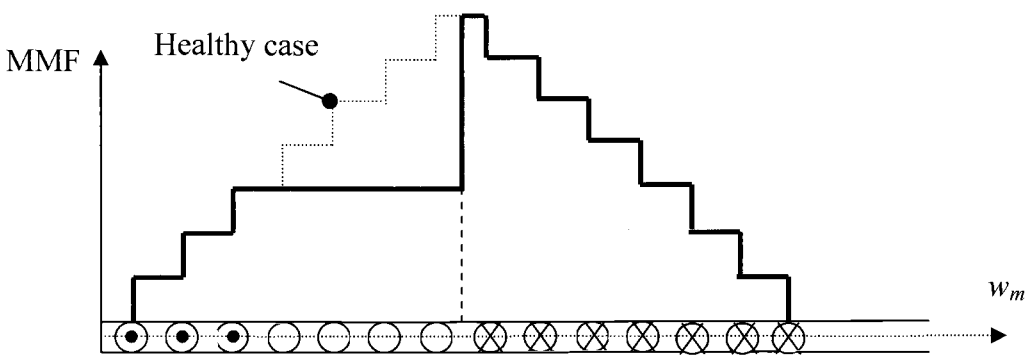

Fig. 2.10: Rotor MMF wave disturbance due to four broken bars in a seven (7) bars/pole (42bars/6poles) motor

$$K_{clark} = \frac{2}{3}\begin{bmatrix} 1 & -\frac{1}{2} & -\frac{1}{2} \\ 0 & \frac{\sqrt{3}}{2} & -\frac{\sqrt{3}}{2} \\ \frac{1}{\sqrt{2}} & \frac{1}{\sqrt{2}} & \frac{1}{\sqrt{2}} \end{bmatrix}\begin{matrix} d \\ q \\ 0 \end{matrix} \tag{2.9}$$

Practically, applying reference frame theory can help in analyzing the behavior of broken bar sidebands. Extending Clark transformation in equation (2.9) to the stator current signal and extracting *d-q* components is straightforward. The *q-axis* carries the torque oscillation signals while the *d-axis* carries the speed fluctuations signal. This proves that the lower sideband (LSB) is a reaction of the torque ripples from a broken rotor bar while the upper sideband (USB) is a reaction of the speed ripples from the broken bar as illustrated in Fig. 2.11. Here the machine-load inertia plays a major role in damping the reactive speed ripples at *(1+2s)f* originally produced by the *(1-2s)f* sideband. The tested motor is of low load inertia equal to 0.04 kg.m^2, which magnifies the *(1+2s)f* sideband amplitude from the speed ripples. However, torque ripples caused by rotor asymmetry are proportional to the mechanical system inertia. In summary, load inertia causes a trade-off effect between USB and LSB sideband amplitudes. A global diagnostic index can be formulated using the average amplitude of both 1st order sidebands of broken bar, as extracted from Fig. 2.9.

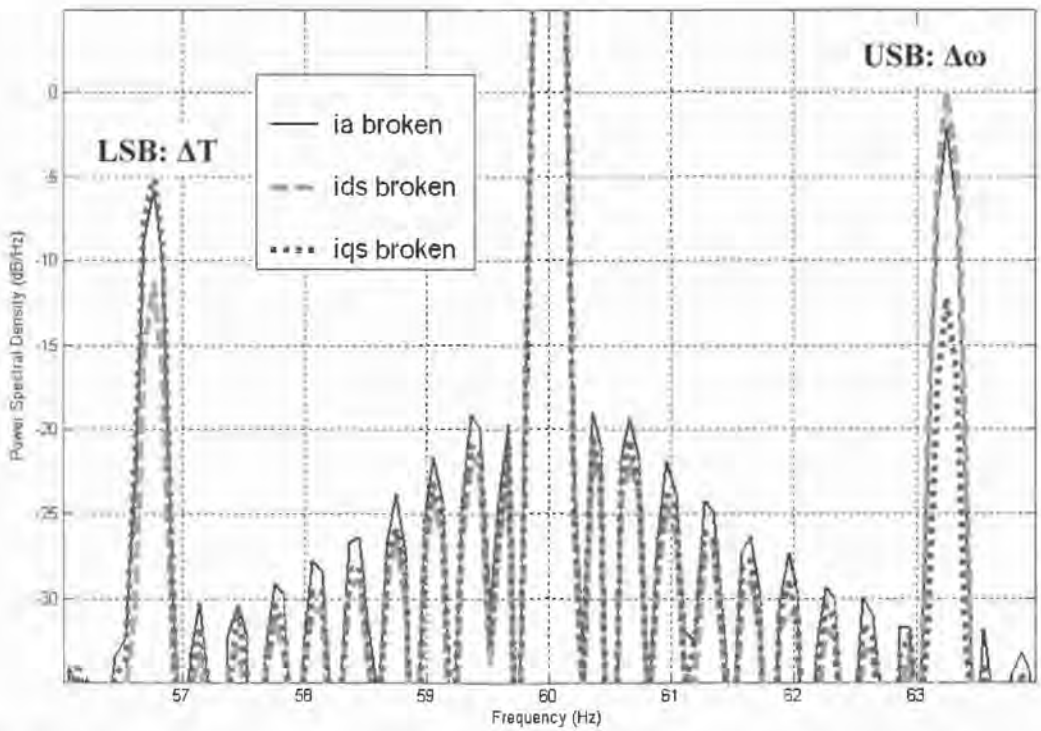

Fig. 2.11: Power spectrum density for *d-q* analysis of the four broken bars fault. LSB is a machine torque ripple (ΔT) reaction due to broken bars, while USB is a speed ripples (Δω) component

The MATLAB® program code in appendix C was used to implement the stator reference frame transformation to three-phase terminal currents of the monitored machine. Then all transformed quantities are manipulated to extract negative-sequence components associated with the four broken bars fault signals:

$$\begin{bmatrix} i_{a2} \\ i_{b2} \\ i_{c2} \end{bmatrix} = \frac{1}{3}\begin{bmatrix} 1 & a^2 & a \\ a & 1 & a^2 \\ a^2 & a & 1 \end{bmatrix}\begin{bmatrix} i_a \\ i_b \\ i_c \end{bmatrix}, \; a = e^{j\frac{2\pi}{3}} \qquad (2.10)$$

The analysis of the *d-axis* current using the negative-sequence approach, as in equation (2.10), shows that the stator air-gap flux negative-sequence content can be investigated. Notably, both LSB and USB have the same fault severity as depicted in Fig. 2.12, which indicates that any deviations are only due to induced torque and speed ripples from the defective bar. Therefore, the amplitude of the line current LSB is more related to negative-sequence amplitude in contrast to the amplitude of the USB that has higher amplitude far from negative-sequence due to the induce speed ripples aligned with (i_{ds2}) current. Evidently, the torque variations are the main symptom of the broken bar fault as the defective bars inject a negative-sequence torque that the LSB can measure it more acutely.

Thus, it is concluded that negative-sequences analysis is a fundamental and useful tool, entailing its implementation during this research for the purpose of measuring the magnitude of fault signals and the separation from any overwhelming torque ripples from the load. Chapter 6 addresses in more detail the subject of negative-sequence mean values as an approach for rotor fault separations.

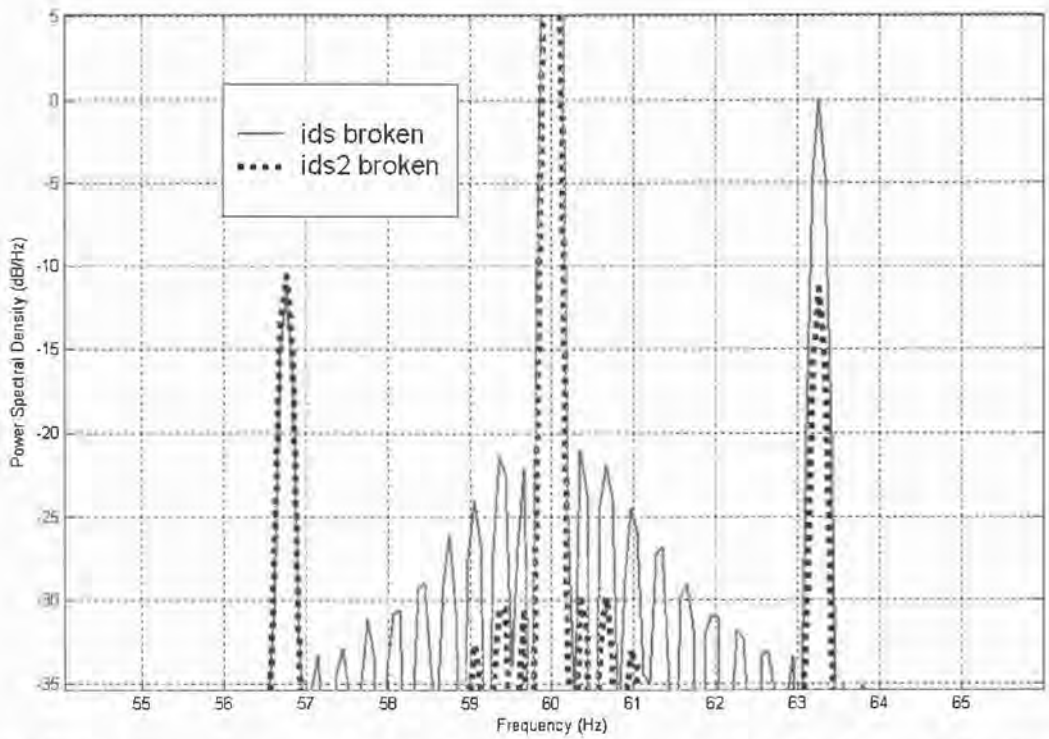

Fig. 2.12: Power spectrum density of negative-sequence of broken bars sidebands (i_{ds2})

2.2. Air-gap eccentricities and asymmetries

The air-gap is not of constant size around the rotor, but has inherent imperfections due to manufacturing tolerances. Rotor eccentricity in IM can be divided into static and dynamic eccentricities. In the next sections, analytical and experimental investigations of those types of eccentricities will be presented.

2.2.1. Static eccentricity analysis background

Static eccentricity can be caused when the rotor rotational axis and symmetry axis are displaced from the stator bore axis but rotor is still turning upon its own axis. Also, static eccentricity can be caused by stator bore out-of-round [9], [10] as shown in Fig. 2.13. The primarily causes of static eccentricity are related to manufacturing deficiencies of the stator bore and/or bearing off-centering or incorrect positioning. Static eccentricity

causes a static force pull on the rotor in one direction. This constant unbalanced magnetic pull (UMP) is generally difficult to detect and requires specialized testing equipment only possible during off-line conditions for plant motors [10].

Previous research has proven that there are some mitigation methods which can be considered during the manufacturing process to optimize motor performance and to avoid excessive UMP forces. Moreover, these procedures can help to prevent impeding static eccentricity from consequently damaging stator windings by rotor-to-stator rub. Parallel connections of stator windings have been found to significantly reduce the magnitude of the UMP present in the motor [11].

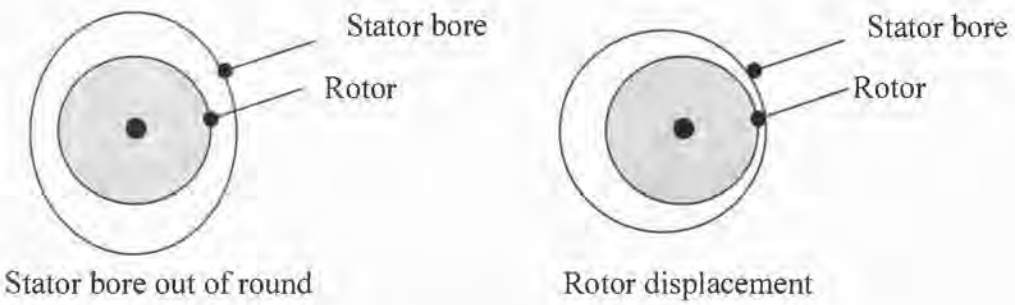

Fig. 2.13: Static eccentricity types

As stated in section 2.1.2, rotor faults typically produce anomalies in the air-gap flux density by affecting either the air-gap MMF or the air-gap permeance of the motor. Static eccentricity mainly influences the air-gap permeance, causing an additional spatial Fourier series component as in equation (2.11) [12]. The reason is that the MMF depends on the winding topology, number of turns and current. As an elementary effect of static eccentricity fault, the level of rotor irregularity with respect to surrounding air-gap increases.

The permeance distribution is given by

$$P_s = \sum_{i=0}^{\infty} P_i \cos(i\Phi) \qquad (2.11)$$

where P_S is the overall static eccentricity permeance, P_i is the air-gap permeance oscillation amplitude and Φ is the angular position. The air-gap permeance is a function of air-gap length:

$$P_g = \mu_o / g \tag{2.12}$$

where P_g is the air-gap permeance, g is the mean air-gap length and μ_o is the permeability of free space.

The model of eccentricities is widely used in investigating the generation of eccentricity related harmonics. This model is illustrated in Fig. 2.14, duplicated from [9]. This model represents the rotor eccentricities based on the assumption that the stator is a perfect circle with no slotting position or time harmonics. Both static and dynamic eccentric rotors can be represented by the eccentricity model. Conceptually, the Fourier series content of an irregular rotor geometry is stationary in the stator reference frame in case of static eccentricity while the dynamic case is dependant on rotor speed, as will be discussed in the next session.

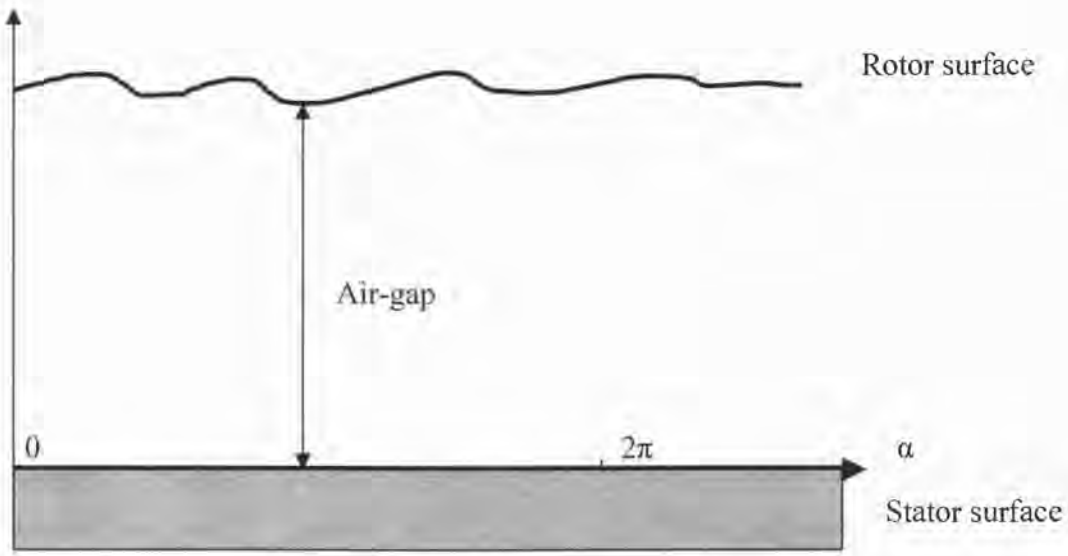

Fig. 2.14: Rotor eccentricity representation

2.2.2. Dynamic eccentricity analysis background

The rotor dynamic eccentricity is caused when the rotor rotational axis does not coincide with its symmetry axis or because of an out-of-round rotor as shown in Fig. 2.15. The primary causes of dynamic eccentricity are related to imbalanced forces exerted on the rotor during operation at critical speed which create rotor "whirl". A bent rotor shaft or worn bearings can cause similar effects. Those dynamic forces pull on the rotor and rotate at its velocity. This makes the UMP forces easily detectable by vibration monitoring.

Previous works show that vibration due to dynamic eccentricity can be massively reduced by adjusting the rotor skew to more practical levels. [13] verified that skewing the rotor does increase the UMP in cage IM when the rotor is eccentric.

In practice, both forms of eccentricities inherently exist in any IM and an increase of UMP can be due to either one. Moreover, causes of those pull forces are many and most of the time they overlap.

The air-gap permeance due to dynamic eccentric rotor or asymmetric rotor shape is

$$P_D = \sum_{i=0}^{\infty} P_i \cos i(\Phi - w_r t) \qquad (2.13)$$

where P_D is the dynamic eccentricity permeance and w_r is the rotor rotational speed in radians/second.

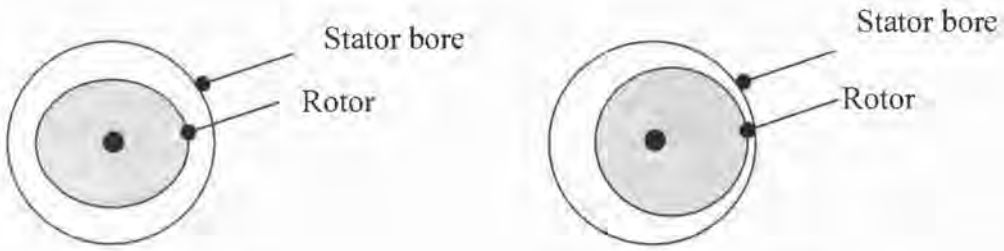

Rotor out of round

Rotor rotational and rotor symmetry axis do not coincide (rotor does not turn on its own center)

Fig. 2.15: Dynamic eccentricity types

Stator air-gap fields induce EMF's into the rotor cage and then produce rotor surface MMF waves as illustrated in Fig. 2.8 (healthy case waveform). The rotor MMF waves produce back EMF's through the air-gap and can be reflected by the stator via parallel or series stator windings. It is obvious to note that both static and dynamic eccentricities produce their own spatial pole-pair $p \pm 1$ field components, but the rotational velocity is the only difference between them as in equation (2.14). Dynamic eccentricity leads to slip frequency current components for the $p \pm 1$ MMF waves [10].

This leads to the conclusion that magnitudes of field components and rotor MMF harmonics govern the behavior of current sideband densities due to either static or dynamic eccentricities.

$$\begin{aligned} b_s = (y,t) = & B_s^p \cos(wt - pky) \\ & + B_{S(s)}^{p-1} \cos(wt - (p-1)ky) \\ & + B_{S(s)}^{p+1} \cos(wt - (p+1)ky) \\ & + B_{S(d)}^{p-1} \cos((w - w_r)t - (p-1)ky) \\ & + B_{S(d)}^{p+1} \cos((w + w_r)t - (p+1)ky) \end{aligned} \qquad (2.14)$$

where w is the supply frequency in radians/second, p is the pole-pair field, k is the inverse of average air-gap radius, y is the linear distance round the air-gap circumference from some base point (such that ky = angle round the air-gap from the base point), b_s is the stator air-gap field is stator reference frame, B_s^p is the main air-gap stator field with a pole-pair field p, $B_{S(s)}^{p-1}$ and $B_{S(s)}^{p+1}$ are the air-gap stator fields due to static eccentricity with spatial pole-pair fields $p-1$ and $p+1$ respectively, $B_{S(d)}^{p-1}$ and $B_{S(d)}^{p+1}$ are the stator air-gap fields due to dynamic eccentricity with spatial pole-pair fields $p-1$ and $p+1$ respectively.

Ideally, as shown in Fig. 2.6, when motor loading increases the field produced by the extra stator current is cancelled out by the reaction field from the equal and opposite currents induced in the rotor, resulting in consistent air-gap field orientation and

magnitude. However, in practice and due to rotor irregularities and asymmetry caused by static or dynamic eccentricities, additional field harmonics are induced in the air-gap where a change in the resulting air-gap field will be encountered. By applying Ampere's circuital law, the current density flowing in the mutual inductance also changes.

$$B_g = P_g \int \mu_o J_m .dy \qquad (2.15)$$

where B_g is the air-gap flux field and J_m is the current density flowing in the magnetizing inductance of the machine.

The magnitudes of the spatial pole-pair $p \pm 1$ field components increase proportionally with the load. However, the rotor damps the produced eccentricity fields by reducing the total irregularity measure as seen by the stator reference frame. This damping effect can be explained by studying equations (2.14) and (2.15). From equation (2.14), it is evident that only dynamic UMP related forces are affected by rotor rotational speed. Referring to the experiment result in section 2.2.3, dynamic eccentricity typically decreases with loading but with a marginal increase beyond full-load point. This unique behavior of dynamic eccentricity influences the relative density of the current flowing in the stator. By deriving the current density from equation (2.15), the relationship between rotor speed and dynamic eccentricity severity can be explained.

$$J_{SD} = \frac{\frac{dB_g}{dy}}{\mu_o P_g} \qquad (2.16)$$

The angular position rate of change $d\phi / dt$ is equal to rotor speed w_r in radians/second. The lower $d\phi / dt$ rate implies a proportional rate of change of eccentric rotor MMF waves with respect to the linear distance around the air-gap circumference. Therefore, the total dB_g / dy observed by the stator reference frame of the current

density J_{SD}, which is related to dynamic eccentricity, obviously decreases due to the reduction in rotor velocity.

The stator current signature basically mirrors the fundamental frequency component and any other created frequency components into the rotating air-gap field. Eccentricity sideband harmonics are inevitable in any IM, making it possible to diagnose multiple fault cases more efficiently. The 1st order stator sideband harmonics induced in the stator windings due to the rotor irregularities can be seen around 40 and 80Hz in the case of a 6-pole machine. The behaviors of those sidebands through various loading points can reflect actual mechanisms of rotor impeding eccentricities. The suggested method has been applied on 6-pole machines, during which its effectiveness was verified. Chapter 4 discusses more details of this method.

2.2.3. Experimental results

The laboratory implementation of mechanical dynamic eccentricity is based on adding an aluminum disk with steel bolts and nuts of various masses placed at different radial distances from the rotor shaft. The dynamic eccentricity has been created by placing 120g or 220g bolts at eight different holes located at 7.6, 10, 12.7, and 15.2 cm radial disk distances to simulate different vibration levels, as in Fig. 2.16 (a) and (b). An alternative method of calculating the dynamic eccentricity is provided in appendix B.

Specific frequencies caused by the eccentricity problem are monitored

$$f_{ec} = f_s\left[1 \pm m\left(\frac{1-s}{p/2}\right)\right] \qquad (2.17)$$

where f_{ec} is the air gap eccentricity frequency, p is the number of motor poles and m = 1, 2, 3, ... a multiplying index. Frequencies close to the fundamental frequency are extracted during nominal full-load slip value, seen in Table 2.2. The resultant non-supply current components produced in the supply current are found to exist experimentally and

are certainly verified to be due to both dynamic and static eccentricity. In practice, when dynamic eccentricity occurs, both types of eccentricity exist together.

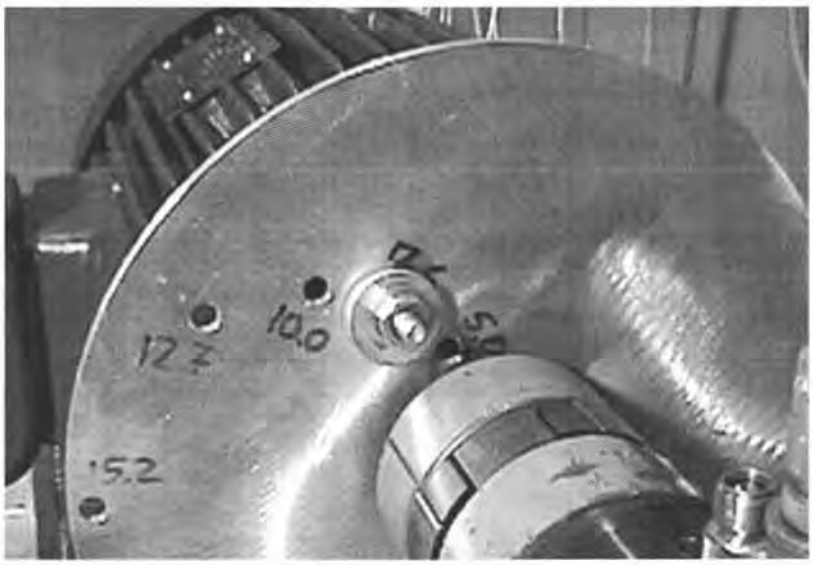

(a) Dynamic Eccentricity simulation using an unbalanced disk

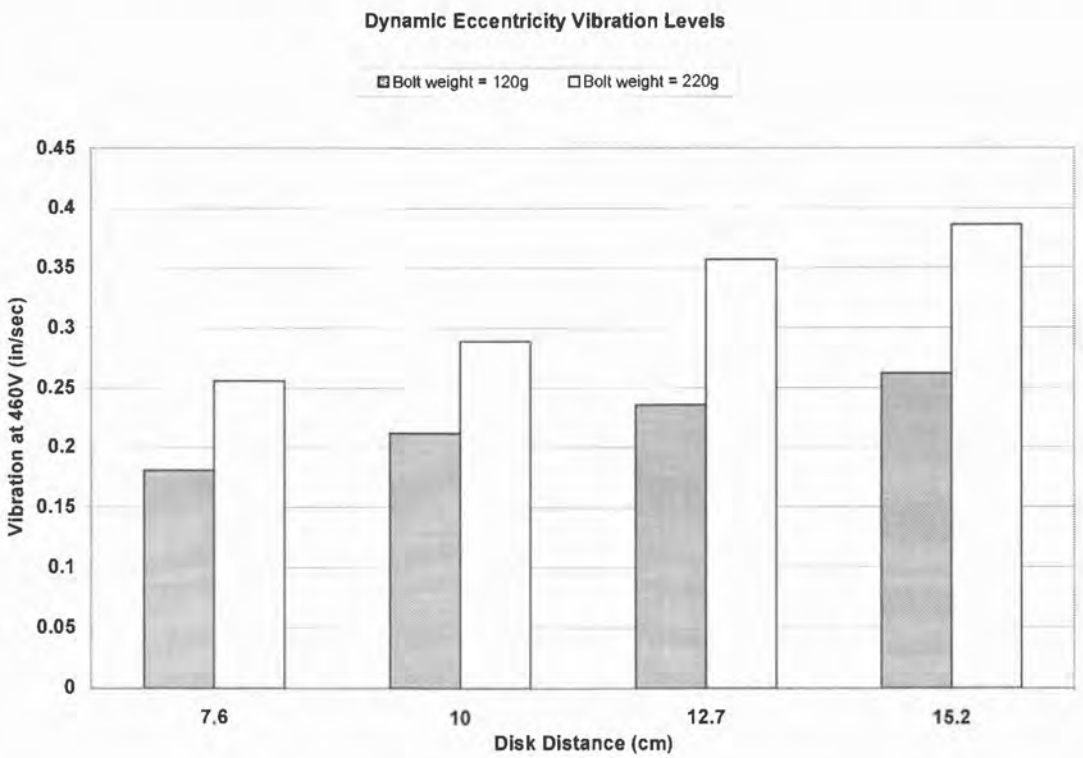

(b) Eight vibration levels created by the unbalanced disk

Fig. 2.16: Dynamic eccentricity simulation

Table 2.2
Eccentricity frequencies for a 6-pole IM at nominal full-load slip (0.027)
f_s is supply frequency (Hz), f_r is rotor rotational speed in radians/second (Hz)

m	f_{ec}	*Approximation*	*Accuracy*	*m*	f_{ec}	*Approximation*	*Accuracy*
1	79.6	(f_s+f_r)	*Inconsistent*	-1	40.4	(f_s-f_r)	***Clear & consistent***
2	99.2	(f_s+2f_r)	*Inconsistent*	-2	20.8	(f_s-2f_r)	*Inconsistent*
3	118.8	$(2-s)f_s$	*Not clear*	...	....		
4	138.4	$(2f_s+f_r)$	*Not clear*	...	....		
5	158	$2(f_s+f_r)$	*Inconsistent*	...	....		

Well-known monitoring techniques using accelerometer readings, for stator casing vibration analyzed the UMP caused by both eccentricity types. Dynamic eccentricity creates a rotating force, therefore monitoring the rotational speed vibration can assist in verifying which type of eccentricity exists in the motor. Fig. 2.17 shows that three levels of dynamic eccentricity can consequently increase current sidebands, which proofs current signature effectiveness for detecting and quantifying the gravity of related faults. When combining vibration and current monitoring techniques, one can verify whether the dynamic or static eccentricity type is more dominant.

However, not all the monitored current sidebands in Fig. 2.17 can reflect an exact measure of dynamic eccentricity severity or any eccentricity condition in general. Only the (f_s-f_r) sideband current is clear and of consistent accuracy, as expected with a comparative increase of dynamic eccentricity levels. This sideband occurrence is somewhat analogous to the broken bar harmonic in session 2.1. Based on the results in Fig. 2.11 and 2.12, it was confirmed that both upper and lower sidebands (USB and LSB respectively) have the same flux negative-sequence contents. However, direct spectral analysis of line current shows that LSB is aligned with negative-torque signal (*q-axis*) at the frequency shift of $2sf_s$ while USB is aligned with speed ripples (*d-axis*). Also, the line current LSB amplitude is more related to negative-sequence amplitude in contrast to USB which has higher amplitude than from negative-sequence. Despite the fact that variable torque could be induced due to broken bar fault, the eccentricity mechanism does not cause a relative torque variation but can mainly induce a negative-sequence components

in the air-gap. Now the interpretation of why the eccentricity sideband at (f_s-f_r) incorporates a unique fault surveillance measure is clear. This frequency component has a more pure and accurate fault index if effective torque pulse filtration is integrated. The dynamic eccentricity negative-sequence associated components are correctly measured and behave proportionally with increased levels of vibration.

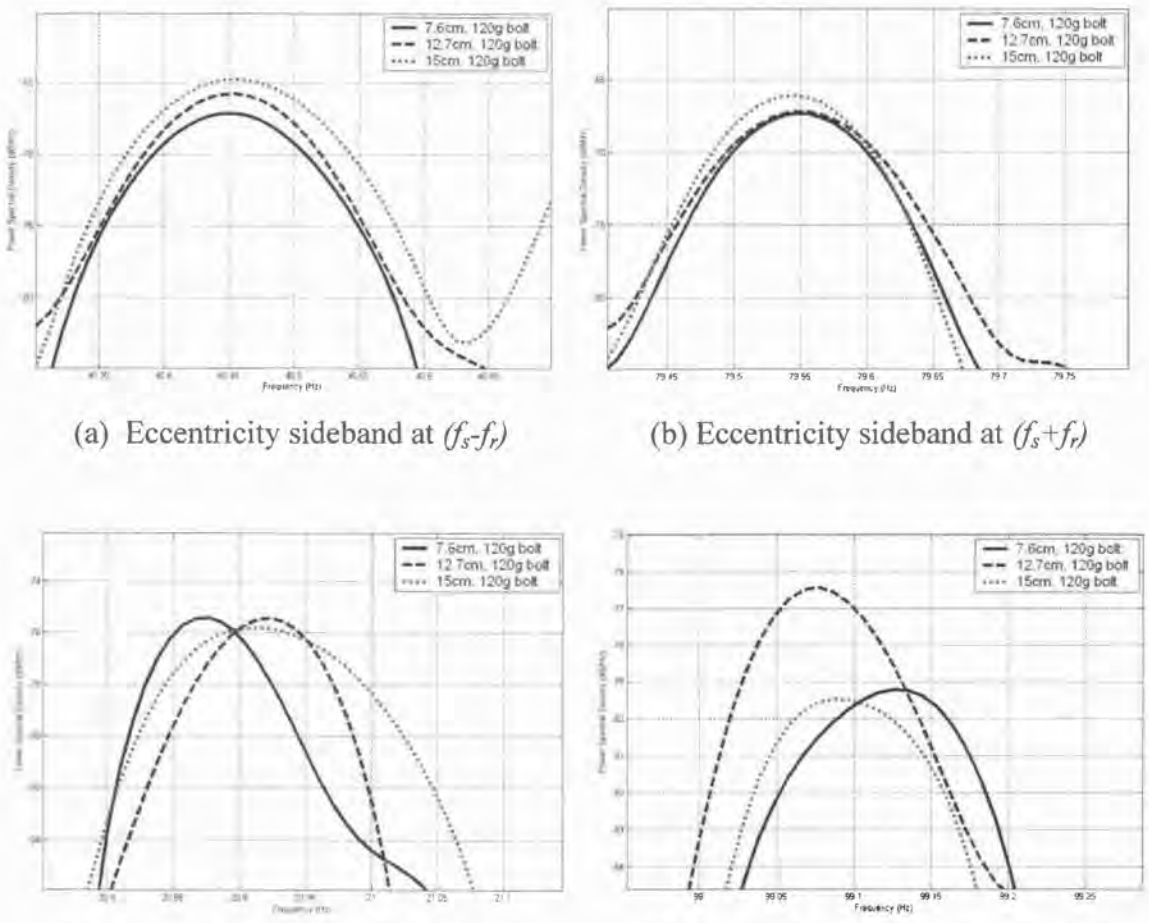

(a) Eccentricity sideband at (f_s-f_r)

(b) Eccentricity sideband at (f_s+f_r)

(c) Eccentricity sideband at (f_s-2f_r)

(d) Eccentricity sideband at (f_s+2f_r)

Fig. 2.17: Power spectrum density of stator current sidebands due to dynamic eccentricity

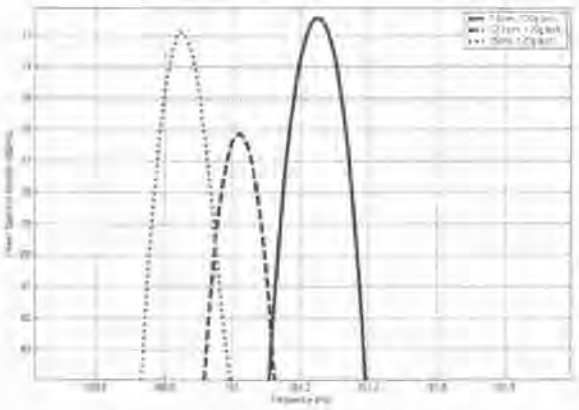

(e) Eccentricity sideband at $2(f_s-f_r)$

Fig. 2.17 (cont.): Power spectrum density of stator current sidebands due to dynamic eccentricity

The core saturation effect on the permeance of machine air-gap is also investigated. Reduced terminal voltage can purify the rotor fault signal from saturation effects, verified by monitoring the 3rd harmonic as shown in Fig. 2.18 (a). As an example, Fig. 2.18 (b) illustrates the amplitude of the dynamic eccentricity sideband at (f_s-2f_r), which is inversely proportional to stator terminal voltage. This behavior is due to the reduction in core saturation that negatively influences the accuracy of the fault signal and consequently suppresses any fault signals from the rotor. Moreover, under voltage produces operation at low rotor speed (high slip) that increases the rotor frequency and consequently increases the rotor current density, making the flux more coupled to the stator windings. Therefore, any flux variations due to eccentricity in the air-gap will be more dominant in amplitude.

However, in practice, the above results lead to an unpractical way of monitoring in service motor vibrations due to dynamic eccentricity because low voltage operations will be terminated by under voltage relays and are also considered to be a time consuming task during off-line tests.

In contrast, Fig. 2.18 (c) shows an amplitude of the 1st order dynamic eccentricity sideband at (f_s-f_r), which obviously decreases when a specific level of eccentricity is maintained during voltage reduction. This proves the earlier discussion that this sideband can measure the flux rate of change as a function of rotor speed in an analogous manner

to the reduction of rotor speed by more loading, as discussed in session 2.2.2. Estimation of an accurate rotor fault severity requires maintaining rotor speed at constant values when comparing with a new data set. This is a critical feature derived to measure accurate magnitudes of the $(f_s\text{-}f_r)$ sideband. Chapter 4 discusses this in more detail.

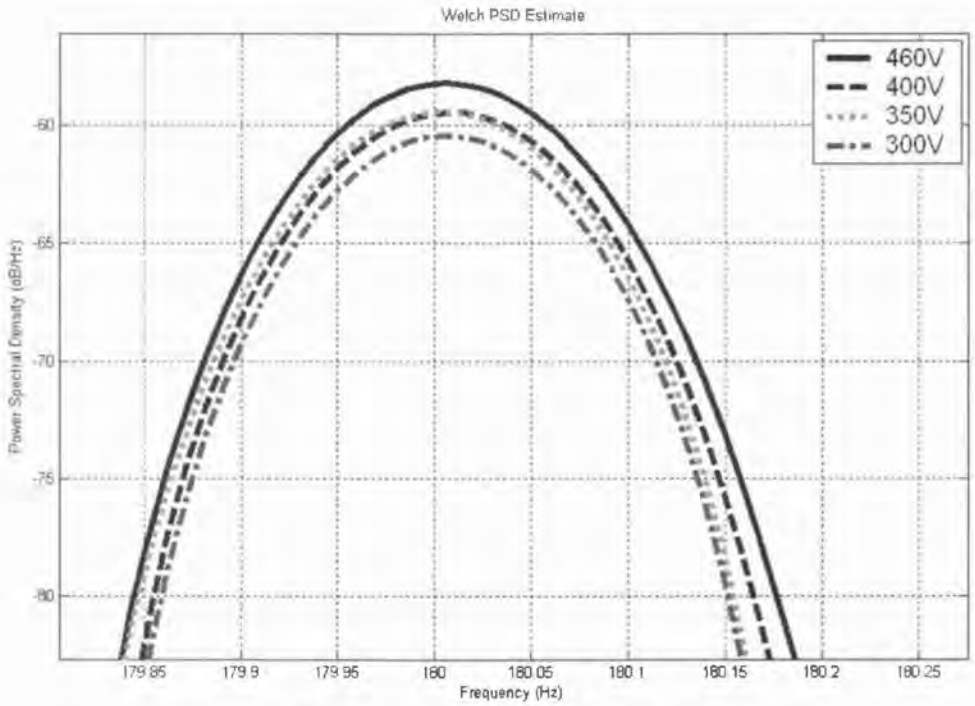

(a) 3rd Harmonic relationship with saturation

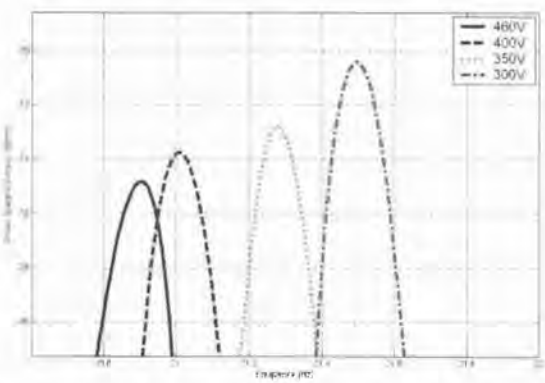

(b) Dynamic eccentricity sideband at $(f_s\text{-}2f_r)$

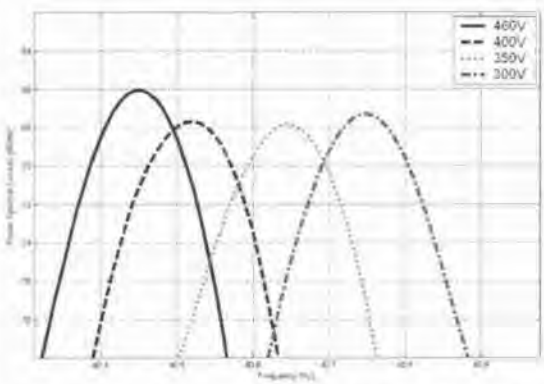

(c) Dynamic eccentricity sideband at $(f_s\text{-}f_r)$

Fig 2.18: Power spectrum density of stator current sidebands at reduced terminal voltage

In general, eccentricity related frequencies are of orders

$$f_{ec} = (f_s \pm k.f_r) \qquad (2.18)$$

where $(f_s - f_r)$ is experimentally verified to be the optimum fault feature, which can be derived similarly from a broken bar, eccentric rotor or any other air-gap asymmetries such as shaft misalignment.

Other air-gap anomalous behaviors that can be encountered are motor shaft misalignments. Two types of misalignments simulated in this study are the horizontal and vertical (radial) misalignments of the motor with respect to the shaft and load. The horizontal situations have been created by shifting the machine in the horizontal plane (*xy*-plane) at a specific offset with respect to its rotor shaft and coupled load. The vertical (radial) misalignment has been created by inserting additional shims of specific thickness under the base of the machine to lift it upward with respect to the shaft of its coupled load in the direction of the *yz*-plane. Fig. 2.19 illustrates how the types of misalignments are created.

Similar to dynamic eccentricity, a motor misalignment condition can be quantified more reliably by measuring the sideband at $(f_s - f_r)$. Fig. 2.20 compares different levels of vibration due to normal, vertical and horizontal misalignment conditions as in Table 2.3, which shows that vibration severity increases due to vertical and horizontal misalignments. Vertical misalignment, in this example, has the highest vibration value. Fig. 2.20 (a), (b), and (c) show the stator current sidebands at $(f_s - f_r)$, $(f_s + f_r)$, and $(2-s)f_s$ respectively. These measure the relative vibration severity as expected. However, in this research only $(f_s - f_r)$ is considered as the rotor fault universal index because of its consistency and reliability. Contrary to that, $(f_s + f_r)$, and $(2-s)f_s$ sidebands are not clear or consistent in the case of dynamic eccentricity, as in Table 2.2.

Many sources share the interesting outcome that speed can be estimated accurately using current signature analysis, regardless of knowing the rotor bars count (as in the slot harmonics monitoring method) and avoiding physical proximity due to speed transducers. The sought after $(f_s - f_r)$, $(f_s + f_r)$, and $(2-s)f_s$ sidebands are simple yet accurate

estimation tools for rotor speed. Chapter 3 discusses extracting the rotor speed using 1st order dynamic eccentricity sidebands in more detail.

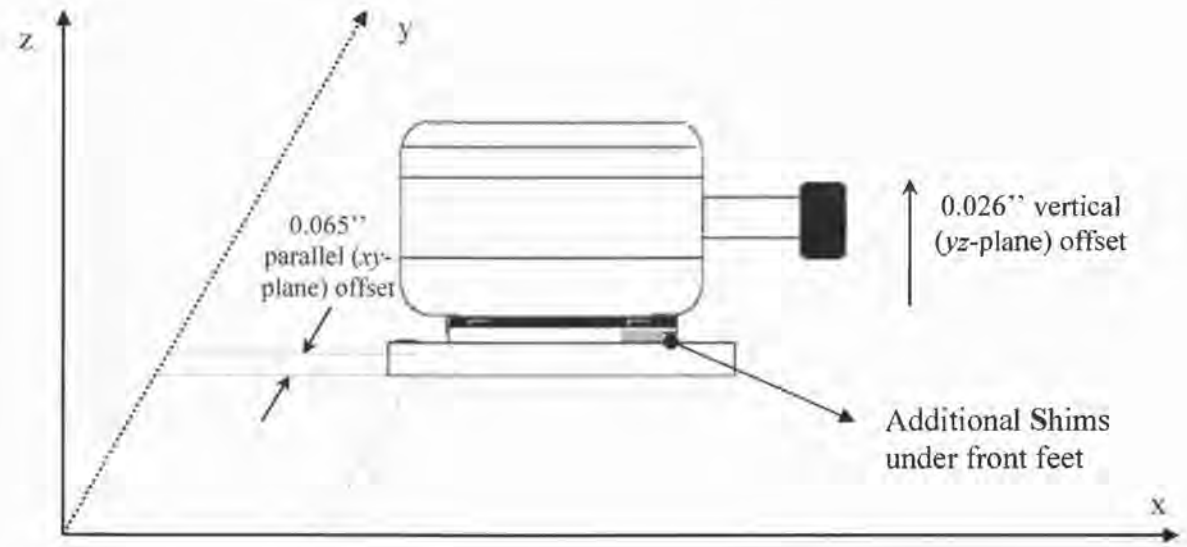

Fig. 2.19: Horizontal and vertical (radial) misalignments creation

Table 2.3
Vibration measurements at vertical (radial) and horizontal misalignments

Motor condition	Offset distance (in)	Vibration (in/sec)
Normal	0	0.0195
Horizontal misalignment	0.065 parallel offset on xy-plane	0.036
Vertical misalignment	0.025 offset on face of coupling on yz-plane	0.058

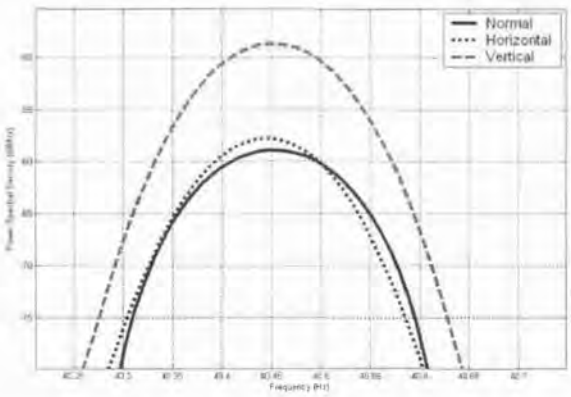

(a) Eccentricity sideband at (f_s-f_r)

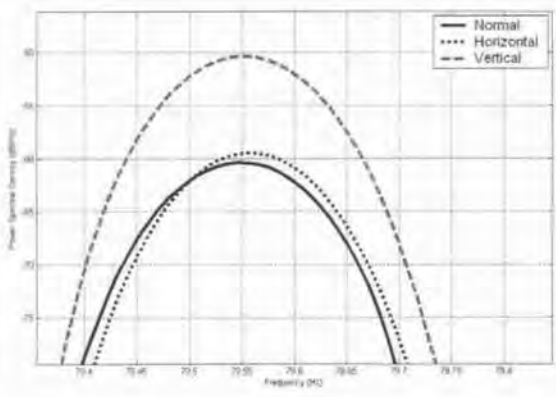

(b) Eccentricity sideband at (f_s+f_r)

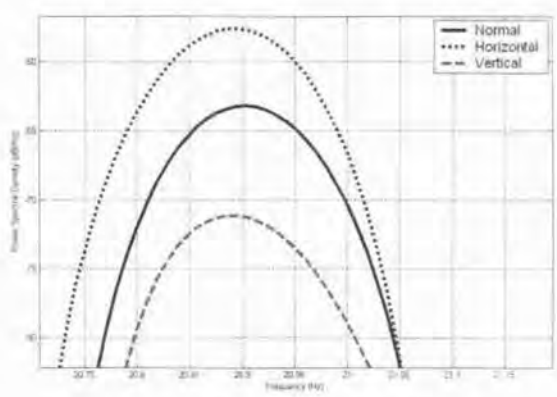

(c) Eccentricity sideband at (f_s-2f_r)

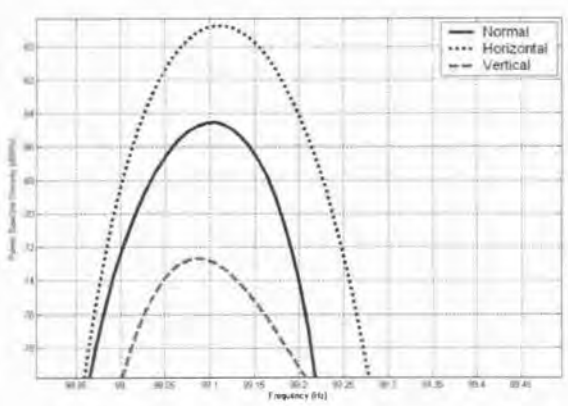

(d) Eccentricity sideband at (f_s+2f_r)

Fig. 2.20: Power spectrum density of stator current sidebands due to Normal, vertical and horizontal misalignments at slip = 0.027, poles = 6, rotor bars = 42

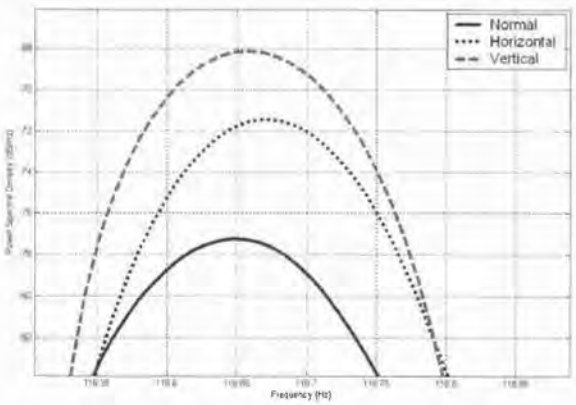

(e) Eccentricity sideband at $(2\text{-}s)f_s$

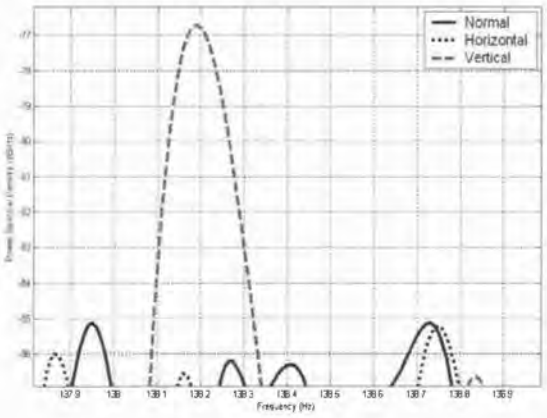

(f) Eccentricity sideband at $(2f_s+f_r)$

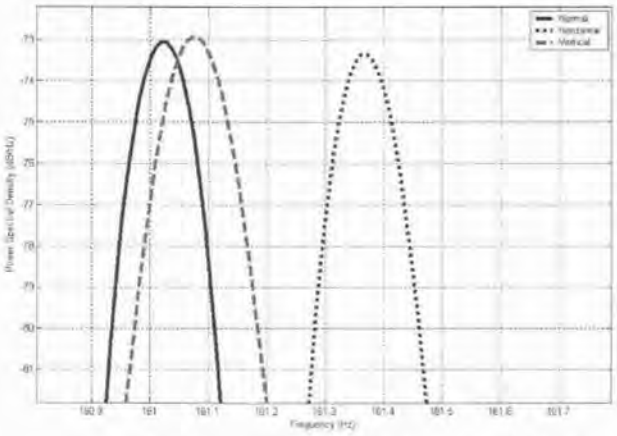

(h) Eccentricity sideband at $2(f_s+f_r)$

Fig. 2.20 (cont.): Power spectrum density of stator current sidebands due to Normal, vertical and horizontal misalignments at slip = 0.027, poles = 6, rotor bars = 42

2.3. Arbitrary load conditions

2.3.1. Analytical background

The accurate fault detection methods will lead to a more effective parameter correlation and interpretation. Therefore, a clear definition of on-line detection system capabilities is essential and will result in a mature fault analysis based on the measured data. This data will be affected by many other external factors, which will have a major impact on the detection process and will introduce some limitations. Therefore, arbitrary load effects should be considered and carefully evaluated during the rotor fault detection process. This factor will be reflected in the following discussion and will be related to the accuracy of broken bar detection techniques.

The disturbances of the stator currents produced by load torque oscillations are examined. Torque oscillations occur at multiples of rotor rotational speed to produce stator current components at frequencies of

$$f_{load} = f_s \pm m f_r = f_s \left[1 \pm m \left(\frac{1-s}{p} \right) \right] \qquad (2.19)$$

where m = 1, 2, 3, ... a multiplying index, f_{load} is frequency of the stator current at multiples of rotational speed f_r, p is the number of motor poles and f_s is the fundamental stator frequency.

The resulting torque in an AC machine is produced due to induced rotor flux in the radial direction (*d-axis*) outward from the rotor surface. In squirrel-cage motors, the rotor bar produces electromagnetic torque (T_e) proportional to the current flowing in it due to a tangential force in the *q-axis* direction, as shown in Fig 2.18. Assuming a linear mechanical system, all torque variation from the coupled load side can be reflected in the resultant electromagnetic torque (T_e) of the machine [3]. Load torque oscillation is assumed to have the following form and has positive-sequence harmonics only:

$$T_{load} = T_{avg} + T_p \cos(\theta_{rm}) \qquad (2.20)$$

where the electrical and mechanical rotor angles are related by $\theta_r = (p/2)\ \theta_{rm}$, p is the number of machines poles and T_p is the magnitude of induced torque pulsation from a coupled load within the rotor rotational speed range of

$$0 < f_p \leq f_r \qquad (2.21)$$

where f_p is the torque pulse frequency and f_r is the rotor rotational speed. Therefore, the net magnitude of machine flux can also be influenced by load oscillations that vary air-gap inductances at torque pulse rate f_p. Moreover, flux fluctuation reactions due to permeance (eccentricity) or MMF (broken bar) irregularities may overlap with torque pulse effects in the stator current signatures as depicted in Fig. 2.22 (a) and (b). Inherent torque pulses mainly caused by an odd number of rotor bars (impractical design) or eccentricity components aligned with the tangential (*q-axis*) direction are negligible compared to similar components due to broken bar torque pulses. Load torque pulses can obstruct or overwhelm rotor fault sidebands for both eccentricity and broken bar faults. In many practical applications, the stator current sidebands caused by load torque oscillations are many times larger than those produced by the fault conditions. This entails seeking an effective procedure for rotor fault separation. Chapter 6 discusses this in more detail.

Fig. 2.22 mainly compares the torque pulses due to rotor asymmetry and those induced by the coupled load. Different behaviors are extracted by analyzing the positive- and negative- sequences (Fig. 2.22 (a) and (b) respectively) of *d-q* stator current vectors during normal, eccentricity, broken bar and load oscillation conditions. Load oscillation effects (T_p) are positive-sequence components aligned with the *q-axis* that manage the magnitude of the total stator current. Similarly, a broken bar fault also demands more stator current but harmfully reduces the efficiency of the machine; section 5.1 discusses more details. Observing the torque pulse negative-sequence component aligned with the *q-axis*, as in Fig. 2.22 (a), these components are more severe compared to the same fault positive-sequence component aligned with the *q-axis* in Fig. 2.22 (b). This phenomenal

effect discriminates load oscillations from any other fault torque reactions as shown in the next experiment session.

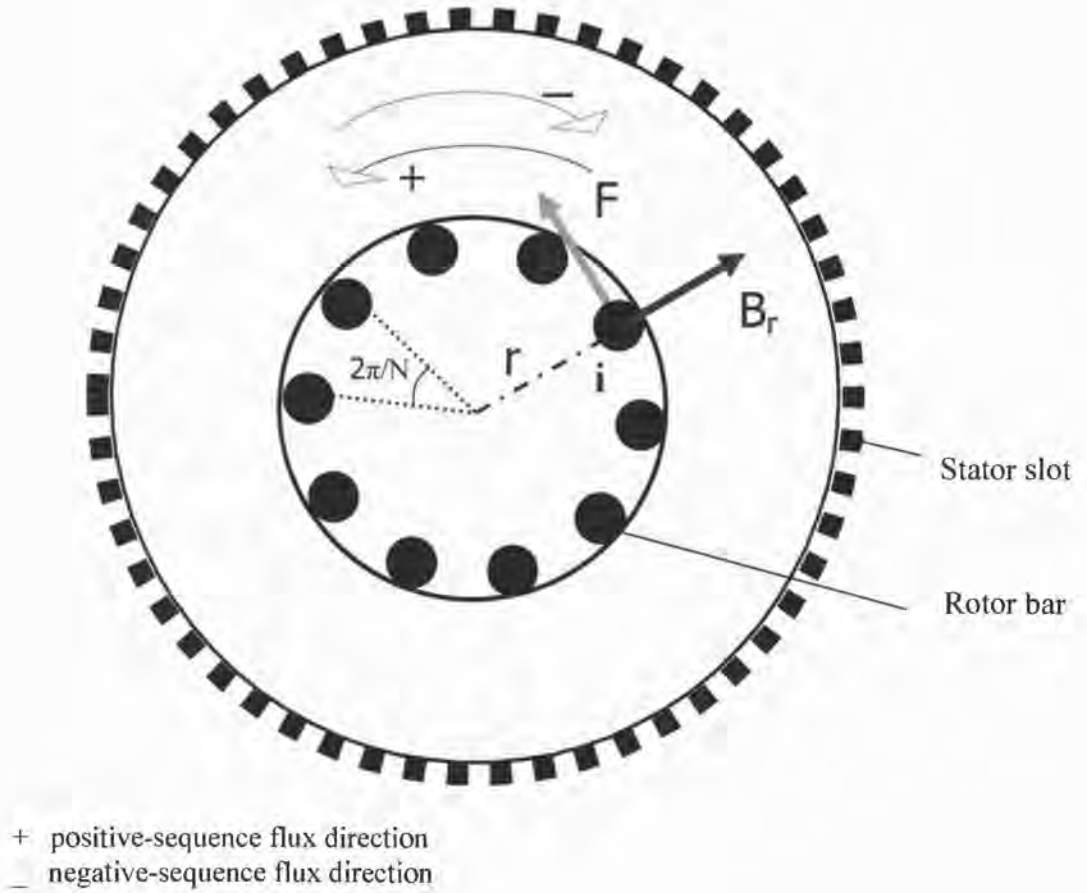

Fig. 2.21: Torque production in squirrel-cage induction machines

High load inertia has two different consequences. Large-size AC machines, with high load inertia, have the advantage of damping speed ripples of rotor asymmetry in addition to the torque ripples induced by the coupled load. However, high inertia magnifies the negative-sequence torques created by a broken bar. Accordingly, the structure of the fault diagnosing task for a large-size IM, as compared to a small-size IM, can assess and discriminate more precisely the operating condition of the machine independent from the load oscillations.

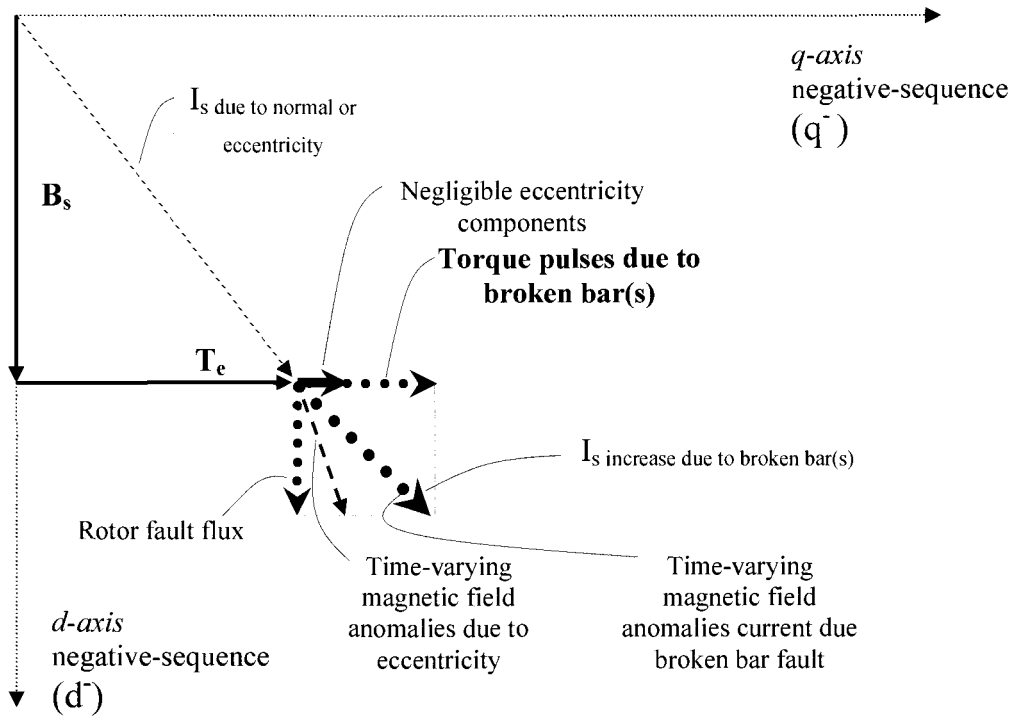

(a) Negative-sequence analysis

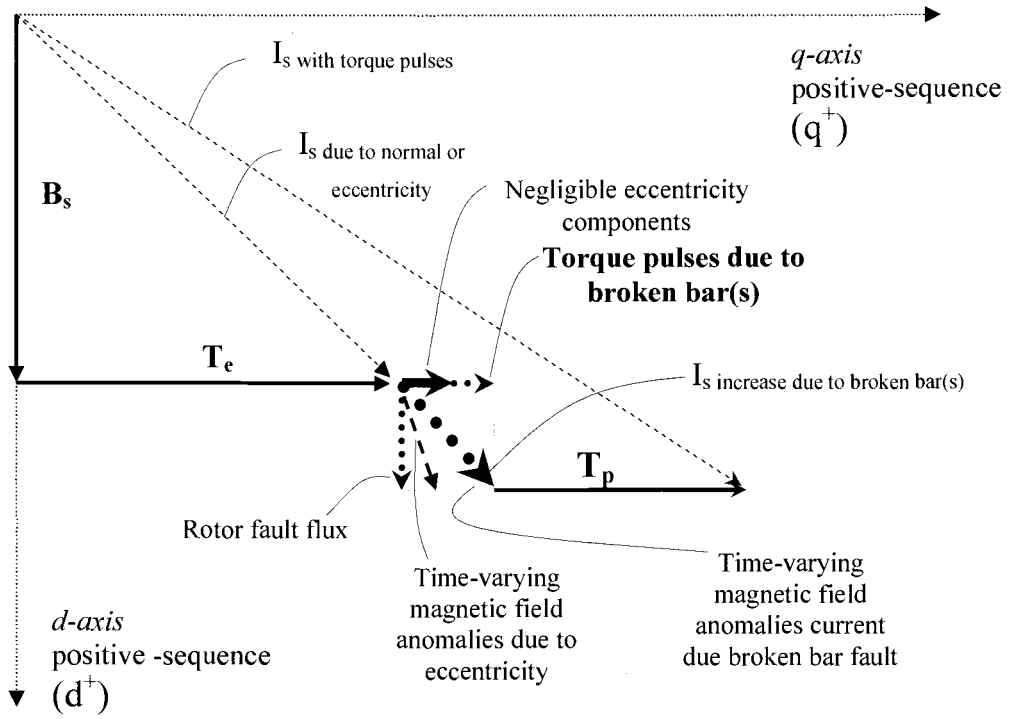

(b) Positive-sequence analysis

Fig. 2.22: Analysis of *d-q* stator current vectors during normal, eccentricity, broken bar and load oscillation conditions

2.3.2. Experimental results

Load torque oscillations are simulated by using the load control circuit depicted in Fig. 2.23 (a). Varying the load torque to a specific value can be accomplished by switching in the desired amount of resistance connected in a shunt with a DC dynamometer's armature circuit. The parallel output current is controlled by an Advanced Power MOSFET IRF542 model of electrical specifications, as shown in Table 2.4. The transistor is switched at predefined frequency settings in a function generator, which control transistor's gate to source voltage. The transistor switches in a drain current that is proportional to the desired torque pulse level. Only positive-cycle patterns of torque can be simulated using this circuit. During this experiment, a maximum of 2 N.m torque pulses are induced at variable times and positions with respect to rotor speed. Fig. 2.23 (b) shows the V_{GS} control signal of the function generator and the resulting stator currents after applying the torque pulsations to the controlled load.

Table 2.4
MOSFET electrical specifications

Specification	Rating
Drain to Source Breakdown Voltage	V_{DS} = 100 V
Continuous Drain Current	I_D = 25 Amps
Gate to Source Voltage	V_{GS} = ±20 V
Maximum Power Dissipation	150 W
Turn-On Delay Time	td(ON) = 15 ns
Turn-Off Delay Time	td(OFF) = 40 ns
Reverse Recovery Time	trr = 150 ns

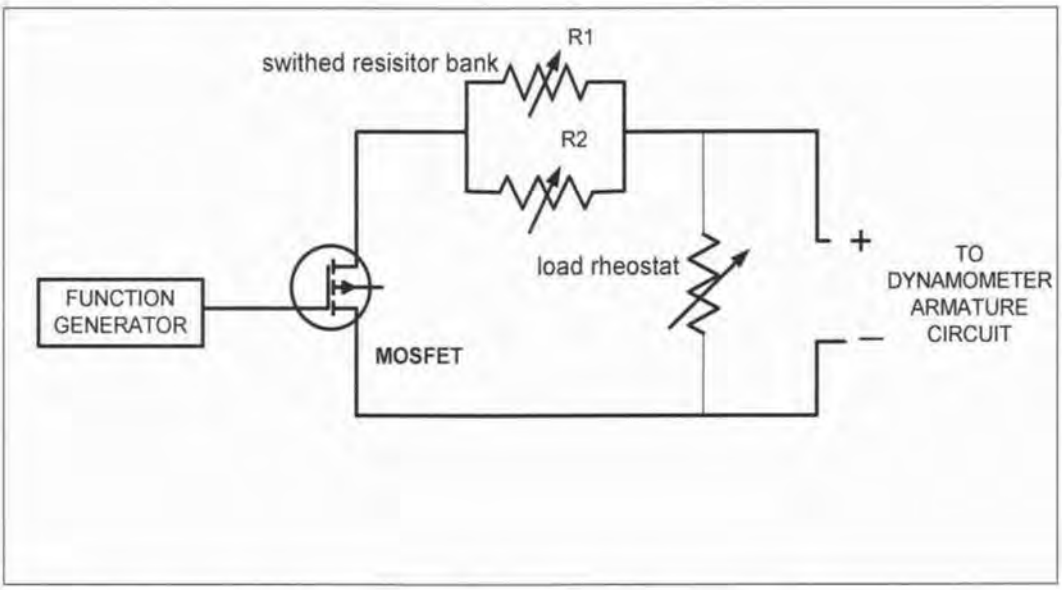

(a) Load control circuit schematic

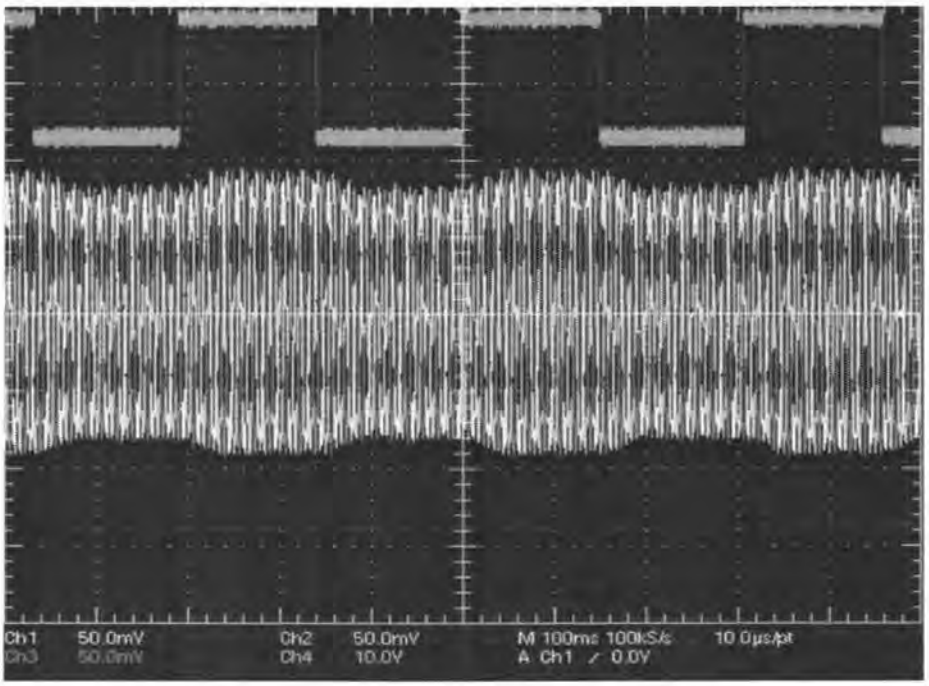

(b) Function generator control signal (top) and three-phase stator current (bottom) after applying the torque pulsations

Fig. 2.23: Dynamometer control circuit

Various ranges of torque pulses frequencies are illustrated in Fig. 2.24. Torque pulses are not visible beyond the rotor rotational speed, but can be effectively monitored within the 1st order eccentricity sidebands envelope, as indicated in Fig. 2.24 (a). There is always a probability of obstructing the rotor fault signal when it is associated with torque pulses at the same oscillating frequency around the air-gap. Practically, high ratios of load oscillations might be experienced and hence introduce a lack of fault detection effectiveness.

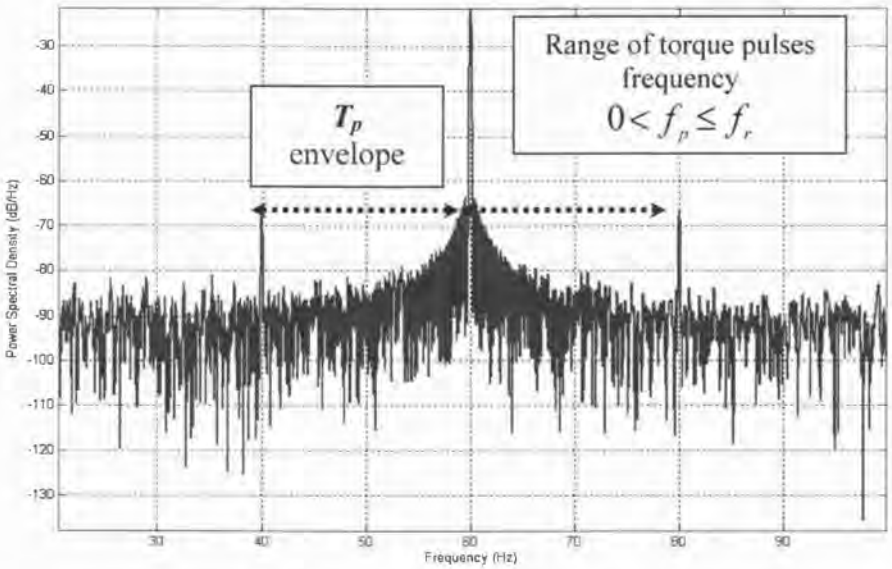

(a) Torque pulses frequency range

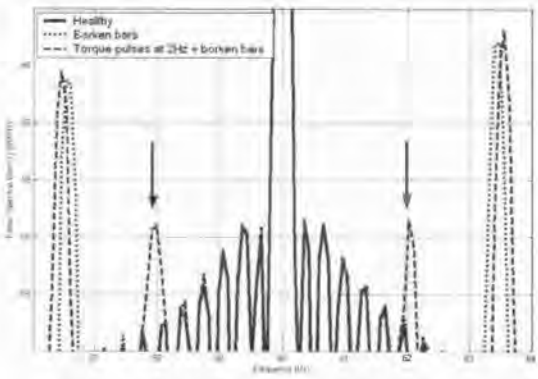

(b) Torque pulses at 2 Hz

$$T_{load} = T_{avg} + \cos(0.1\theta_{rm})$$

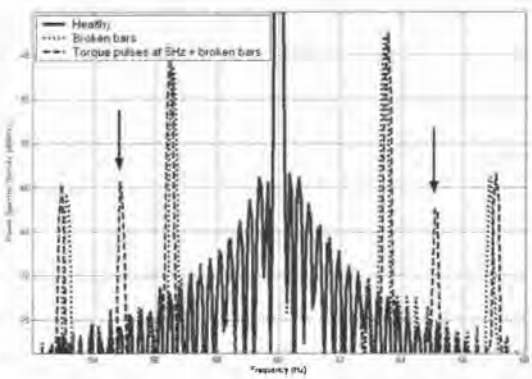

(c) Torque pulses at 5 Hz

$$T_{load} = T_{avg} + \cos(0.25\theta_{rm})$$

Fig.2.24: 1 N.m torque pulses at different frequencies during four broken bars condition

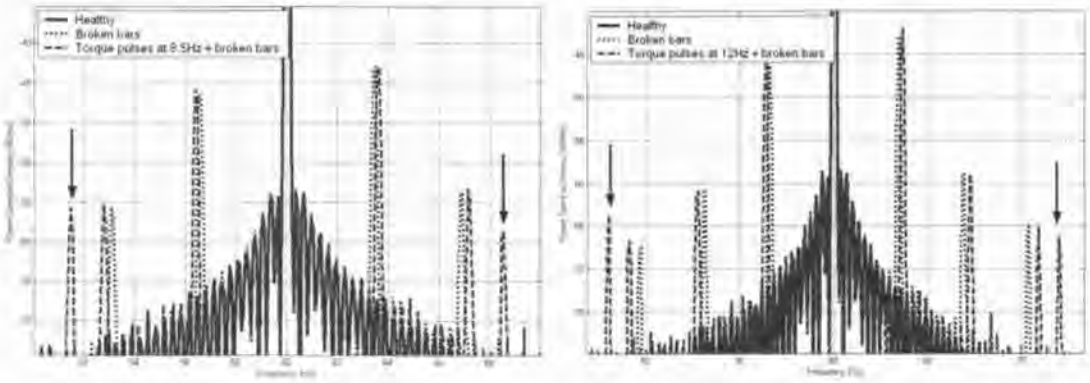

(d) Torque pulses at 8.5 Hz

$$T_{load} = T_{avg} + \cos(0.425\theta_{rm})$$

(e) Torque pulses at 12 Hz

$$T_{load} = T_{avg} + \cos(0.6\theta_{rm})$$

Fig.2.24 (cont.): 1 N.m torque pulses at different frequencies during four broken bars condition

The time-domain signal has common characteristics between load and broken bar torque pulses. Amplitude demodulation of the stator current wave can provide a preliminary fault diagnostic tool as shown in Fig.2.25 (a). The stator current of the form

$$i_s(t) = m(t)\cos(2\pi f_s t) \quad (2.22)$$

where $i_s(t)$ is the stator current waveform and $m(t)$ is the stator current amplitude. The filtered $m(t)$ carries useful information about the status of the monitored machine.

$$m(t) = 0.5\, A_m \cos(2\pi f_{sb} t) \quad (2.23)$$

where A_m is the peak-to-peak amplitude of $m(t)$ at a frequency of f_{sb}. The magnitude of torque pulses (A_p) due to fault or load oscillations are proportional to A_m as shown in Fig.2.25 (b). Moreover, the frequency of $m(t)$ at f_{sb} is exactly equal to double the slip frequency in the case of a broken bar fault, $f_{sb} = 2sf_s$, or the load oscillation rate, $f_{sb} = f_p$.

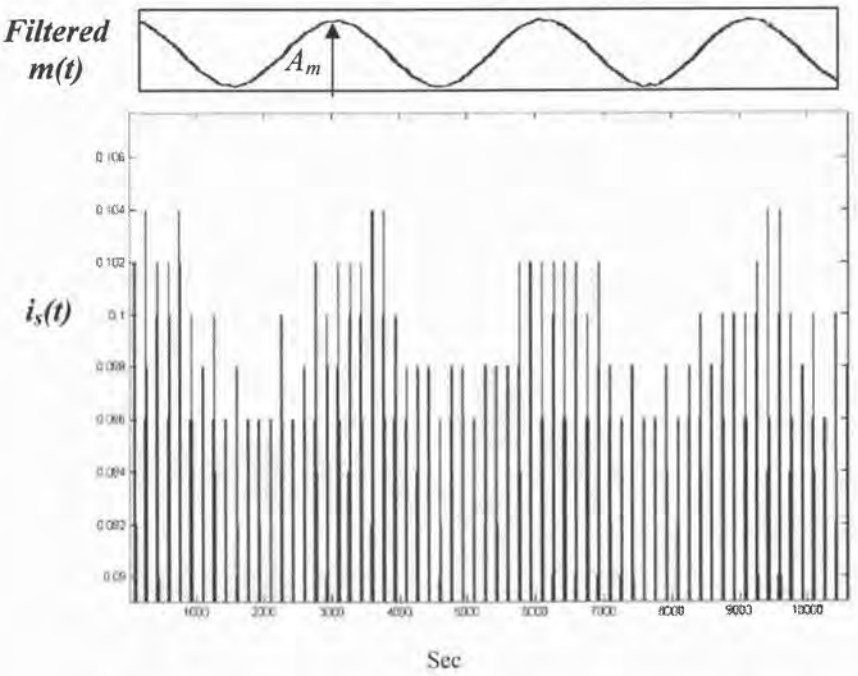

(a) Time demodulation of stator current amplitude signal

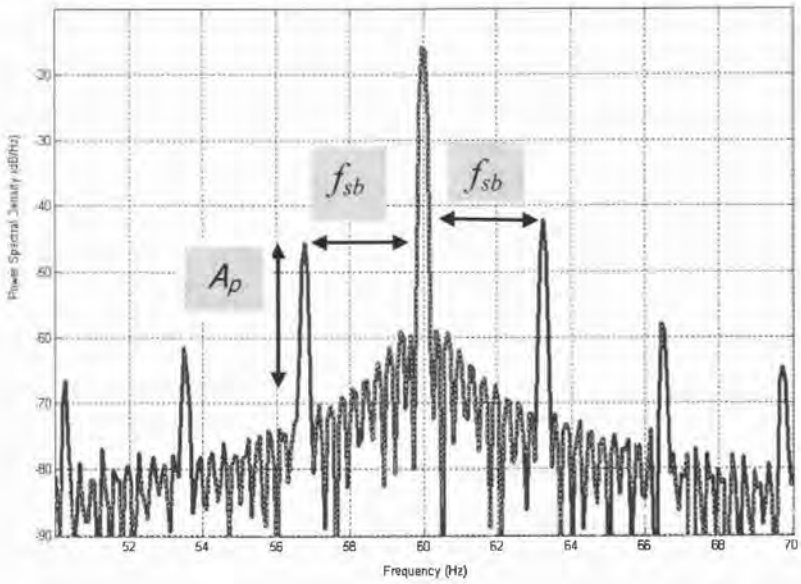

(b) Frequency demodulation of stator current signal

Fig.2.25: (a) Time domain-based analysis of stator current amplitude signal

The time-domain method only senses the existence of any available torque pulses in a motor without providing predictability of the exact source of torque pulses. It is similar to vibration monitoring, which is commonly used for detection of mechanical unbalance in the machine. All of these methods are of limited benefit in separating fault components from irrelevant signals of coupled load or other external frequency sources.

Nevertheless, spectral analysis of the stator terminal current might run into similar limitations as shown in Fig. 2.26. Here it is difficult to distinguish between broken bar sidebands in (a) and load torque pulses in (b).

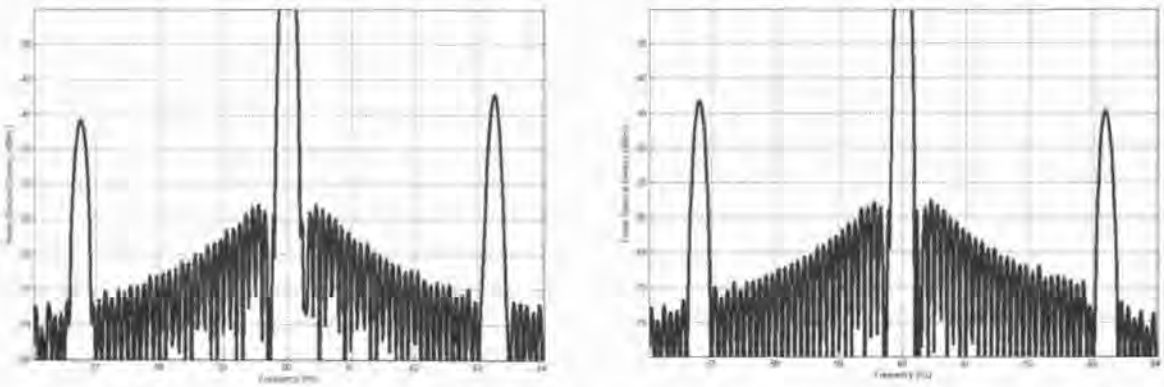

(a) Four broken bars (b) Torque pulse at 3.2 Hz

Fig. 2.26: Power spectrum density of stator current sidebands

Some fault diagnostic procedures can be implemented to solve the fault separation problem. To some extent, sideband frequency monitoring is a practical diagnosing method. Frequency movement of sidebands throughout multiple loading points is obvious in the case of broken bar faults, as shown in Fig. 2.7, while other sidebands caused by load or external vibration source are fixed in space, as shown in Fig. 2.27. The observation of this distinctive behavior leads to the derivation of a characteristic feature only applicable to variable load operations. In industrial environments, the limitation of sideband frequency monitoring still exists because of operational restrictions that prohibit the variation of some critical loads coupled to high-cost processes. Therefore, the goal is

to probe the feasibility of utilizing spectral analysis that causes the least possible intrusion while maintaining high accuracy.

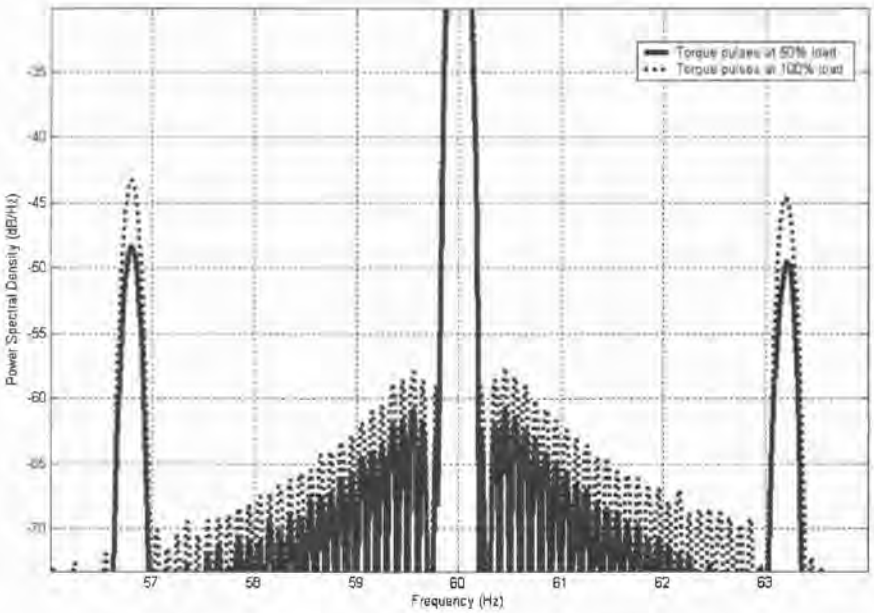

Fig. 2.27: Torque pulses at 50% and 100% loading points

Studying the reactions of sideband amplitudes can anticipate imminent machine or load related deficiencies more practically. However, direct extension of the spectral estimation technique to only a single phase of the stator current is infeasible due to the aforementioned reasons. Therefore, deploying a three-phase current-based technique is the underlying scheme of modern fault diagnostics systems, which are capable of investigating the interaction between the negative-sequence harmonics from rotor faults and the positive-sequence harmonics from a load oscillation.

Fig. 2.28 shows that rotor asymmetries create a series of positive- and negative-sequence reactions. These reaction loops induce speed ripples, torque pulses and consequently stator current sidebands at various time and position harmonics, while load torque pulses generate only positive-sequence at multiple frequency values. Extending the positive- and negative-sequence analysis to the three-phase currents is evidently an effective tool. The 1st order sidebands of the q-component of stator current have unique amplitude behaviors observed by applying a negative-sequence conversion matrix (equation 2.10) and positive-sequence conversion matrix:

$$\begin{bmatrix} i_{a1} \\ i_{b1} \\ i_{c1} \end{bmatrix} = \frac{1}{3}\begin{bmatrix} 1 & a & a^2 \\ a^2 & 1 & a \\ a & a^2 & 1 \end{bmatrix}\begin{bmatrix} i_a \\ i_b \\ i_c \end{bmatrix}, \; a = e^{j\frac{2\pi}{3}} \tag{2.24}$$

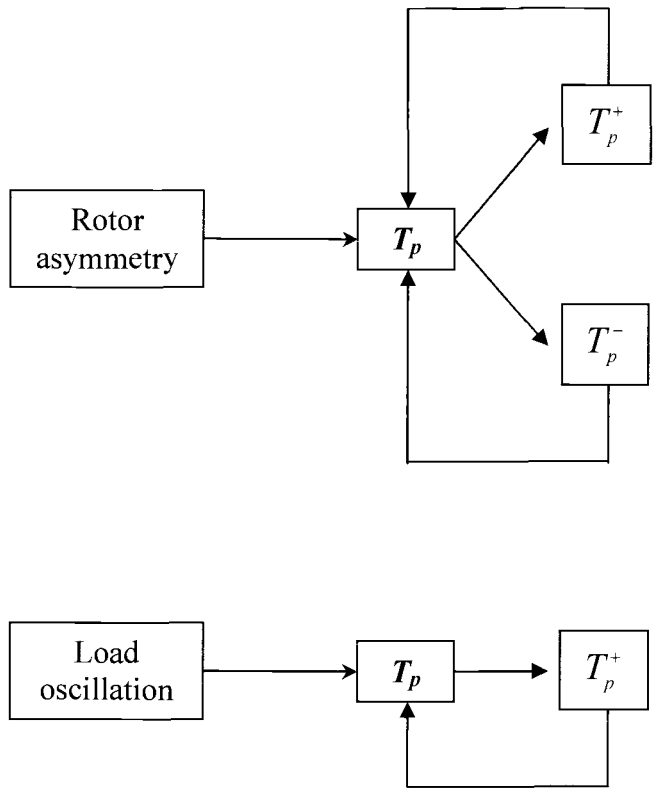

Fig. 2.28: Reaction loops due to broken bar fault and load oscillation

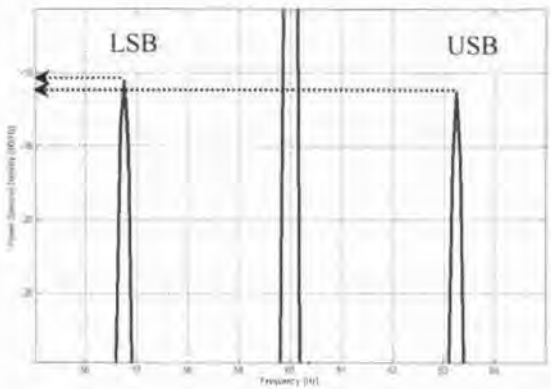

(a) Negative-sequence of broken bar (i_{qs2})

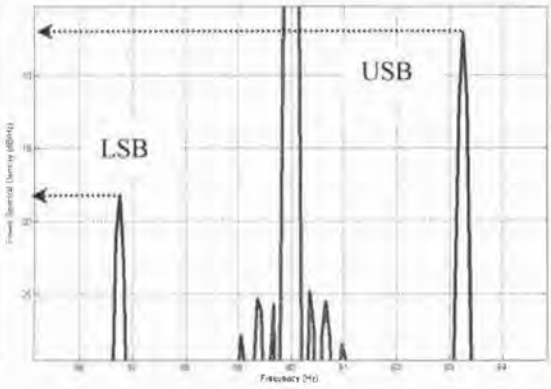

(b) Positive-sequence of broken bar (i_{qs1})

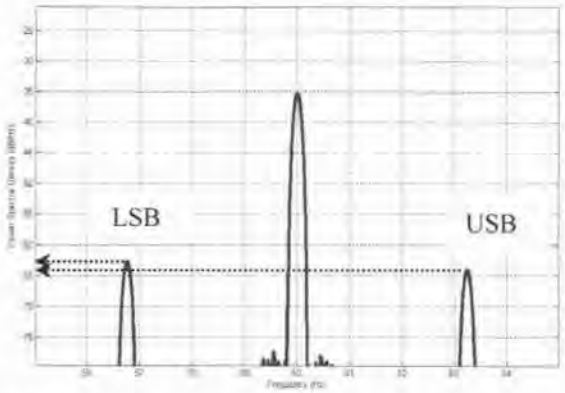

(c) Negative-sequence of torque pulse (i_{qs2})

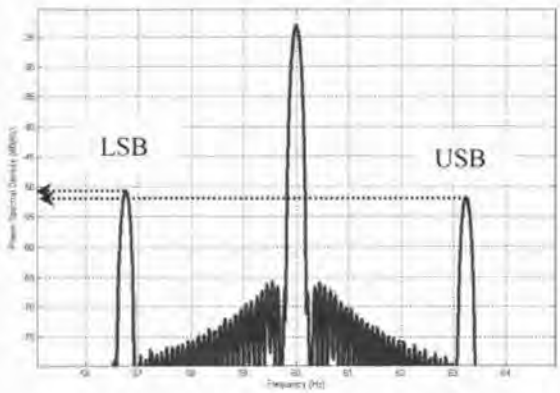

(d) Positive-sequence of torque pulse (i_{qs1})

Fig. 2.29: Analysis of q-component of stator current

By monitoring the difference between the positive- and negative-sequences sidebands of the broken bar tangential components, as in Fig. 2.29 (a) and (b), it is possible to observe equal negative-sequence *q-axis* (i_{qs2}) sidebands due to the identical reaction of both LSB and USB. The reaction loop of these sidebands has consistent equal amplitudes, which form higher order sidebands with nearly similar behaviors. However, these sidebands are not of particular concern compared to the main LSB's and USB's. Referring to equation (2.2) and the negative-sequence (i_{ds2}) sidebands in Fig. 2.12, the severity of the broken bar fault is independently extracted from speed ripples and load

inertia. Fig. 2.29 (b) shows a clear difference between LSB and USB because of the severe reduction of the LSB positive-sequence (i_{qs1}) that is mainly affected by negative-sequence torques from the fault, as in Fig. 2.29 (a) and (b). The positive-sequence sidebands aligned with the tangential axis have an inconsistent reactions loop at the USB because of partially incorporated speed ripples at $2sf$ frequency.

In contrast, torque pulse sidebands have a unique behavior when deriving their negative- and positive-sequence tangential components, as shown in Fig. 2.29 (c) and (d). The LSB and USB sidebands are always identical to each other. This leads us to derive another characteristic feature which can assist the fault separation process. Yet, due to the insufficiency of torque filtration used in Fig. 2.29 (c), the torque pulses are not effectively removed from the signal. Therefore, the only comparison of the positive-sequence of the *q-axis* current is considered. However, another limitation can arise when torque pulses overlap with the rotor fault signal. In this situation, comparing only a positive-sequence analysis of the three-phase current, as shown in Fig. 2.29 (b) and (d), is inadequate. Chapter 6 discusses an alternative approach for the separation of rotor faults.

3. Speed Estimation: Current Signature Method

The aim of fault detection and classification of an IM that causes the least possible interference while maintaining high accuracy leads to the investigation of possible methods to estimate the rotor speed of the IM. Modern sensorless control approaches of IM suggest avoiding physical proximity or contact during rotor speed estimation.

Current signature is an established alternative approach for speed estimation. This technique provides a high accuracy estimation of the steady state speed of an IM by analyzing the eccentricity sidebands caused by rotor irregularities, as shown in Fig. 3.1. As per reference [9], this method is mainly utilized to calculate the time variation of the magnitude of the stator-rotor mutual inductance. Moreover, the $(2\text{-}s)f_s$ sideband in the stator current still can measure the rotor speed since three-phase induction machines do not generate a second harmonic from the fundamental. However, this sideband amplitude was not consistent during experiments and was not clear during dynamic eccentricity tests as illustrated in Table 2.2. Hence, this component has been disregarded during this study.

Regardless of the number of induction machine poles, the first order dynamic eccentricity sidebands are constantly detectable because of the nonlinear relationship between mutual inductance and the length of the air-gap [9]. Therefore, these sidebands are always prevailing in the stator current signature, resulting in not only accurate speed estimation but also fault detection and classification techniques.

The above discussion is proven experimentally as illustrated in Fig. 3.2 and 3.3, where accurate speed values were extracted while varying the operating conditions of the test motor. The terminal voltage of the machine was varied to provide a wide-range of speed points in order to verified the robustness and accuracy of the current signature method.

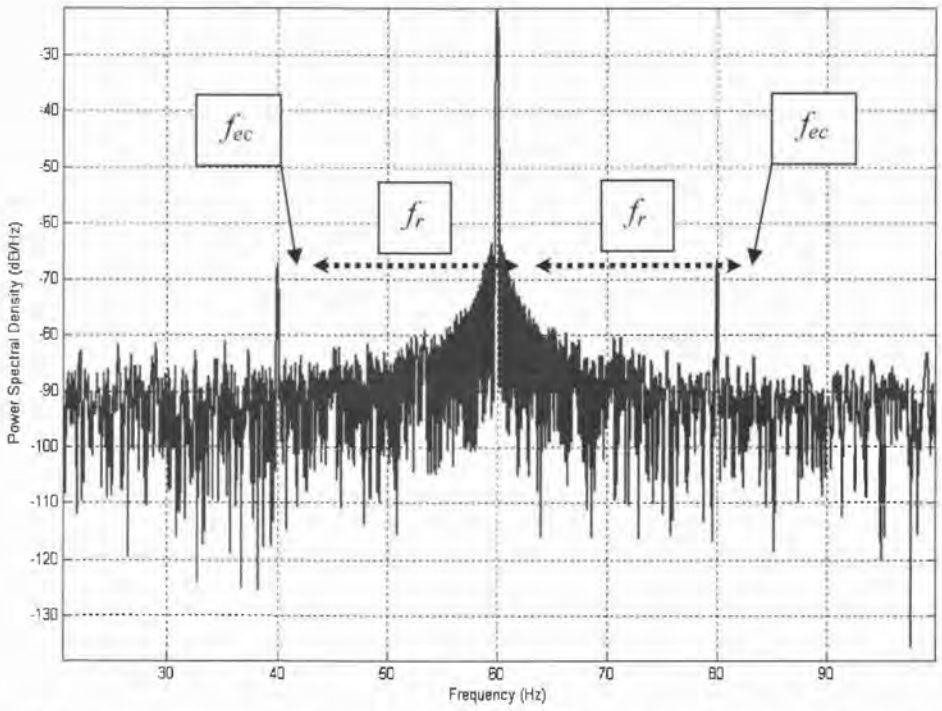

Fig. 3.1: Speed extraction from 1st order eccentricity sidebands (f_s+f_r) and (f_s-f_r)

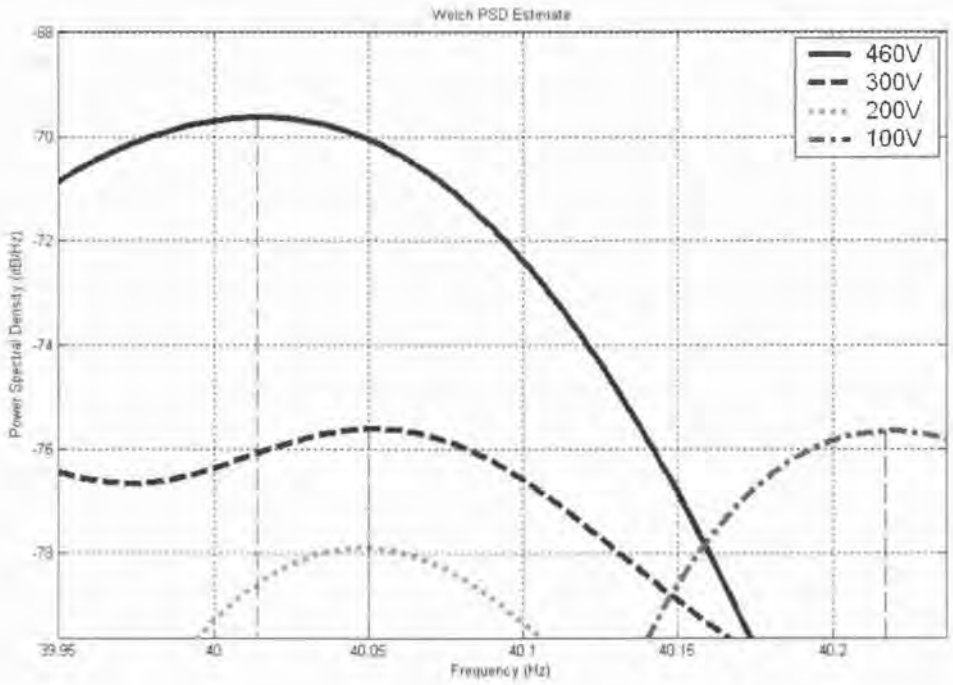

Loading (N.m)	Terminal voltage (V)	Frequency component (Hz)	Measured speed (rpm)	Estimated speed (rpm)	Error (rpm)
0	100	40.217	1187	1188	1
0	200	40.05	1197	1197	0
0	300	40.05	1197	1197	0
0	460	40.017	1199	1197	2

Fig. 3.2: Comparison between speed measurement and estimation during reduced terminal voltages of an uncoupled motor

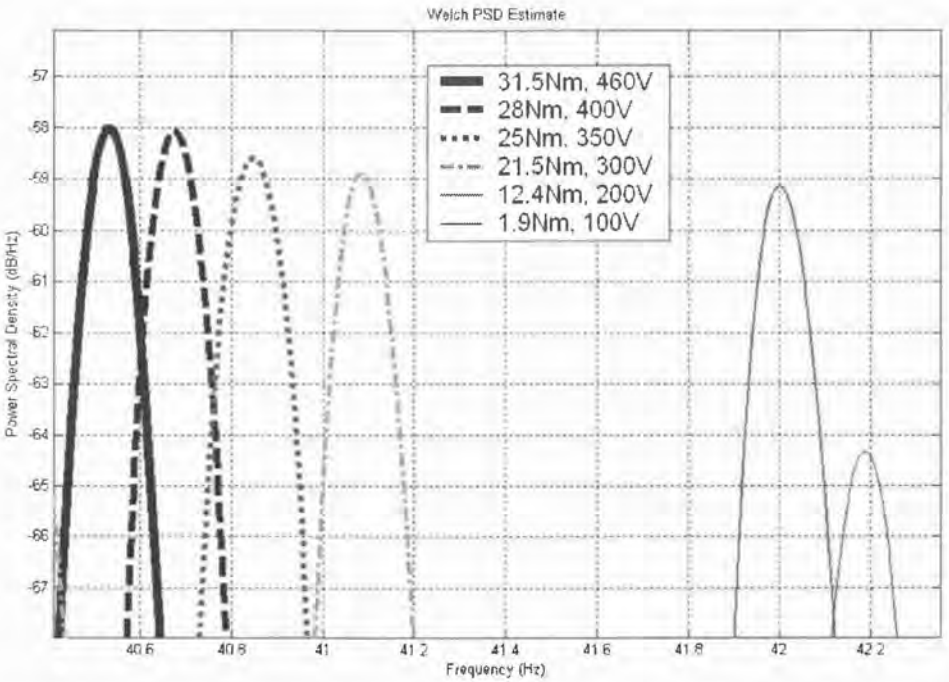

(The speed at 100V was the lowest possible since increasing the slip beyond the limits caused excessive rotor heating due to high rotor current.)

Loading (N.m)	Terminal voltage (V)	Frequency component (Hz)	Measured speed (rpm)	Estimated speed (rpm)	Error (rpm)
1.9	100	42.188	1068	1068.7	0.7
12.4	200	42	1078	1080	2
21.5	300	41.1	1135	1134	1
25	350	40.85	1149	1149	0
28	400	40.7	1159	1158	1
31.5	460	40.55	1167	1167	0

Fig. 3.3: Comparison between speed measurement and estimation during reduced terminal voltages of coupled motor

4. Universal Fault Index Using Dynamic Eccentricity Sidebands

The objective of this chapter is to thoroughly analyze the stator current signature in order to develop a global wellness measure for an IM. Much research has been done to investigate fault detection techniques so far. Yet, the assessment of the actual fault has many aspects that necessitate the monitoring of various sidebands around the fundamental or slot-passing frequencies. The following two sections examine the proposed method of fault assessment and its respective specifications. This initiative seeks out a reliable and pure universal index for rotor asymmetry conditions.

4.1. Fault detection

Rotor asymmetries generally inflict different electrical, electromagnetical, or mechanical machine quantities that result in vibration, acoustic emission, or poor efficiency. Inquisitive fault investigation is necessary for determining the exact cause of rotor fault that, if not alleviated or counteracted, can spread and increase fault severity or cause severe motor degradation.

Of course, sudden failure of a critical motor coupled to a high-volume, high-cost process is not an option. Therefore, the scope of a practical fault detection system should be to pinpoint anomalous situations in the monitored machine by utilizing the least possible raw data while maintaining high quality standards of the detection procedure. Moreover, the system should have the capacity to adopt many aspects of noise immunity against internal or external parameters related to an IM reaction during motor fault, coupled load torque pulse injection, or time-harmonics and fluctuations of machine supply, as will be discussed in Chapter 5.

The objective of this thesis is to correlate, between rotor faults and rotor irregularity, measures through a wide range of loading points and different source and load conditions, verifying the detection capabilities of the proposed method. In the frequency domain, the amplitude and frequency reactions of dynamic eccentricity sidebands are the key determinants of rotor condition.

Current signature analysis: The implementation of frequency domain monitoring of a one-phase stator current still can be more useful. The reason lies in the fact that one-phase monitoring is a cost-effective yet accurate diagnostic tool when clear data is provided about the integrity of the load or supply quantities. In practice, this assumption is not always valid and some external fluctuations are not preventable. However, in spite of initially considering the whole system frame work, stator current raw data from a sigle-phase sensor need to be used more effectively. From the noise filtration perspective, fault signal separation entails a three-phase monitoring of electrical quantities for the purpose of determining voltage, current unbalance or negative-sequence mean values. Namely, the $(f_s\text{-}f_r)$ frequency is the prime element in this discussion as proven theoretically and experimentally in Chapter 2; this component is more sensitive than any other to rotor asymmetries.

Vibration monitoring of eccentricity: Either inherent or exerted irregular levels of eccentricities might exist in the machine and may be mixed together. Traditional techniques of vibration monitoring cannot effectively filter static eccentricity vibration because it has a steady pull in one direction and is independent of rotor rotational speed (w_r), therefore it will not cause any associated vibrations in the stator case. The diagnosis of motor static eccentricity requires special experimental equipment that is beyond the ability of current on-line monitoring techniques.

Dynamic eccentricity vibration behaves uniquely from no-load to full-load conditions of the motor where the rotational speed vibration is decaying as shown in Fig. 4.1 and in Table 4.1, in contrast to normal condition vibration. This eccentricity pattern is fundamentally important because it can explain current dynamic eccentricity (or current eccentricity) sidebands during the same range of loading points.

Fault detection technique: The experimental work put forward shows that it is possible to use the stator current sideband at $(f_s\text{-}f_r)$ as a reliable rotor fault index as it was noticed that this component's amplitude is a measure of irregularities induced in the air-gap. That behavior was analogous to the dynamic eccentricity vibration curve shown in Fig. 4.1. The proposed fault detection technique deploys the rotor eccentricity concept as a universal measure of rotor bar and radial force asymmetries due to their relative eccentricity reaction at the prevailing sidebands primarily at $(f_s\text{-}f_r)$.

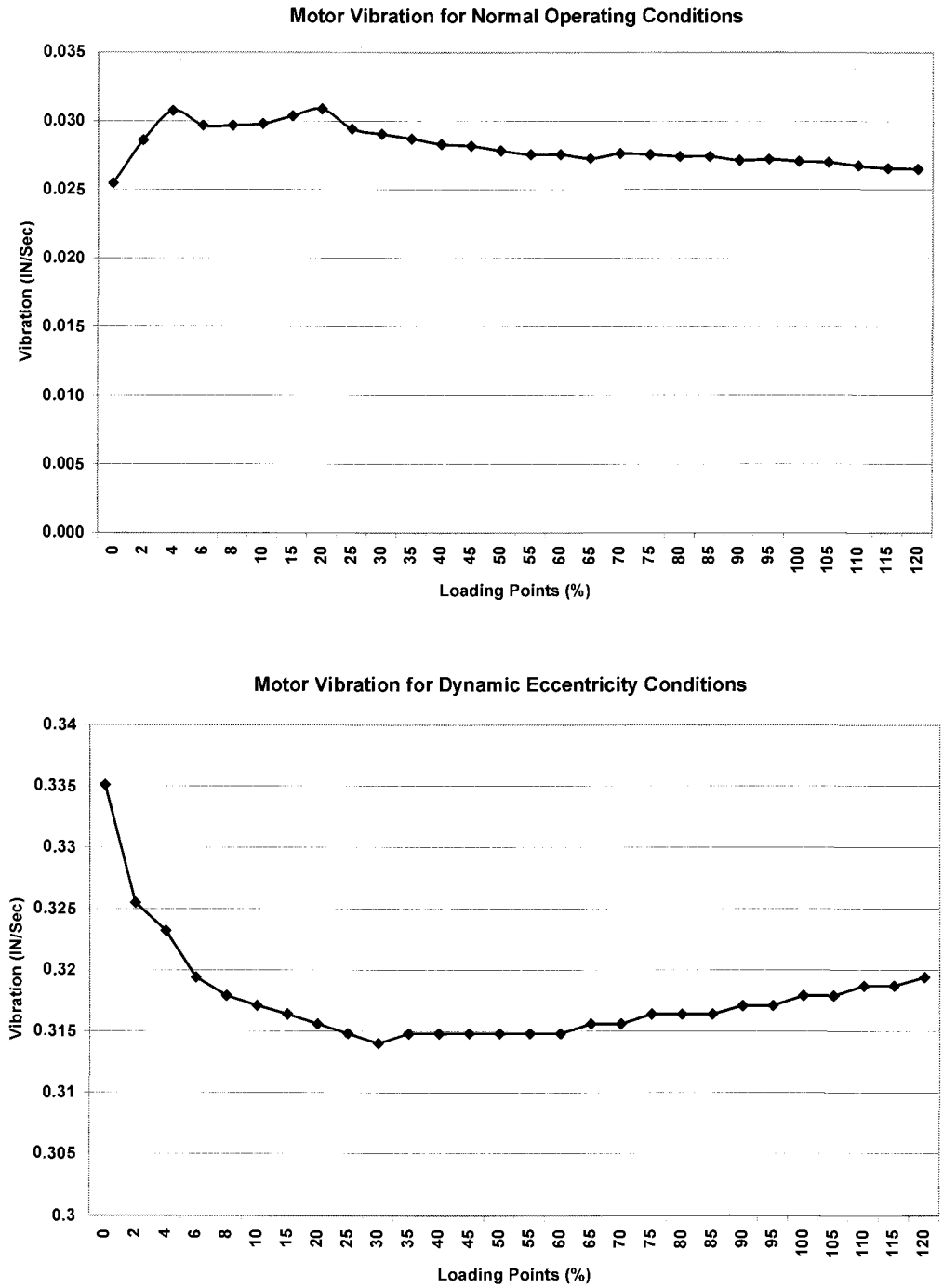

Fig. 4.1: Comparison between normal and dynamic eccentricity vibration values from no-load to full-load conditions

Table 4.1
Normal and dynamic eccentricity vibration monitoring

Loading %	Normal Vibration (IN/Sec)	Dynamic Eccentricity Vibration (IN/Sec)
0	0.02546	0.3351
2	0.0286	0.3255
4	0.03076	0.3232
6	0.02968	0.3194
8	0.02968	0.3179
10	0.02981	0.3171
15	0.03038	0.3164
20	0.03088	0.3156
25	0.02943	0.3148
30	0.02903	0.314
35	0.0287	0.3148
40	0.0283	0.3148
45	0.02817	0.3148
50	0.02783	0.3148
55	0.02755	0.3148
60	0.02755	0.3148
65	0.02727	0.3156
70	0.02762	0.3156
75	0.02755	0.3164
80	0.02741	0.3164
85	0.02741	0.3164
90	0.02713	0.3171
95	0.0272	0.3171
100	0.02706	0.3179
105	0.02699	0.3179
110	0.02671	0.3187
115	0.02656	0.3187
120	0.02649	0.3194

Contrary to the ideal assumption illustrated in Fig. 2.6, the practical rotor-stator mutual inductance in the air-gap is affected by the amount of loading and hence the magnetization current varies accordingly. This is due to the time-variation of mutual inductance, which is inversely proportional to the air-gap length where any geometrical variation of air-gap length causes time spectral components in the stator current. Referring to the eccentricity model derived in Fig. 2.14, both static and dynamic eccentricities can be represented by incorporating a static Fourier series and another rotating Fourier series modulated by the rotor speed [9]. Therefore, the stator current reflects the total Fourier series contents associated with the rotor surface and can be considered as an eccentricity measure at relative frequencies.

As illustrated in Fig. 2.22, time-varying magnetic field anomalies can cause an increase in the fundamental stator current only if associated with a broken bar fault or load oscillation conditions. However, the gravity of the eccentricity components can reflect any air-gap variations related to:

- motor efficiency discrepancies caused by rotor bar fault mechanisms that tend to reduce rotor current and demand more stator current and also,
- fluctuation of the radial rotor flux (*d-axis*) due to eccentricity.

These effects can be described by the following relation.

$$\lambda_{dr} = L_m . i_{ds} \qquad (4.1)$$

where λ_{dr} is the rotor flux linkage aligned with the *d-axis*, L_m is the air-gap mutual inductance and i_{ds} is the stator current aligned with the *d-axis*. Large variations in the air-gap length apparently scatter the mutual inductance values. Therefore, the steady-state rotor flux (B_r in Fig. 2.21) is affected proportionally by the air-gap mutual inductance variations resulting in inconsistent rotor current densities. Consequently, the stator current responds to the same Fourier series components associated with rotor eccentricity shown in Fig. 4.2.

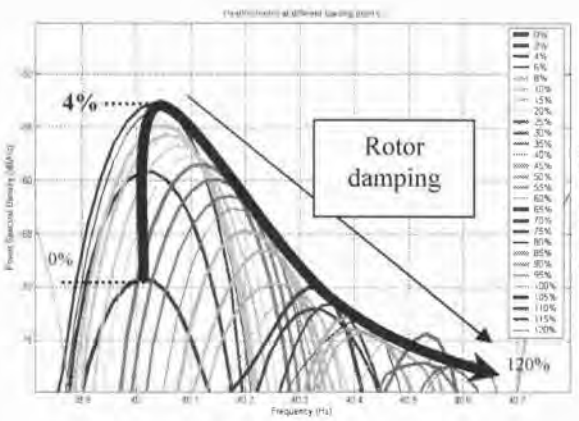

(a) Normal operating case

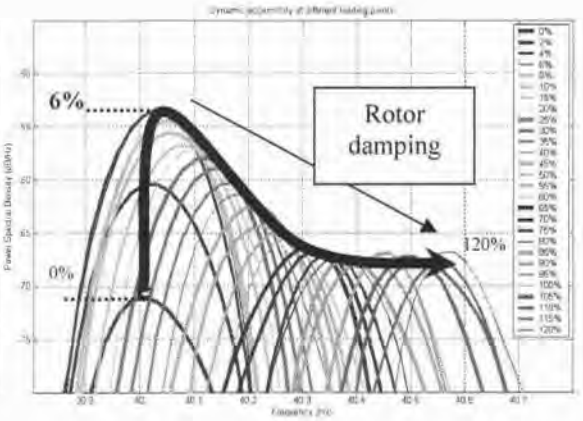

(b) Dynamic eccentricity case

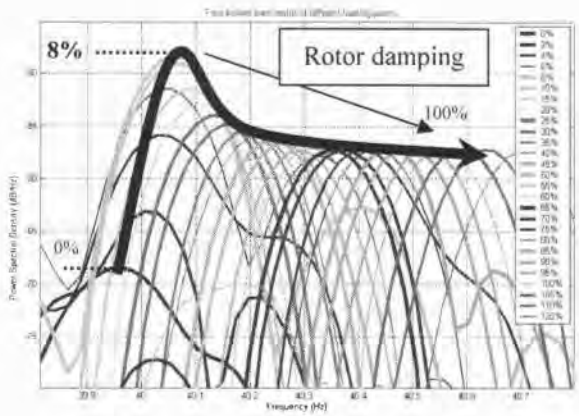

(c) Four broken bars case

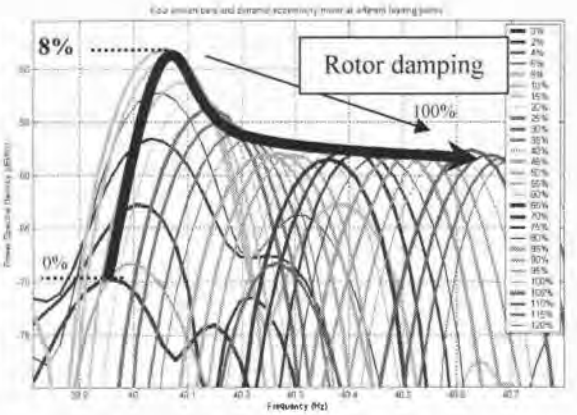

(d) Four broken bars and dynamic eccentricity case

Fig. 4.2: Amplitude envelopes of the $(f_s\text{-}f_r)$ through twenty-eight loading points due to normal and different rotor asymmetry conditions in frequency domain at frequency resolution $\Delta f = 0.019$ Hz, poles = 6 and rotor bars = 42

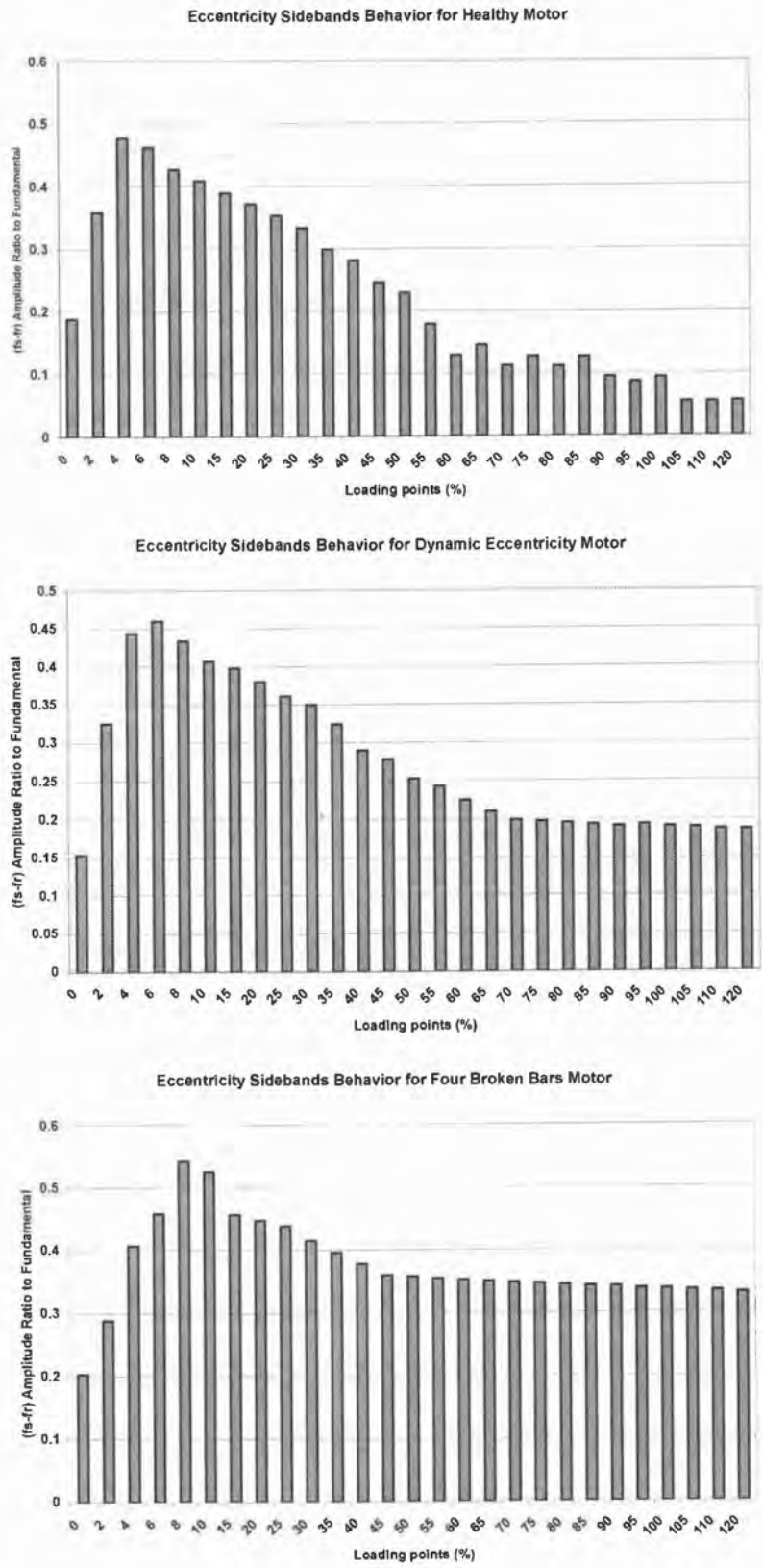

Fig. 4.3: Relative ratios of eccentricity sidebands at $(f_s\text{-}f_r)$

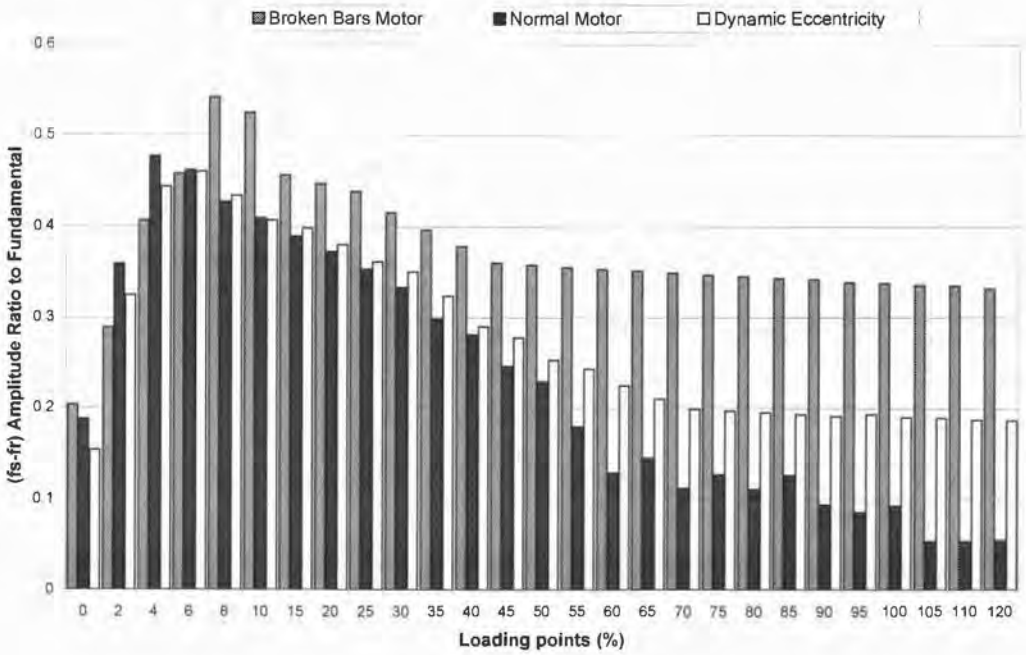

Fig. 4.4: Comparison of $(f_s\text{-}f_r)$ Ratios

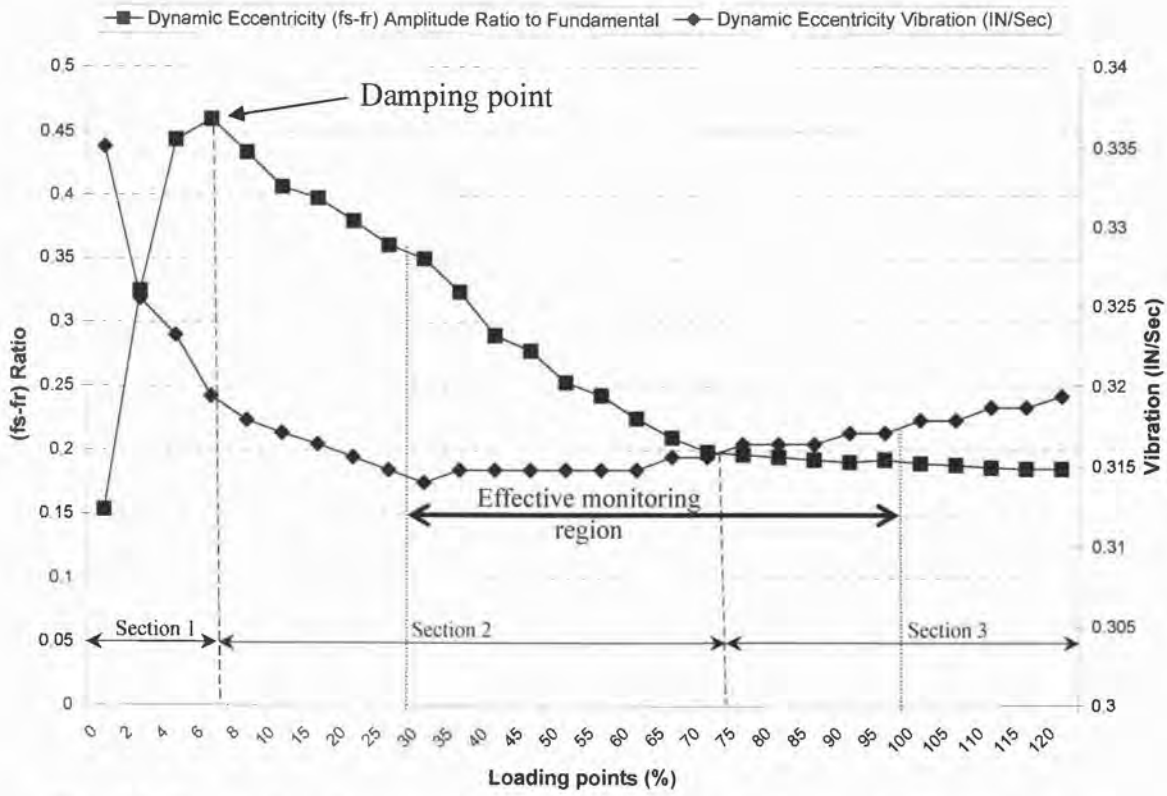

Fig. 4.5: Comparison between dynamic eccentricity vibration and current signature at $(f_s\text{-}f_r)$

Four different rotor asymmetry cases have been extracted by capturing the behavior of the eccentricity sideband at (f_s-f_r) during twenty-eight loading points. The sideband is shown in Fig. 4.2 (a), (b), (c) and (d) that each case has an unique behavior as measured by different rotor damping rates exerted on UMP radial forces. By comparing these different behaviors, as in Fig. 4.3 or 4.4, one can notice the amplitude behavior proportional to the amount of irregularities in the rotor, where the rotor cannot damp effectively the (f_s-f_r) amplitude if the eccentricity level increases by a fault.

It is important to study the commonalities observed in Fig. 4.5 when comparing between dynamic eccentricity vibration and (f_s-f_r) amplitude at the same level of eccentricity. The analysis will be based on three sections, which describe different rates of changes of motor parameters as seen in Table 4.2: rotor speed (w_r), rotor MMF wave amplitude and rotor flux density rate of change (dB_r/dy).

Table 4.2
Motor parameters rates of change during each loading section

Parameter	Rate of change at section 1	Rate of change at section 2	Rate of change at Section 3
w_r	Low decrease	Moderate decrease	High decrease
MMF	High increase	Moderate increase	High increase
dB_r/dy	High increase	Moderate decrease	Constant

Section 1: In this section, the dynamic eccentricity vibration curve is totally opposite to the (f_s-f_r) amplitude. This is because only that dynamic eccentricity can be measured using a vibration accelerometer. In contrast, all eccentricity forms that cause radial forces at spatial poles $p \pm 1$ forces are notably evaluated by the proportional stator current sideband (f_s-f_r). This is mainly due to the high increase in dB_r/dy reflected in the stator sideband during a sharp increase in rotor current at light loading stages. However, the technique is not sufficiently accurate/sensitive in this section.

At the end of this section, the damping of UMP force starts. Different values of loading points correspond to the rotor damping points at 4%, 6% and 8% due to normal, dynamic eccentricity, and broken bar cases respectively, as shown in Fig. 4.2. The reason resides in the increased irregularity values in rotor flux that increase $p \pm 1$ forces, so that the damping ability of the rotor decreases.

Section 2: This is a reaction to a moderate decrease of rotor w_r and MMF parameters; the dB_r/dy is gradually damped. As a result, the dynamic eccentricity vibration curve is decaying consistently to the $(f_s\text{-}f_r)$ amplitude. Similar to the traditional rotor bar fault detection, in this section the rotor current and MMF wave amplitude increase notably beyond the 30% loading point that eases fault detection process. As depicted in Fig. 4.4, the comparison of $(f_s\text{-}f_r)$ ratios associated with different faults is feasible.

Section 3: In this section, the rate of change of dB_r/dy is almost constant due to the imposed equilibrium caused by the opposite reactions of w_r rotor speed and MMF. However, sections 2 and 3 overlap during fault cases because of the high deceasing rate of w_r especially in the case of a broken bar condition that also requires an increase of the MMF due to poor motor efficiency. In the case of dynamic eccentricity, there will be less sections overlapping because the air-gap permeance is affected by eccentricity, not by the MMF wave.

From the standpoint of modern energy automation, a cost-effective utilization of motor energy is important at the full-load point. However, broken rotor bars to some extent govern the operation strategy of the defective motor. Assuming a healthy motor is in service, section 3 contains the optimum ranges of loading and consequently the most effective monitoring region due to the high values of rotor current.

Effective monitoring region: comparing Fig. 4.4 and 4.5, the effective monitoring range is from 30% to 100%. The over-loading points (100-120%) are excluded due to the excess MMF increase, which increases UMP radial forces and consequently increases stator case vibration. Therefore, the current signature behavior is not describing the dynamic eccentricity accurately but deviation between the $(f_s\text{-}f_r)$ ratios and dynamic eccentricity vibration is marginal and not expected due to the fact that the motor is usually not over-loaded. Nevertheless, by comparing the three fault types, it is

obvious that the fault detection and classification is valid from 30% to 120% of nominal load as evidently shown in Fig. 4.4.

4.2. Fault classification

The previous fault detection method proposed a new approach to capture rotor fault signals since checking limits are based on a visual or computer comparison between the (f_s-f_r) ratios at frequent surveillance periods. Conservative fault thresholds need to be set because this approach suffers from a wide variation in motor parameters even during normal operation. Moreover, the influence of a single component may propagate to other variables, introducing a confusion of alarms and hence complicate the fault classification process. So, in order to facilitate the classification of rotor faults, certain preventative measures need to be implemented to reduce misclassification error.

As illustrated in Fig. 4.6, rotor faults can be classified based on amplitude and the frequency positions of the 1st order eccentricity sideband. An increase of the (f_s-f_r) ratio to the fundamental frequency is classified as a permeance variation due to eccentricity or shaft misalignment, while an amplitude increase with rotor speed reduction is considered as a broken bar fault at the same loading point.

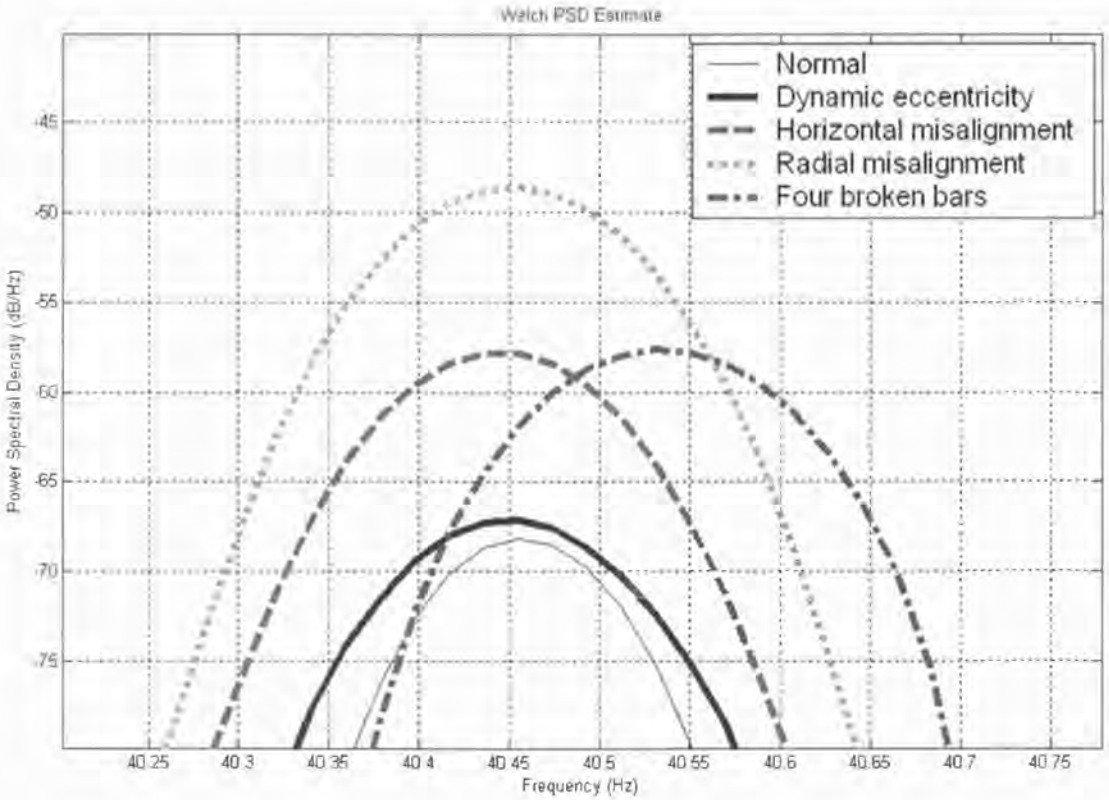

Fig. 4.6: Fault classification process based on amplitude and frequency positions of the 1st order eccentricity sideband (f_s-f_r)

The fault classification thresholds have previously been extracted on a sample by sample basis, as illustrated in Fig. 4.7. The characteristic fault curves show a good correlation in relative amplitudes and also in shape. The adequate fitting of such a sideband plot to the linear regression of the resulting data can be done as an equation to look up estimation values of fault severity. Based on this method, a practical tool for rotor faults diagnosis has been developed.

The amplitude and frequency data have been grouped into a wide range of loading points that restrict the validity of the proposed method to off-line applications. However, a few samples at the effective monitoring region may still be possible as process operations can adaptively vary certain parameters as required. Therefore, matching sidebands' characteristic amplitude and frequency can be mandated to confirm fault existence independent to any suspicious resonating vibration at a critical rotor speed creating a rotor "whirl" problem, for example.

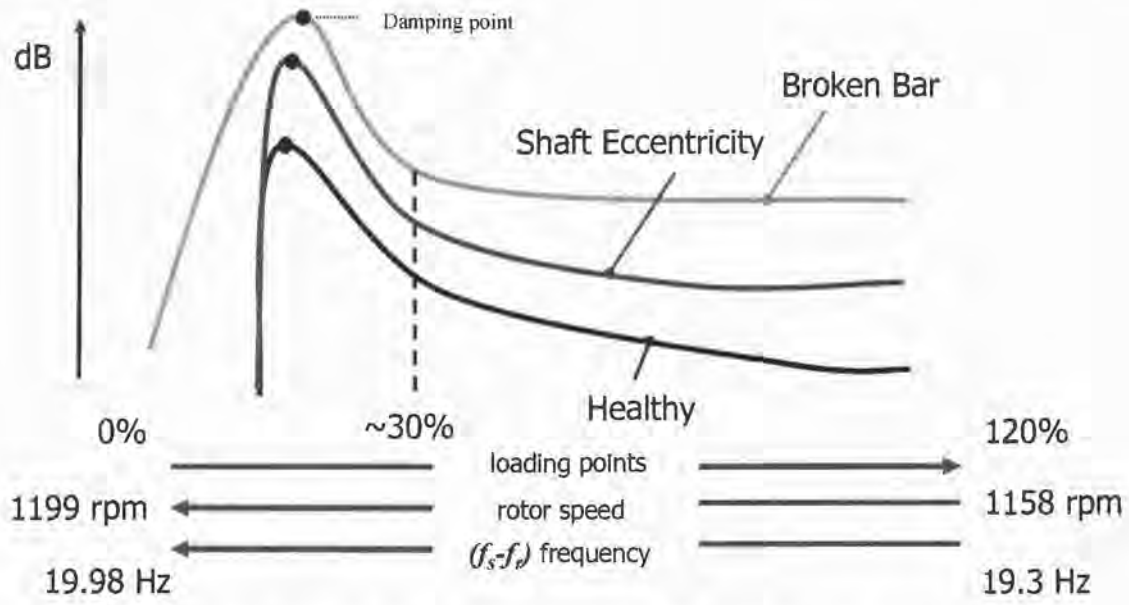

Fig. 4.7: Fault detection and classification thresholds

However, the effective monitoring region can successfully decide on the rotor condition by only a single sampling process in which a maintained loading point is considered. This process can be implemented by deriving two detection and classification features.

Feature 1: The detection and also the increment of fault severity can be observed by carefully monitoring the ratios of the (f_s-f_r) sideband to the fundamental frequency. From Fig. 4.8, the eccentricity and shaft misalignment feature is the ratio of the integral of the power spectrum density window around the (f_s-f_r) sideband (S) to that achieved from the fundamental. The increase of (S) at the same frequency components (f_{r1}) is considered an eccentricity or shaft misalignment that can be relatively quantified by (S_e) due mainly to vibration increase.

Feature 2: Similarly, the broken bar faults can be classified by monitoring the integral of the window (S_b) with an rpm shift due to a broken bar influence on the motor slip and hence efficiency. Due to rotor speed reduction, the feature harmonic will exist at

a new frequency (f_{r2}). The frequency resolution is the key element in deriving this feature in which high frequency resolution is required. Chapter 8 discusses this in more details.

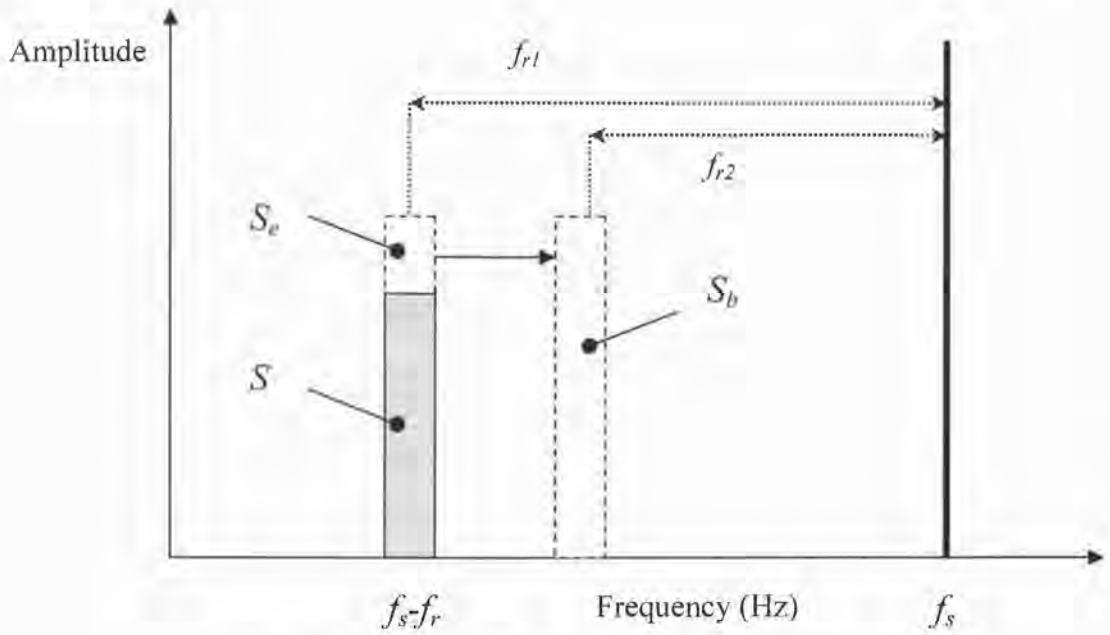

Fig. 4.8: Derived fault classification features

The schematic of the basic method by which a fault is detected and classified is shown in the block diagram in Fig. 4.9. In many industrial applications, torque transducers are not readily available and sometimes are not possible to install, since the shaft of the machine is difficult to reach (enclosure and housing) or inaccessible (submersible pumps). Therefore, in such settings, it is still a simple task to estimate the loading point of the machine by monitoring the amplitude of the stator current.

However, source or load arbitrary generations may influence the classification process. Therefore, the performance of the presented fault detection and classification scheme needs to integrate noise immunity procedures to eliminate misclassification errors. Chapter 5 discusses these aspects in more details and the optimal scheme will be presented.

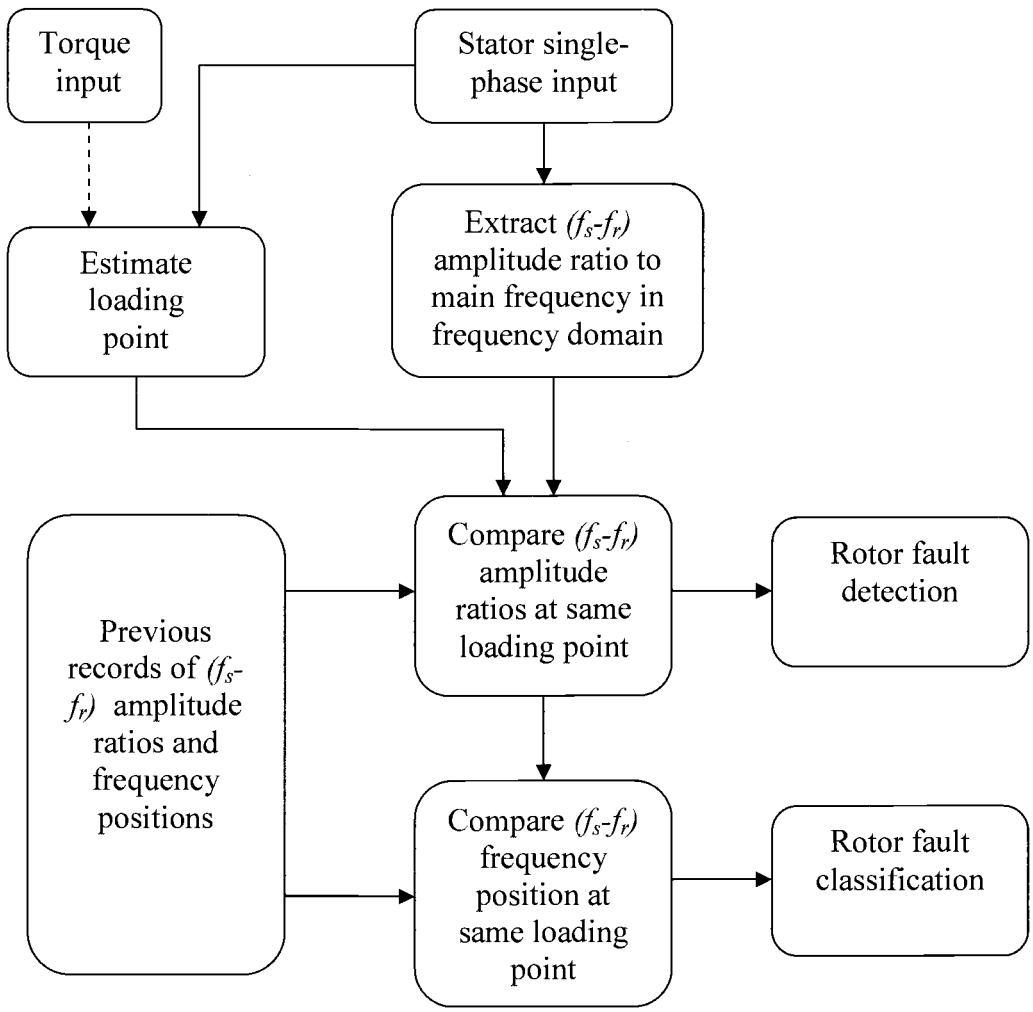

Fig. 4.9: Fault detection and classification process schematic

5. Influences of Arbitrary Conditions on Rotor Fault Detection And Classification

A motor is exposed to many electrical and mechanical stresses, and as a result of those stresses different faults can occur. In order to reduce unexpected failures and system breakdown it has become essential to detect incipient faults at their early development stages. During those stages, fault severity measures need to be sensitive and free of any other internal or external reaction components due to arbitrary conditions from supply or load.

It has been admitted that Variable Frequency Drives (VFDs) application can have some negative impacts in which fault detection becomes more complicated. The proposed diagnosing technique develops new monitoring characteristics at eccentricity sidebands. This technique is expected to have the advantage of excluding sidebands due to VFDs' small output frequency changes. However, VFDs may impose some noise effects on the eccentricity sidebands that are not experimentally evaluated yet. Core saturation, wave reflection on stator windings and harmonic distortions can be induced by the VFD and consequently obstruct fault signals. However, studying VFDs' influences on the eccentricity sidebands is not in the scope of this research.

The consideration of fault misinterpretation is of prime importance due to the above factors. The goal is to evaluate rotor fault signals while maintaining a high accuracy and implementing robust surveillance measures for an IM while maintaining the least possible sensor interference and a high efficiency of logarithmic computation.

5.1. Load oscillation

Load oscillation is a well-investigated effect in which frequencies of the load torque pulses can overlap with the fault indicator at (f_s-f_r), as discussed in session 2.3. Fig. 5.1 (a) and (b) depicts two examples where torque pulses can easily increase the magnitude of the eccentricity sideband obstructing and overwhelming the actual

measurements. Sometimes, the torque pulses are many times higher than the amplitude of the normal sideband, as in Fig. 5.1 (a). Moreover, they can deceivably magnify the fault signal, as shown in Fig. 5.1 (b). The fault separation from torque pulses is an extremely important and rich topic. Chapter 6 discusses this in more detail.

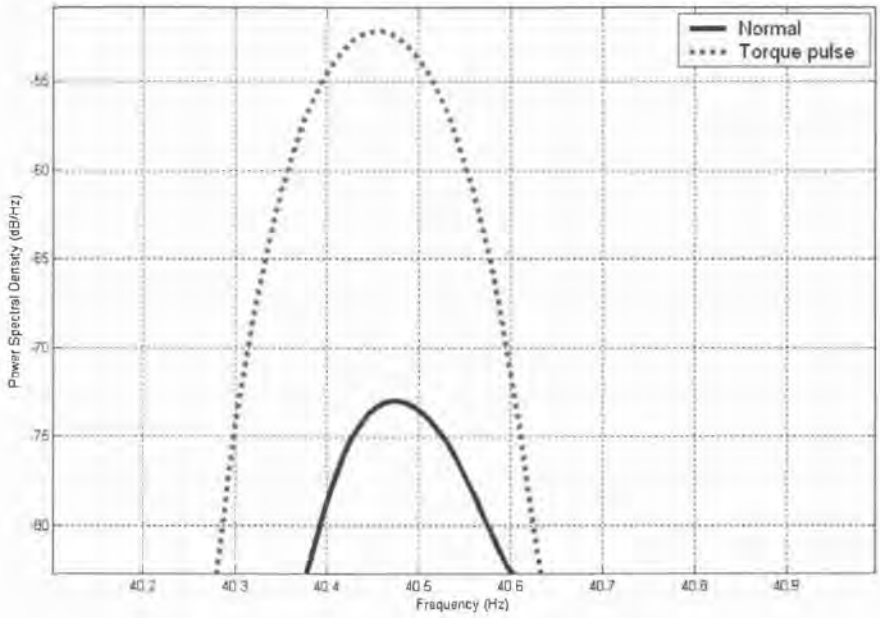

(a) Torque pulse at rotor speed at full load

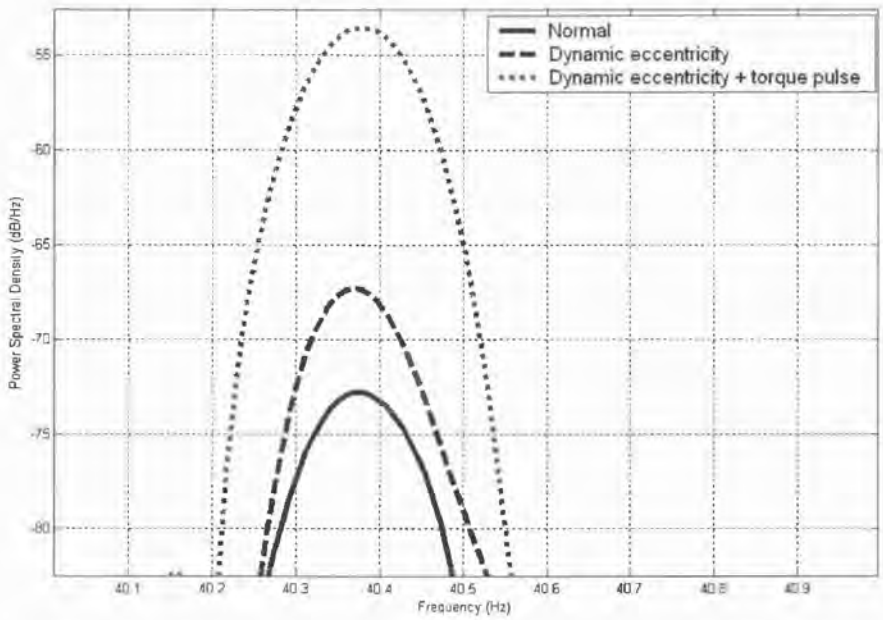

Fig. 5.1: (b) Dynamic eccentricity and torque pulse at rotor speed at 80% loading point

5.2. Stator current and motor efficiency relationship

The ultimate goal of fault detection and classification is to accommodate modern plant management and to police the standards of motor efficiency. Apparently, the broken rotor bar fault in particular reduces the output mechanical power of the motor, resulting in decreased motor efficiency. This is due to the aforementioned fact that the defective bar does not contribute the same torque. In similar situations, operating strategies are suggested to reduce stress on the adjacent bars that consequently carry more current. Also, the number of direct line starts and the loading level need to be reduced. Therefore, the motor efficiency from both an engineering and operational point of view is compromised.

The stator current inversely increases as rotor current decreases in the defective bar. Fig. 5.2 shows a clear deviation of the two current curves wherein the motor efficiency in the broken bars case decreases and entails more demand on the stator current as the motor is loaded.

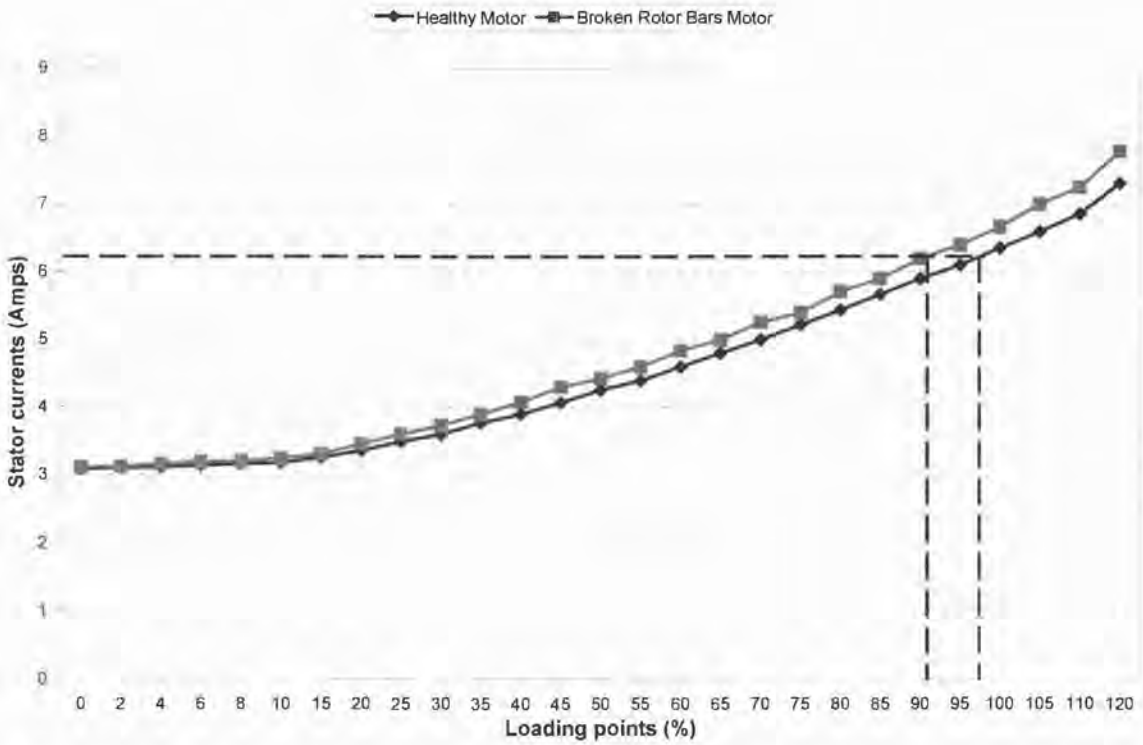

Fig. 5.2: Comparison between stator currents of healthy and four broken rotor bars motors

Example 5.1:

From motor experimental data in tables 5.1 and 5.2, the efficiency reduction due to four broken bars can be calculated as follows:

$P_m = 2.\pi.T_m.f_r$

The rotor speed at full-load of the healthy motor: f_r = 19.50 radian/sec (Hz).

The rotor speed at full-load of the defective motor: f_r = 19.45 radian/sec (Hz).

The output mechanical power of the healthy motor: P_m = 3.86 kW

The output mechanical power of the defective motor: P_m = 3.84 kW

The input power at full-load stator current (6.35 A) of the healthy motor: P_{in} = 3.95 kW

The input power at full-load stator current (6.66 A) of the defective motor: P_{in} = 4.14 kW

Therefore, the efficiency of the healthy motor: $\eta_{healthy}$ = 97.7 %, while the broken bars motor efficiency: η_{broken} = 92.75 %. The $\Delta\eta$ = 4.95% reduction is due to the fault of four broken bars.

Example 5.2:

By assuming no torque and speed transducers as in most IM applications, and utilizing only stator current magnitude as a load point indicator, the results are different as follows:

Some values have been approximated to match loading levels using the same stator current value (6.35 A as a full-load point based on healthy condition).

The rotor speed at full-load of the healthy motor: f_r = 19.50 radian/sec (Hz).

The rotor speed at full-load of the defective motor: f_r = approximately 19.49 radian/sec (Hz).

The output mechanical power of the healthy motor: P_m = 3.86 kW

The output mechanical power of the defective motor: P_m = 3.86 kW (based on the previous records of the healthy motor)

The input power at full-load stator current (6.35 A) of the healthy motor: P_{in} = 3.95 kW

The input power at full-load stator current (approximately 6.35 A as indicated in Table 5.2) of the defective motor: P_{in} = 3.95 kW based on 6.35 Amps monitored stator current magnitude to match previous record.

Therefore, the efficiency of the healthy motor: $\eta_{healthy}$ = 97.7 %, while the broken bars motor efficiency: η_{broken} = 97.7 %. The $\Delta\eta$ = approximately 0%. Estimating the motor loading point by only monitoring the magnitude of the terminal current may indicate misleadingly the same loading point. This can occur when the motor efficiency is calculated based on the horsepower rating from the motor nameplate that divided by the input motor power utilizing the monitored stator current magnitude. In contrast, Fig 5.2 shows different loading points at the full-load current value (6.35 A), which cannot be correctly distinguished without accelerometer.

The above example elevates the concern that a possible poor estimation of a loading point can occur using only stator current. Consequently, the broken bar fault may be misinterpreted as an eccentricity or shaft misalignment because of relative current magnitude and speed are unchanged although loading has been decreased due to the broken bars. In example 5.2, the frequency positions (f_r) of the eccentricity sidebands are evidently close to each other in the case of both healthy and broken bars, which makes the classification process in the frequency domain more complicated.

However, during the onset of a broken bar fault the rotor efficiency reduction is marginal. On the other hand, this may also introduce a misclassification error because the healthy and imminent broken bar conditions are very close in their frequency position. In similar cases, the fault characteristic of the (f_s-f_r) sideband ratio alteration (feature 1) must be the determinant of the fault detection scheme.

Table 5.1
Healthy motor data during various loading points

Loading Point (%)	Torque (N.m)	Stator Current (A)	Rotor Speed (rpm)	Slip Value	(f_s-f_r) Amplitude Ratio to Fundamental
0	0	3.09	1199	0.001	0.188
2	0.6	3.1	1198	0.002	0.359
4	1.3	3.11	1197	0.003	0.477
6	1.9	3.14	1197	0.003	0.462
8	2.5	3.16	1196	0.003	0.427
10	3.1	3.18	1196	0.003	0.409
15	4.7	3.26	1195	0.004	0.389
20	6.3	3.36	1194	0.005	0.372
25	7.8	3.49	1192	0.007	0.353
30	9.45	3.6	1191	0.008	0.333
35	11	3.77	1189	0.009	0.299
40	12.6	3.9	1188	0.010	0.281
45	14.2	4.07	1187	0.011	0.246
50	15.75	4.26	1186	0.012	0.229
55	17.3	4.4	1184	0.013	0.179
60	18.9	4.6	1183	0.014	0.129
65	20.5	4.8	1182	0.015	0.145
70	22.05	5	1180	0.017	0.112
75	23.6	5.22	1179	0.018	0.127
80	25.2	5.44	1177	6.400	0.111
85	26.8	5.67	1175	0.021	0.126
90	28.35	5.9	1174	0.022	0.094
95	29.9	6.1	1173	0.023	0.086
100	31.5	6.35	1171	0.024	0.093
105	33.1	6.59	1169	0.026	0.054
110	34.65	6.85	1167	0.028	0.054
120	37.8	7.3	1165	0.029	0.055

Table 5.2
Broken rotor bars motor data for 28-loading points

Loading Point (%)	Torque (N.m)	Stator Current (A)	Rotor Speed (rpm)	Slip Value	$(f_s\text{-}f_r)$ Amplitude Ratio to Fundamental
0	0	3.11	1199	0.001	12
2	0.6	3.12	1198	0.002	17
4	1.3	3.16	1197	0.003	24
6	1.9	3.19	1196	0.003	28
8	2.5	3.2	1196	0.003	32
10	3.1	3.25	1195	0.004	31
15	4.7	3.31	1194	0.005	28
20	6.3	3.46	1193	0.006	27
25	7.8	3.6	1192	0.007	26
30	9.45	3.73	1190	0.008	25
35	11	3.9	1189	0.009	24
40	12.6	4.08	1187	0.011	23
45	14.2	4.3	1185	0.013	22.5
50	15.75	4.43	1184	0.013	22
55	17.3	4.6	1182	0.015	22.1
60	18.9	4.84	1181	0.016	22
65	20.5	5	1179	0.018	22.2
70	22.05	5.26	1177	0.019	22
75	23.6	5.4	1176	0.020	22
80	25.2	5.71	1174	0.022	22.3
85	26.8	5.9	1172	0.023	22
90	28.35	6.2	1170	0.025	22.2
95	29.9	6.4	1169	0.026	22
100	31.5	6.66	1167	0.028	22.1
105	33.1	7	1164	0.030	22
110	34.65	7.24	1162	0.032	22.1
120	37.8	7.77	1158	0.035	22

5.3. Stator current unbalance

The stress on stator winding insulation is related to unbalanced motor currents, which leads to torque pulsations, increased vibrations, mechanical stresses and increased losses and heating of IM. The current unbalance is mainly caused by voltage unbalance, where the magnitude of current unbalance may be 6 to 15 times as large as the voltage unbalance, as shown experimentally in Fig. 5.3.

The linear interpolation, shown in Fig. 5.3, illustrates the proportional increase rate of the stator current unbalance as the healthy motor is loaded, but with an insignificant decrease after the 50% loading point. The efficiency of the motor can be altered by the unbalance of the stator quantities. However, current unbalance is common at low loads.

Therefore, current unbalance is considered as a general motor wellness index in the fault detection and classification scheme, which will be revised accordingly at the end of this chapter.

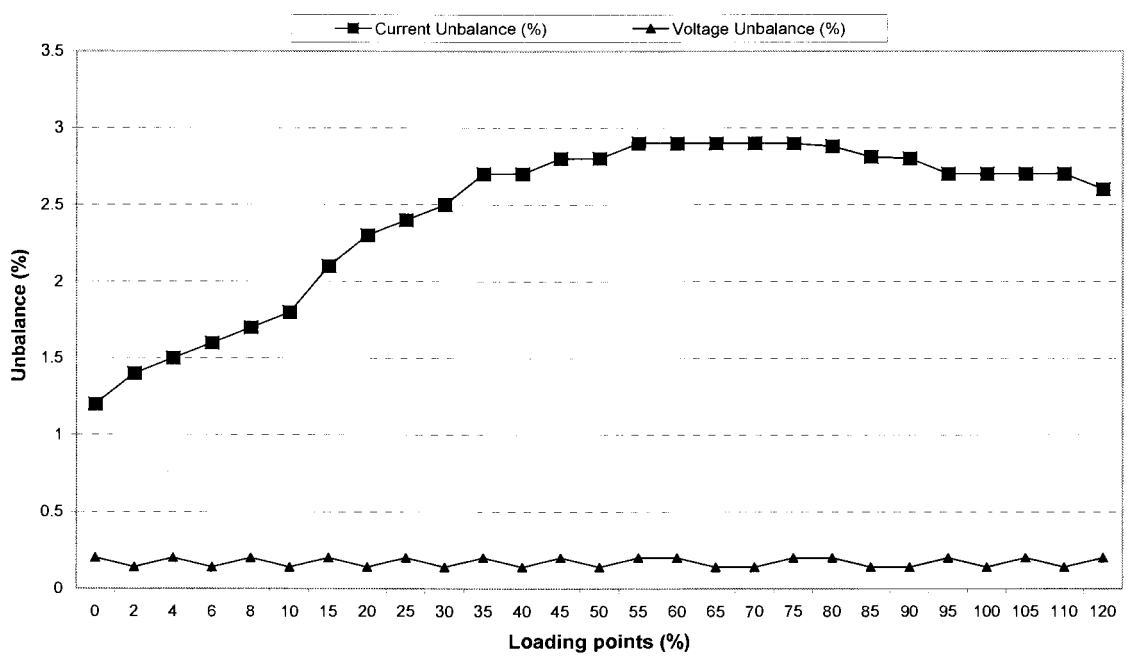

Fig. 5.3: Stator current and voltage unbalances from no-load to full load conditions

5.4. Supply voltage unbalance

The voltage unbalance is defined to be

$$V_{un} = \frac{V_{dev}}{V_{avg}} \times 100 \qquad (5.1)$$

where V_{un} is the percent of voltage unbalance, V_{dev} is the maximum voltage magnitude deviation from the average voltage magnitude V_{avg}.

As represented by Fig. 5.4, voltage unbalance reduces phase rotation uniformity and increases air-gap flux fluctuations that produce speed ripples that consequently increase the fault severity by producing more torque pulses. Moreover, rotor rotational speed is evidently reduced by forcing a high magnitude of voltage unbalance as in Fig. 5.5 that, practically and as per standards, should not be reached. However, the voltage unbalance has been exaggerated to illustrate its negative impact on fault detection and classification processes.

In the proposed system scheme, the magnitude of voltage unbalance needs to be monitored precisely. A failure of a broken rotor bar may misleadingly be reported due to the overwhelming effect of voltage unbalance in which rotor speed shifted to a lower level at the same loading point.

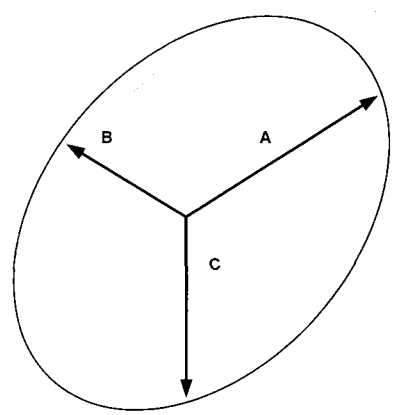

Fig. 5.4: Representation of rotating flux deformity due to voltage decrease at phase-b.

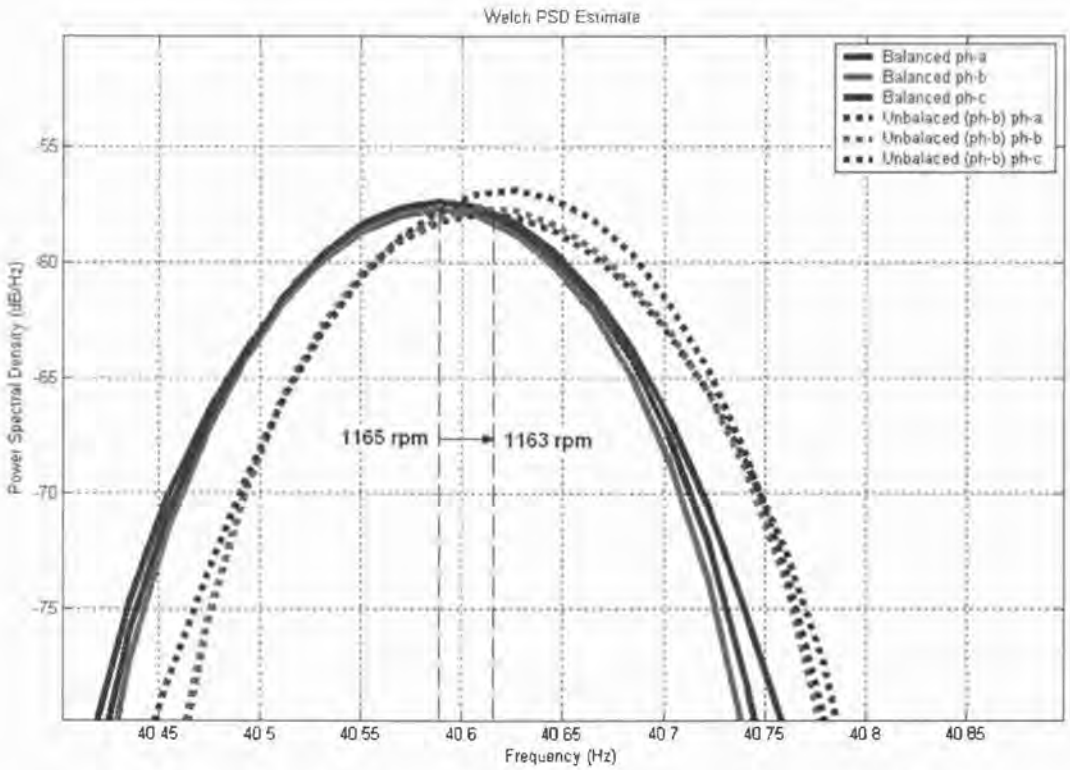

Fig. 5.5: Rotor speed reduction of 2 rpm due to 6% unbalance at phase-b

5.5. Core saturation

Some facts and effects of core saturation on the rotor fault monitoring process can be summarized as follows:

- Reduced saturation is attained by lowering stator terminal voltages.
- Magnitude of core saturation can be verified by monitoring the 3rd harmonic of stator current.
- Resulting motor torque is inversely proportional to stator voltage magnitude squared.
- As discussed in session 2.1.2, the upper broken bar sideband is a reaction of the speed ripples that are suppressed by high inertia values.

– As discussed in session 2.2.3, the core saturation effect on the permeance of the machine air-gap is obvious. The reduced terminal voltage can eliminate saturation effects from the monitored rotor fault signals.

These days, voltage level and many other electrical quantities are comprehensively monitored via advanced Intelligent Electronic Devices (IED's) mounted on motor control cabinets and/or linked to power monitoring centers. An instantaneous update of motor electrical quantities can be integrated with the fault detection and classification scheme, as shown in Fig. 5.6. The load oscillation separation algorithm will be discussed in the following chapter.

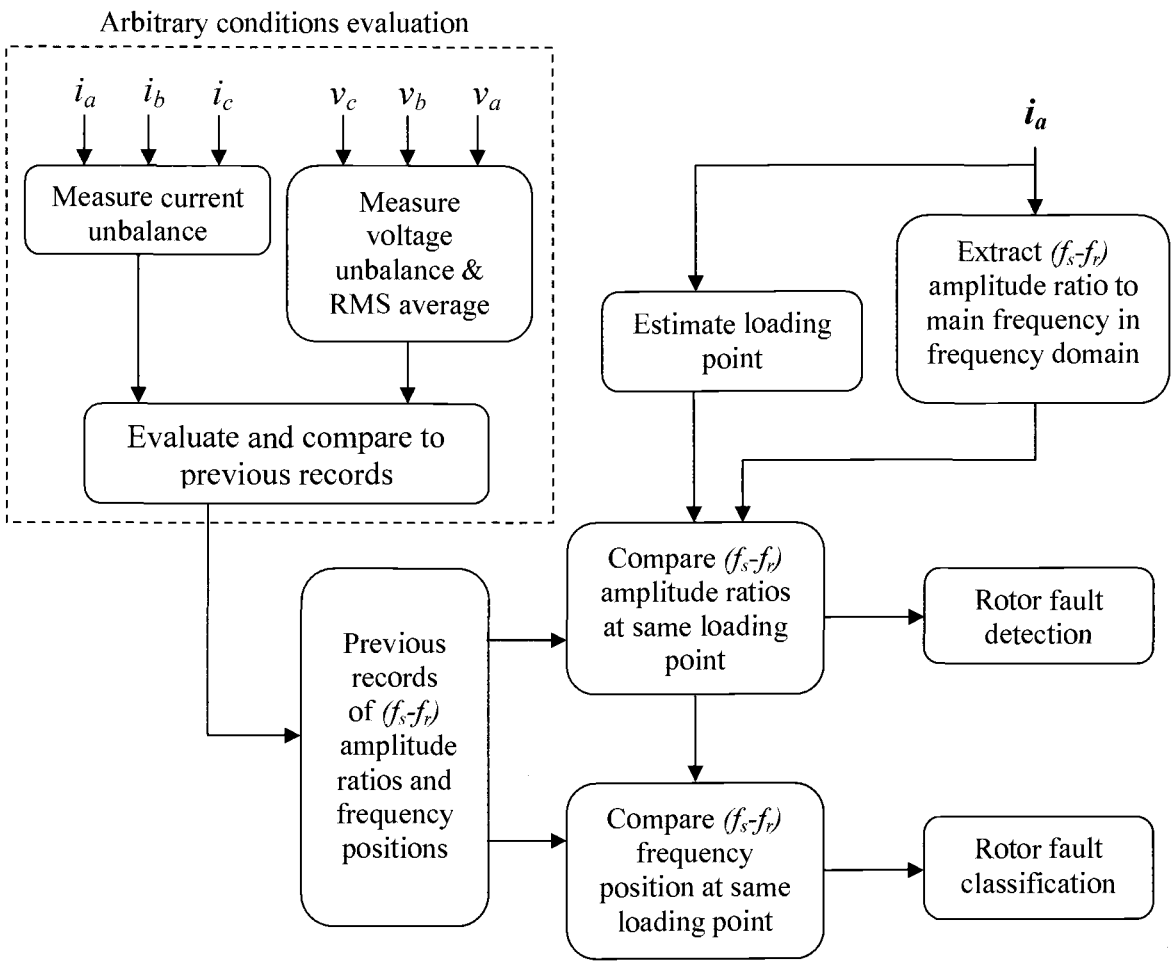

Fig. 5.6: Fault detection and classification scheme integrated with power monitoring system

6. Negative-Sequence Mean Value Approach For Separations of Rotor Faults

Many disadvantages are associated with the existing fault separation techniques, which include the instantaneous power spectral analysis method, Vienna monitoring method, and synchronous reference frame flux observer method. All suffer from some of the following limitations:

- Requirement of accurate estimation of machine parameters that incessantly vary due to temperature rise and skin effect.
- Integration errors and drifts in the synchronous reference frame flux observer.
- Effectiveness is governed by the technique application.

Therefore, due to the above shortcomings, those techniques do not accommodate the requirements of the envisioned motor diagnosis systems.

In practice, it is very difficult to separate the rotor fault induced positive and negative harmonics from load oscillation induced harmonics. Despite the fact that the supply arbitrary condition massively influences the negative-sequence components, the **negative-sequence separation technique method** has been elected to be the optimal severity indicator of any rotor fault. However, an evaluation of the supply arbitrary condition needs to be carefully incorporated into the fault separation process.

The proposed approach is a hybrid of a modified synchronous reference frame and negative-sequence computation routines [14]. As in Fig. 6.1, the system compares previous records of i_{qs}^{e+} and i_{ds}^{e-}, which are the positive-sequence of the stator current aligned with the *q-axis*, and the negative-sequence of the stator current aligned with the *d-axis* respectively. Any increase in the mean values of these quantities is considered a deviation from the normal condition of the motor. An increase in the tangential values (Δ_q^+) can be interpreted as a positive-sequence increase due to load oscillations (T_p^+),

while an increase in the radial values (Δ_d^-) can be interpreted as a negative-sequence increase due to a fault condition.

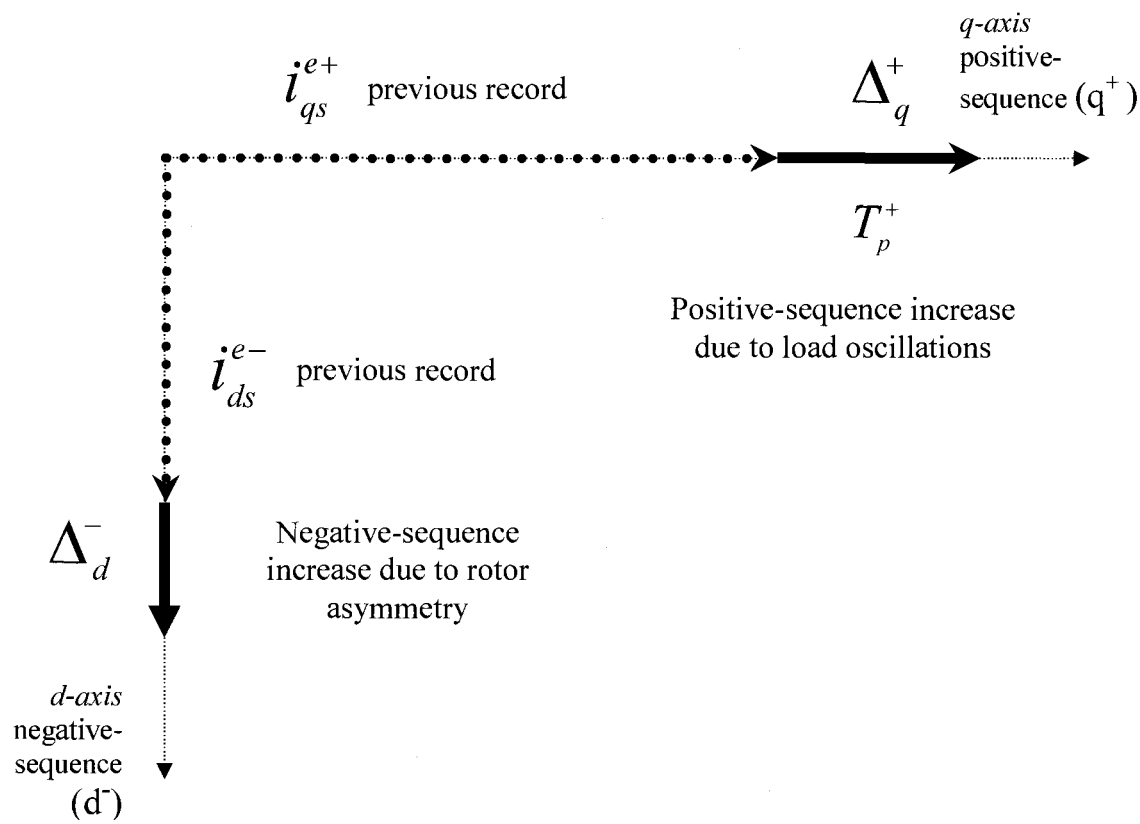

Fig. 6.1: Separation of rotor fault signals using negative-sequence mean value approach

The transformation process is accomplished by computing the synchronous *dq*-phasor currents and then the quantities of positive- and negative-sequence as shown in Fig. 6.2. The synchronous rotating currents have exactly the same magnitude in any synchronous reference frame. However, monitoring the DC quantities of i_{ds}^{e-} is conceptually regarded as a good fault indicator, while i_{qs}^{e+} can quantify the positive-sequence increment due to torque pulses from a coupled load.

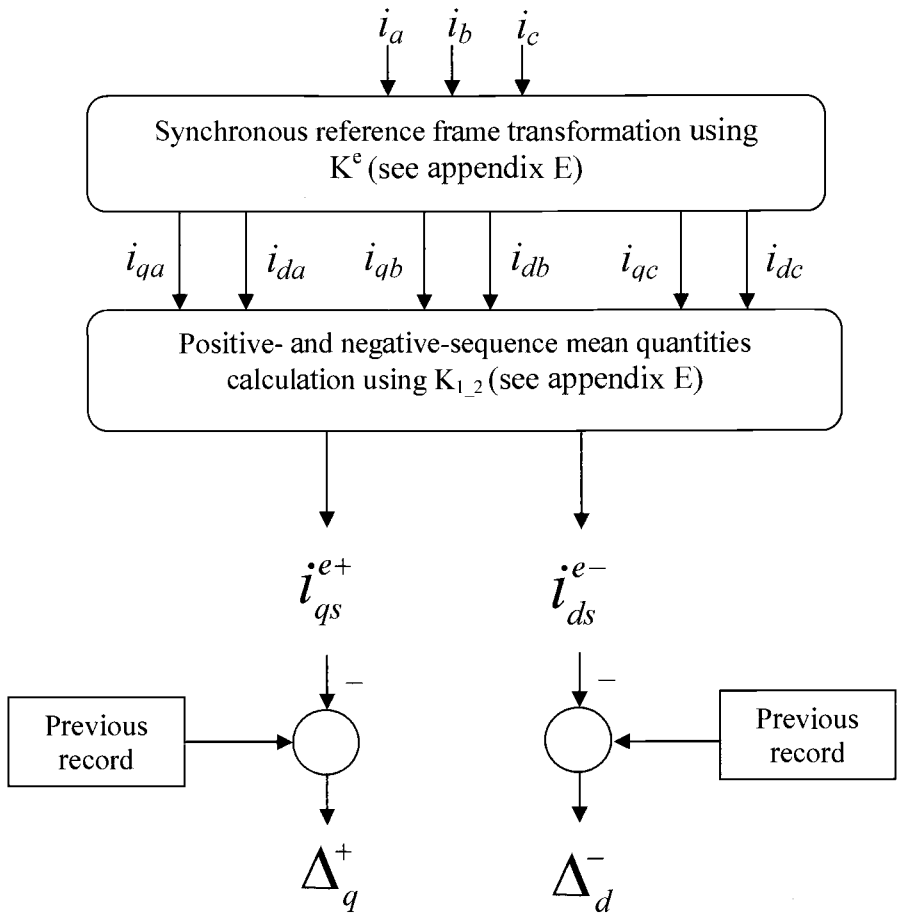

Fig 6.2: Block diagram of the rotor fault separation algorithm

Theoretically, Δ_d^- = 0 in the presence of only load torque pulses, while the value of Δ_q^+ is expected to be small in the presence of rotor faults due to the fact that some air-gap asymmetries induce low magnitude positive-sequence harmonics. However, in practice, the inherent dynamic eccentricity, machine or supply arbitrary variables, inject extra negative-sequence into a healthy machine making the value of Δ_d^- not an absolute zero even though the actual condition of the machine is undamaged.

The following conditions will be applied to the result in the verification test, as in Table 6.1:

- Rotor fault is highly likely to exist in the motor if Δ_d^- increased.
- Load oscillation is highly likely to exist in the motor if Δ_q^+ increased.

Table 6.1
Experimental verification of rotor fault separation algorithm using m1.m MATLAB script in appendix E.

Record	**Record length**	**Sampling Frequency**	Δ_d^-	Δ_q^+	**Motor diagnostics results**
RECORD 1	6 Cycles	250 kHz	**4.4e-4**	**1.6e-5**	Record 2 induced more i_{qs}^{e+} compared to record 3. (Record 2 is a load oscillation condition of $T_p^+ = 2$ N.m)
RECORD 2	6 Cycles	250 kHz			
RECORD 1	6 Cycles	250 kHz	**7.9e-4**	**6.3e-6**	Record 3 induced more i_{ds}^{e-} compared to record 2. (Record 3 is a dynamic eccentricity of radial vibration = 0.35 (IN/Sec)
RECORD 3	6 Cycles	250 kHz			

The deployed algorithm is greatly affected by the supply arbitrary conditions. During data capture, the magnitudes of current and voltage unbalances have been carefully maintained as constant. However, the results extracted are not always consistent and proved that the absolute routine reliability is never achieved due to these external factors.

The power spectrum density (PSD) estimation method has been integrated with the rotor fault separation algorithm, as listed in appendix E. Similar results have been attained, and with the same inconsistency rate, during some tests. An example of the separation of dynamic eccentricity fault is illustrated in Fig. 6.3, where the mean values of the normal and load torque pulse conditions are obviously equal at the DC component (0 Hz) of the PSD plot of the negative-sequence *d-axis* current compared to the dynamic eccentricity condition.

The efficiency of the proposed scheme has been explored through repeated simulations of different combinations of fault and load oscillation conditions. Although there is not full confidence in implementing this scheme, it offsets some limitations of other techniques.

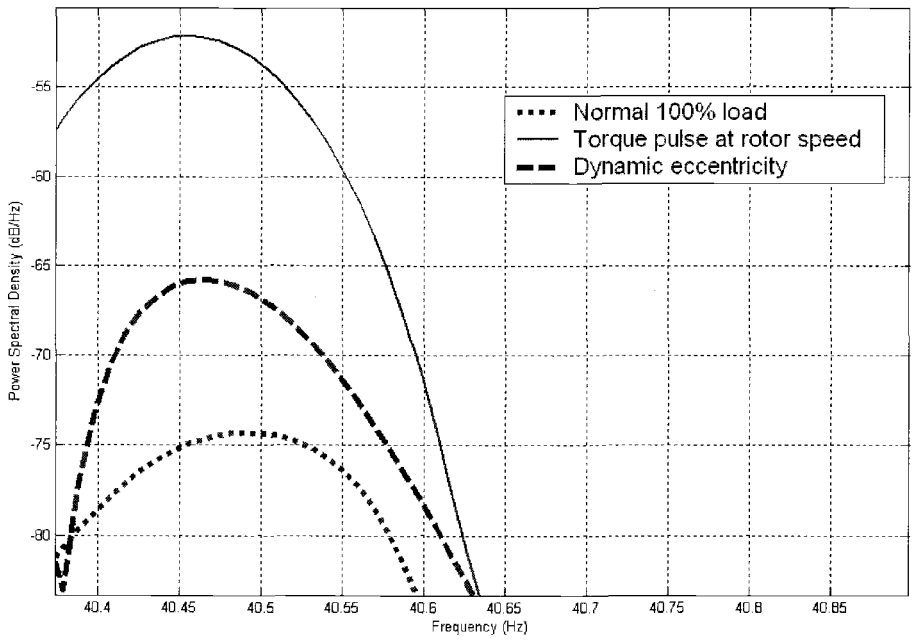

(c) Before filtration

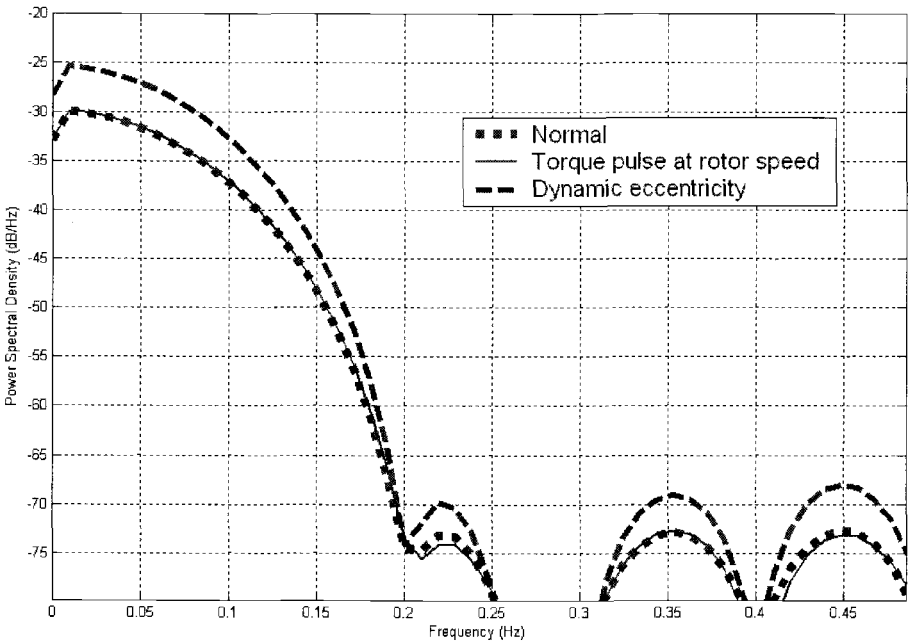

(d) After filtration

Fig. 6.3: Dynamic eccentricity fault separation

7. Implementation and Evaluation of On-line Motor Diagnosis System

The envisioned on-line motor diagnostic monitoring system has complementary benefits for preventative fault detection and identifies potential improvements to industrial plant operations. It has the advantages of detecting and filtering broken rotor bar faults and air-gap anomaly signals remotely and adaptively, allowing a dynamic response to various operating conditions where the monitored values of the fault frequencies are drastically changing as a function of slip frequency.

In critical process applications, the proposed system would provide the foundation for continually monitoring a machine in a noninvasive way, enhancing the ability of maintenance systems to identify impending motor failures and then driving maintenance schedules more efficiently. The diagnosis data can be made available over an open network to a conventional operator interface station. With the advent of this current signature analysis algorithm, many industries will be driven toward online, non-invasive diagnostic solutions.

The system consists of three-phase current and voltage transducers/sensors, and a micro-server to enable these sensors to interface to the Ethernet. The system uses standard PC hardware, where it communicates with, and logs the monitored data in, one computer (the target or communication server) and then performs data manipulation and computation process in another computer (host server).

Fig. 7.1 depicts the basic form of the envisioned on-line system. High accuracy and coordinated current and potential transformers must be selected. The servers communicate directly with those transducers and generate frequency spectra, although memory limitations might be of concern when dealing with many input channels from many different motors simultaneously. Proper communication time scheduling can be used to address memory limitation problems.

The on-line fault algorithms evaluate supply arbitrary conditions and separate fault signals from load oscillations. They compute raw current data of both high and low record lengths and deploy modern spectral estimation techniques. Sample collection times and memory requirements for high spectral resolution cause on-line monitoring bottlenecks. Therefore, balancing strategies need to be considered to reduce the

arithmetic computational load for each input sample, to increase algorithm operating speed, and to eliminate the effect of the spectral leakage phenomenon that alters the monitored amplitudes and introduces high noise levels. Monitoring these noise values can ease the task of determining rotor fault severity and classification processes.

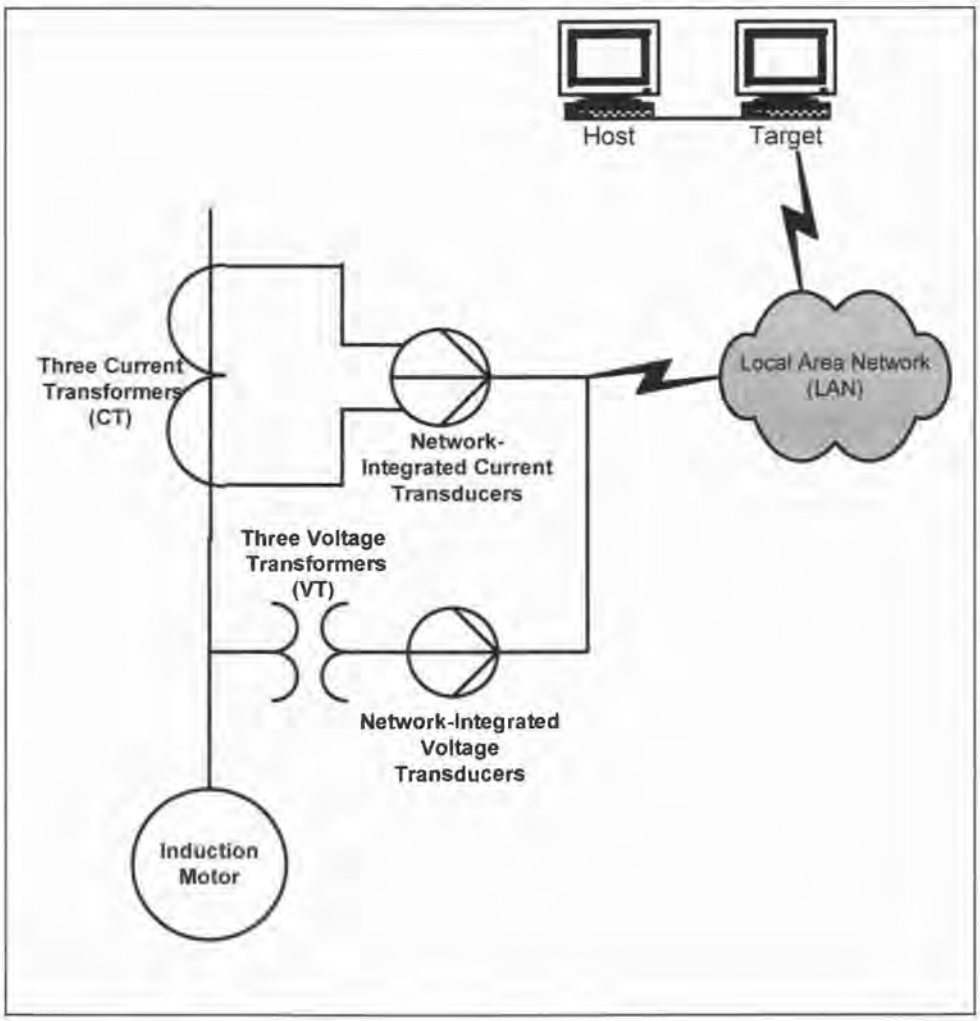

Fig. 7.1: Envisioned System

8. Results

8.1. Experimental equipment

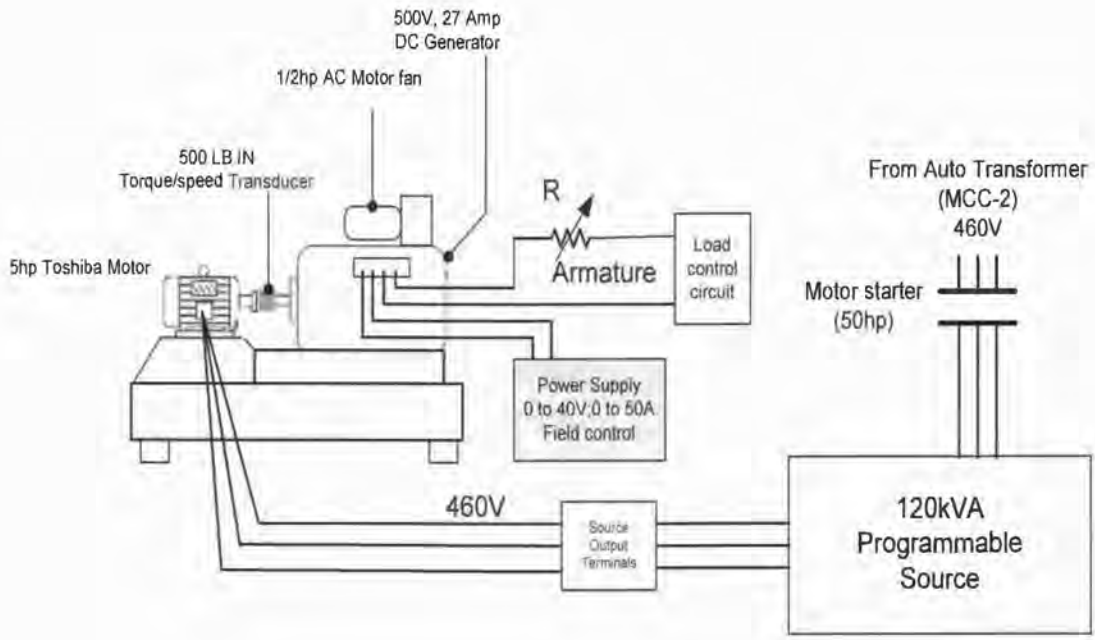

Fig.8.1: 15Hp Test rig with 5Hp Toshiba motors for mechanical fault simulations (broken rotor bars, dynamic eccentricities, and shaft misalignments)

Table 8.1
Experimental equipment specifications

Test equipment	Specifications
Reliance DC Motor/Generator	15Hp, 500V, 27Amps, Field voltage 150/300V, Field current 1.72/1.08A
Tektronix AWG 2005 Arbitrary waveform generator	120KVA programmable source, Max line voltages, 530Vrms steady-state, 600Vrms transient, Max phase voltage, 305Vrms steady-state, 350Vrms transient, Peak phase current, 166A, Frequency range, 45Hz to 2 kHz.
Tektronix TDS 5104 Digital Phosphor Oscilloscope	1 GHz, 500 MHz, 350 MHz Models, 5 GS/s max. Sample Rate, 100,000 wfms/s Waveform Capture Rate, 2 and 4 Channel Models, Up to 8 M Record Length, Floppy Disk Drive, Hard Drive, CD-ROM, USB & LAN
Power Measurement IED 7600	True RMS 3-phase voltage, current and power, Instantaneous 3-phase voltage, current, frequency, and power factor, Up to 256 samples per cycle, Harmonics: individual and total harmonic distortion up to the 63rd. Sag/Swell, Waveform recording, Transient detection, Symmetrical components
PM 5132 Function Generator	0.1 Hz to 2 MHz
MOSFET IRF 542	See table 2.5
Torque transducer Lebow model 7540	N.m measurements
DC supply	Voltage control of 0 to 40 V
Dell Computer	2GHz speed, 256MB

The low THD output of the MSRF programmable source enables reliable fault simulations and high accuracy measurements free of unexpected supply noises.

8.2. Resulting accuracy of rotor fault detection and classification

Many factors imposed significant impacts on the resulting accuracy of the rotor fault detection and classification task. Not only supply or load arbitrary conditions are expected to reduce the accuracy of the results, but also system hardware design, capacity and noise filtration, and immunity are all primary parameters.

The following discussion presents some examples and illustrations of the above factors in an attempt to help evaluate the robustness of the fault detection and classification system:

- The spectral estimation technique used, namely the power spectral density method or PSD function, determines the distribution of power with the frequency of a random input signal. Physically, the PSD process estimates the power distribution by passing the signal through a band pass filter that has a sufficiently narrow bandwidth, and then measuring the power at its output. The power is then divided by the filter bandwidth. The process presupposes that the signal will be of adequate length to allow the filter transients to decay – in this research a period of 10 seconds has been selected. However, the motor's dynamics are noticeably unstable and probably can influence the demodulation process that requires extensive monitoring of motor operating behavior during the stator current recording process.
- Voltage and current transducers accuracies need to be coordinated or "phantom" unbalance will appear.
- In the envisioned system design, the motor current quantities are sensed by advanced transducers where Analog-to-Digital (A/D) converters are used. The resolution of the A/D is not related to the resolution of the spectrum. The resolution of the A/D determines the dynamic range of the analyzer, which is the ability to resolve the lowest amplitude signals amongst high amplitude signals (classic A/D converters are 16 bits). On the other hand, the resolution of the spectrum is nothing but a design issue for the data collector which can be resolved with more memory.
- Worthless high spectrum resolution, albeit high A/D resolution, could happen; Low resolution monitor screen can limit the ability to zoom-in to frequency and/or amplitude details.

9. Conclusion and Recommendation for Future Work

This work has presented a method to estimate the rotor wellness condition of a squirrel-cage motor. The procedure for detecting the incipient rotor fault and air-gap asymmetry was based on results obtained from a comprehensive surveillance technique using current signature analysis. Further analysis of rotor fault separation is rooted in the well-known synchronous reference frame and symmetrical components analysis of electrical machinery. The combination of machine and supply measurements permits evaluation of the arbitrary system conditions. If precisely evaluated, the system noise immunity is elevated and the fault threshold can be sited correctly.

Future work involves integrating the fault detection and classification system with the power monitoring system that is a critical issue for system reliability management. Also, communication mitigation strategies have to be extensively applied to adhere to the standards of substation automation. Recent microprocessor technologies can develop a high system capacity since a large portion of system resources are used for computation.

The ultimate goal of this work was to implement a centralized motor diagnostic monitoring system for mainly high motor-to-load inertia applications. Of course, a cost-effective system mainly considers the monitoring of large-size machines. This assertion implies that there will be a clear line between fault severity and arbitrary load condition and, with large-machine systems, the source of error is greatly reduced.

The current intention is to include starting current signatures as a tool to allow condition monitoring independent of the loading point of the machine. This monitoring method is also easily adaptable when IM's have to perform many startups during a hard duty cycle, which is the most exacting and critical condition for bar breakage.

References

[1] S. Crus and A. Cardoso, "Rotor cage fault diagnosis in three-phase induction motors by the total instantaneous power spectral analysis," *1999. Thirty-Fourth IAS Annual Meeting.* Conference Record of the *1999 IEEE Industry Applications* Conference, vol. 3, pp. 1928-1934, 1999.

[2] C. Kral, F. Pirker, and *G.* Paswli, "Influence of load torque on rotor asymmetry effects in squirrel cage induction machines including detection by means of the Vienna monitoring method," *Conference Proceedings EPE*, 2001.

[3] R. R Schoen and T. G. Habetler, "Evaluation and implementation of a system to eliminate arbitrary load effects in current-based monitoring of induction machines", *IEEE Transactions on Industry Applications,* v 33, n 6, Nov-Dec, 1997, p 1571-1577.

[4] Long Wu, Habetler and Harley, "Separating load torque oscillation and rotor fault effects in stator current-based motor condition monitoring", *School of Electrical and Computer Engineering, Georgia Institute of Technology, Grainger Seminar,* Nov 8th, 2004.

[5] M. Hajiaghajani, "Modeling, detection and classification of eccentricity and broken bar fault in electrical machines," Ph.D. dissertation, Dep. Elect. Eng., Texas A&M Univ., Texas, May 2003.

[6] F. Filippetti, G. Franceschini, C Tossoni and P. Vas, "AI Techniques in induction machines diagnosis including the speed ripple effects," *IEEE Trans. Ind. Applications,* vol. 34, pp. 98–108, Jan/Feb. 1998.

[7] W. Thomson and R. Gilmore, "Current signature analysis to detect faults in induction motor drives-fundamentals, data interpretation, and industrial case histories" Proceedings of the 32nd Turbomachinery symposium, 2003.

[8] B. G. Gaydon, "An instrument to detect induction motor rotor circuit defects by speed fluctuation measurements," *IEE Conference Publication*, n 174, 1979, p 5-8.

[9] E. Wiedenbrüg, "Measurement analysis and efficiency of three-phase induction machines using instantaneous electrical quantities," Ph.D. dissertation, Dep. Elect. Eng. and Comp. Science, Oregon State Univ., Corvallis, Sep. 1998.

[10] D. Dorrell, W. Thomson and S. Roach, "Analysis of air-gap flux, current, and vibration signals as a function of the combination of static and dynamic air-gap eccentricity in 3-phase induction motors," *IEEE Trans. Ind. Applications,* vol. 33, pp. 24–34, Jan/Feb. 1997.

[11] D. Dorrell and A. Smith, "Calculation of U.M.P. in induction motors with series or parallel winding connections," *IEEE Trans. On Energy Conversion, vol. 9, n 2, pp. 304-310, Jane 1994.*

[12] S. J. Yang, Low-noise Electrical Motors (Oxford: Clarendon Press, 1981), 15-16.

[13] D. Dorrell, "Calculation of unbalanced magnetic pull in small cage induction motors with skewed rotors and dynamic rotors eccentricity," *IEEE Trans. On Energy Conversion, vol. 11, n 3, pp. 483-488, Sep. 1996.*

[14] C. Hochgraf and R. Lasseter, " StatCom Controls for Operation with Unbalanced Voltages," *Power systems Engineering Research Center,* IEEE publications, 1997.

[15] G. B. Kliman, J. Stein, and R. D. Endicott, "Noninvasive detection of broken rotor bars in operating induction motors," *IEEE Trans. Energy Conversion,* vol. 3, pp. 873–879, Dec. 1988.

[16] F. Filippetti, G. Franceschini, and C. Tassoni, "Neural networks aided on-line diagnostics of induction motor rotor faults," *IEEE Trans. Ind. Applicat.,* vol. 31, pp. 892–899, July/Aug. 1995.

[17] R. R. Schoen, B. K. Lin, T. G. Habetler, J. H. Schlag, and S. Farag, "An unsupervised, on-line system for induction motor fault detection using stator current monitoring," *IEEE Trans. Ind. Applicat.,* vol. 31, pp. 1280–1286, Nov./Dec. 1995.

[18] R. R. Schoen and T. G. Habetler, "Effects of time-varying loads on rotor fault detection in induction machines," *IEEE Trans. Ind. Applicat.,* vol. 31, pp. 900–906, July/Aug. 1995.

[19] R. R. Schoen, "On-line current-based condition monitoring of three-phase induction machines," Ph.D. dissertation, Dep. Elect. Eng., Georgia Inst. Technol., Atlanta, Sept. 1994.

[20] B. D. Durocher and G. R. Feldmeier, "Preventive versus predictive maintenance," *IEEE Trans. Ind. Applicat. magazine,* Sept/Oct. 2004.

[21] F. Filippetti, G. Franceschini, C Tossoni and G. Kliman and A. Bellini, "Quantitative evaluation of induction motor broken bars by means of electrical signature analysis," *IEEE Trans. Ind. Applicat.,* vol. 37, pp. 1248–1255, Sep/Oct. 2001.

[22] B. Mirafzal and N. A. Demerdash, "Effects of load on diagnosing broken rotor bar faults in induction motors using the pendulous oscillation of the rotor magnetic field orientation," *IEEE Conf. Ind. Applicat.,* Oct. 2004.

[23] X. Boquiang, L. Heming and S. Liling, "Sensitive and reliable detection of broken rotor bar fault in induction motors," *IEEE Conf. Ind. Applicat.,* Oct. 2004.

[24] M. Obaid, "Detection of rotating mechanical asymmetries in small induction machines," Ph.D. dissertation, Dep. Elect. Eng., Georgia Inst. Technol., Atlanta, May 2003.

[25] M El Benbouzid and G. B. Kliman, "What stator current processing-based technique to use for induction motor rotor faults diagnosis?" *IEEE Trans. Energy Conv.*, ., vol. 18, pp. 238–244, Jan. 2003.

Appendix A: Test motor per-phase equivalent circuit

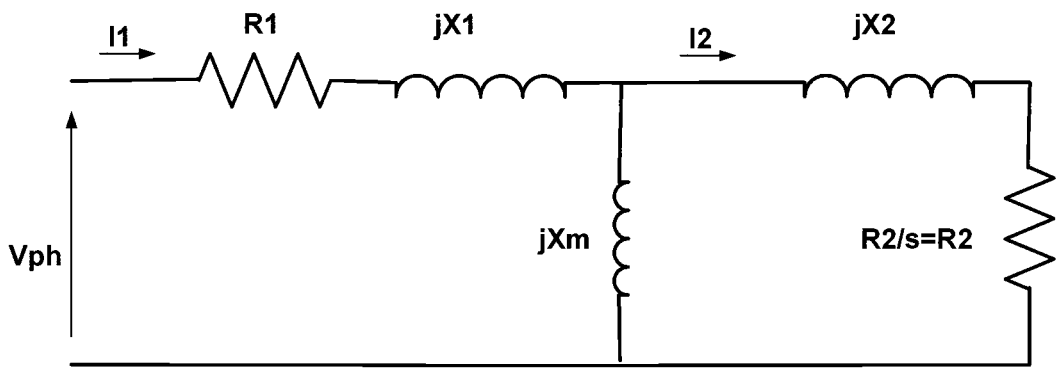

Test motor per-phase equivalent circuit (5Hp, Toshiba)

Measured Parameters	No-load Test	Locked- Rotor Test	DC Test
Frequency (f)	60Hz	60Hz	
Supply Voltage (V_L)	460V	88.3V	13.3 Vdc
Phase Current (I_1)	3.1A	6.5A	6.5 Adc
Input Power (P_{in})	430W	411W @PF=0.413	

Form the no-load test:

$$Z_{nl} = \frac{V_L}{\sqrt{3} I_1} = X_1 + X_m \qquad (A1)$$

$$Z_{nl} = \frac{460}{\sqrt{3} \times 3.1} = 85.67\Omega$$

From motor data sheet:

$$X_1 = 0.0814 \times \left[X_{stator\ slot} + X_{coil\ end} + 0.5 \times \left(X_{zig\ zag} + X_{belt\ leakage} \right) \right]$$

$$X_1 = 2.82\Omega at\, 60\,Hz,\ L_1 = 7.49mH$$

$$X_2 = 0.0814 \times \left[X_{rotor\ slot} + 0.5 \times \left(X_{zig\ zag} + X_{belt\ leakage} \right) \right]$$

$$X_2 = 5.15\Omega at\, 60\,Hz,\ L_2 = 13.66mH$$

From (A1):

$$X_m = 82.85\Omega,\ M = 219mH$$

From the locked-rotor test:

$$Z_{LR} = \frac{V_L}{\sqrt{3}I_1} = \frac{88.3}{\sqrt{3}\times 6.5} = 7.84\Omega$$

$$R_{LR} = \frac{P_{LR}}{3I_1^2} = \frac{411}{3\times(6.5)^2} = 3.24\Omega = R_1 + R_2 \qquad (A2)$$

From the DC test:

$$R_1 = \frac{V}{2I} = \frac{13.3}{2\times 6.5} = 1.023\Omega$$

Substituting in (A2):

$$R_2 = 2.217\Omega$$

Toshiba motors data:

Rated (V)	Rated HP	RPM	DE Bearing	ODE Bearing	Frame	Full Load RPM	Idle (A)
460	5	1200	6308C3	6308C3	215T	1165	3.1
FLC (A)	**LRC (A)**	**FLT (lbft)**	**LRT (%)**	**BDT (%)**	**Eff'y @ 1.0 (%)**	**Eff'y @ 0.75 (%)**	**Eff'y @ 0.5 (%)**
6.5	46.0	22.5	279	376	90.1	89.7	87.4
P.F. @ 1.0 (%)	**P.F. @ 0.75 (%)**	**P.F. @ 0.5 (%)**	**Max KVAR**	**Sound levels**	**FL Watts Loss**	**Rotor Inertia (lbft2)**	**Type of Conn.**
79.4	72.7	60.6	2.2	49	410	0.956	Y
Reactance coefficient	**Stator Slot**	**Rotor Slot**	**Zigzag**	**Coil End**	**Belt Leakage**	**Total resistance**	**Total Reactance**
0.0814	15.83	49.666	22.357	5.223	4.952	2.961	8.873

Appendix B: Dynamic eccentricity calculation

Dynamic eccentricity can be calculated from the relative geometry of the rotor. Air-gap deficiency from the standard nominal air-gap is considered.

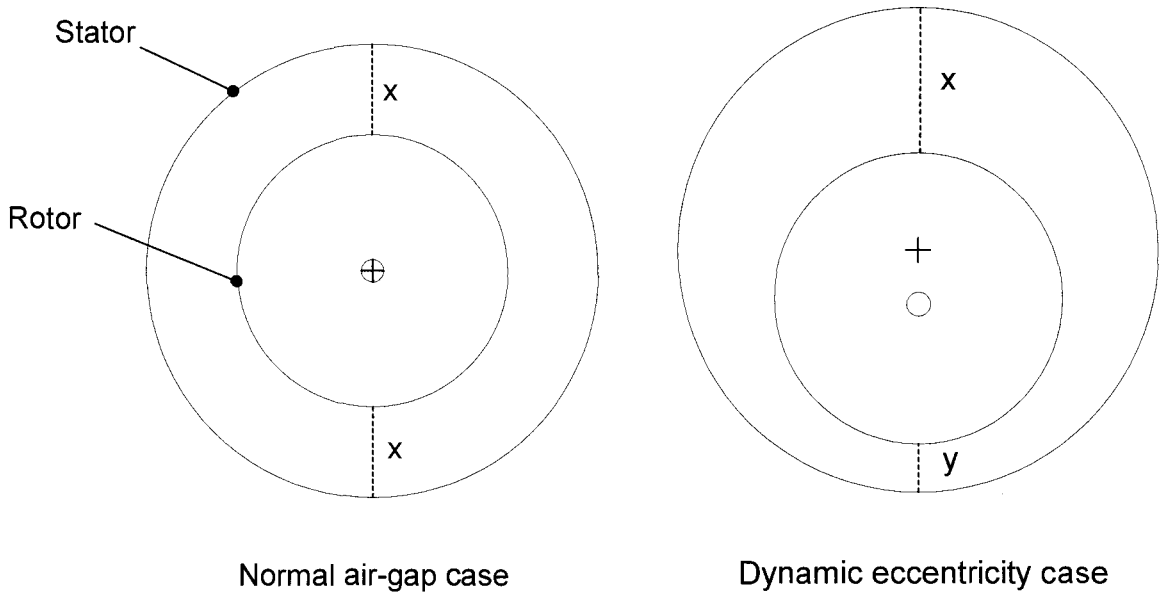

○ rotor symmetry axis + rotor rotational axis

From the normal air-gap case, normal air-gap = x.

From the dynamic eccentricity case, the dynamic eccentricity percentage can be calculated as follows:

$$\%DE = \frac{\frac{x+y}{2} - x}{\frac{x+y}{2}} \times 100$$

Appendix C: MATLAB® script of Clark, negative and positive sequence transformations

```
% motor performance parameter: hp=5; volts=460; rpm=1200; P=6; Is=6.5;

%initialize vectors:
idq=[0;0;0];
idq2=[0;0;0];
idq1=[0;0;0];

%Input tabulated current data:
%The data are stored into a file, which is read by MATLAB


input_current_data_phase-a;
ia=input_current_data_phase-a;

input_current_data_phase-b;
ib=input_current_data_phase-b;

input_current_data_phase-c;
ic=input_current_data_phase-c;

% Applying Clark Transformation to input currents:

Kabc_dq=(2/3)*[1          -0.5          -0.5;
               0           sqrt(3)/2    -sqrt(3)/2;
               sqrt(1/2)   sqrt(1/2)     sqrt(1/2)];

% Applying positive-sequence Transformation to input currents:

a=exp(j*2*pi/3);

Kabc_abc1=(1/3)*[1        a        a^2;
                 a^2      1         a;
                 a        a^2       1];

% Applying negative-sequence Transformation to input currents:

Kabc_abc2=(1/3)*[1        a^2       a;
                 a        1        a^2;
                 a^2      a         1];

% Data length:
m=100000;
for t=1:1:m
```

```
ihelp_abc= [ia(t);
            ib(t);
            ic(t)];
 helpdq = Kabc_dq*ihelp_abc;
 idq=[idq helpdq];
 ids=idq(1,:);          % d-axis current
 iqs=idq(2,:);          % q-axis current
end

for t=1:1:m
ihelp_abc= [ia(t);
            ib(t);
            ic(t)];

 helpdq = Kabc_dq*ihelp_abc;
 helpdq1 = Kabc_abc1*helpdq;
 helpdq2 = Kabc_abc2*helpdq;
 idq1=[idq1 helpdq1];
 idq2=[idq2 helpdq2];

 ids1=idq1(1,:);          % positive-sequence of d-axis current
 iqs1=idq1(2,:);          % positive -sequence of q-axis current

 ids2=idq2(1,:);          % negative-sequence of d-axis current
 iqs2=idq2(2,:);          % negative-sequence of q-axis current
end

% Power spectrum density plots (see appendix C):

fs= 10000;                % Sampling frequency

x=ia(1:m);
window1=hamming(m);
noverlap1=m/2;
pwelch(x,window1,noverlap1,2^20,fs);
hold on

x=ids(1:m);
window1=hamming(m);
noverlap1=m/2;
pwelch(x,window1,noverlap1,2^20,fs);

x=iqs(1:m);
window1=hamming(m);
noverlap1=m/2;
pwelch(x,window1,noverlap1,2^20,fs);
```

```
x=ids1(1:m);
window1=hamming(m);
noverlap1=m/2;
pwelch(x,window1,noverlap1,2^20,fs);

x=ids2(1:m);
window1=hamming(m);
noverlap1=m/2;
pwelch(x,window1,noverlap1,2^20,fs);

x=iqs1(1:m);
window1=hamming(m);
noverlap1=m/2;
pwelch(x,window1,noverlap1,2^20,fs);

x=iqs2(1:m);
window1=hamming(m);
noverlap1=m/2;
pwelch(x,window1,noverlap1,2^20,fs);

hold off

title('Clark d-q, positive- and negative-sequence transformations')
```

Appendix D: MATLAB® script of spectral estimation applying Welch method and Hamming window

Power Spectrum Density (PSD) MATLAB® script example:

```
fs= 5000;                    %sampling frequency
m=50000;                     %Window length
data_file;
x=data_file(1:m);            %The data are stored into a file, which is read by
MATLAB
window=hamming(m);
noverlap=m/2;
pwelch(x,window,noverlap,[],fs);
```

Reference pwelch.mat file code:

```
function varargout = pwelch(x,win,noverlap,varargin)
%PWELCH Power Spectral Density estimate via Welch's method.
%   Pxx = PWELCH(X) returns the Power Spectral Density (PSD) estimate,
%   Pxx, of a discrete-time signal vector X using Welch's averaged,
%   modified periodogram method.  By default, X is divided into eight
%   sections with 50% overlap, each section is windowed with a Hamming
%   window and eight modified periodograms are computed and averaged.
%
%   If the length of X is such that it cannot be divided exactly into
%   eight sections with 50% overlap, X will be truncated accordingly.
%
%   Pxx is the distribution of power per unit frequency. For real signals,
%   PWELCH returns the one-sided PSD by default; for complex signals, it
%   returns the two-sided PSD.  Note that a one-sided PSD contains the
%   total power of the input signal.
%
%   Pxx = PWELCH(X,WINDOW), when WINDOW is a vector, divides X into
%   overlapping sections of length equal to the length of WINDOW, and then
%   windows each section with the vector specified in WINDOW.  If WINDOW is
%   an integer, X is divided into sections of length equal to that integer
%   value, and a Hamming window of equal length is used.  If the length of
%   X is such that it cannot be divided exactly into integer number of
%   sections with 50% overlap, X will be truncated accordingly.  If WINDOW
```

```
%   is omitted or specified as empty, a default window is used to obtain
%   eight sections of X.
%   Pxx = PWELCH(X,WINDOW,NOVERLAP) uses NOVERLAP samples of overlap from
%   section to section.  NOVERLAP must be an integer smaller than the WINDOW
%   if WINDOW is an integer.  NOVERLAP must be an integer smaller than the
%   length of WINDOW if WINDOW is a vector.  If NOVERLAP is omitted or
%   specified as empty, the default value is used to obtain a 50% overlap.
%
%   [Pxx,W] = PWELCH(X,WINDOW,NOVERLAP,NFFT) specifies the number of FFT
%   points used to calculate the PSD estimate.  For real X, Pxx has length
%   (NFFT/2+1) if NFFT is even, and (NFFT+1)/2 if NFFT is odd.  For complex
%   X, Pxx always has length NFFT.  If NFFT is specified as empty, the
%   default NFFT -the maximum of 256 or the next power of two
%   greater than the length of each section of X- is used.
%
%   W is the vector of normalized frequencies at which the PSD is
%   estimated.  W has units of rad/sample.  For real signals, W spans the
%   interval [0,Pi] when NFFT is even and [0,Pi) when NFFT is odd.  For
%   complex signals, W always spans the interval [0,2*Pi).
%
%   [Pxx,F] = PWELCH(X,WINDOW,NOVERLAP,NFFT,Fs) returns a PSD computed as
%   a function of physical frequency (Hz).  Fs is the sampling frequency
%   specified in Hz.  If Fs is empty, it defaults to 1 Hz.
%
%   F is the vector of frequencies at which the PSD is estimated and has
%   units of Hz.  For real signals, F spans the interval [0,Fs/2] when NFFT
%   is even and [0,Fs/2) when NFFT is odd.  For complex signals, F always
%   spans the interval [0,Fs).
%
%   [...] = PWELCH(...,'twosided') returns a two-sided PSD of a real signal
%   X. In this case, Pxx will have length NFFT and will be computed  over
%   the interval [0,2*Pi) if Fs is not specified and over the interval
%   [0,Fs) if Fs is specified.  Alternatively, the string 'twosided' can be
%   replaced with the string 'onesided' for a real signal X.  This would
%   result in the default behavior.  The string 'twosided' or 'onesided'
%   may be placed in any position in the input argument list after NOVERLAP.
%
%   PWELCH(...) with no output arguments by default plots the PSD
%   estimate in dB per unit frequency in the current figure window.
%
%   EXAMPLE:
%     Fs = 1000;   t = 0:1/Fs:.296;
%     x = cos(2*pi*t*200)+randn(size(t));  % A cosine of 200Hz plus noise
%     pwelch(x,[],[],[],Fs,'twosided'); % Uses default window, overlap & NFFT.
%
%   See also PERIODOGRAM, PCOV, PMCOV, PBURG, PYULEAR, PEIG, PMTM, PMUSIC
%   and PSDPLOT.

%   Author(s): R. Losada
%   Copyright 1988-2002 The MathWorks, Inc.
%   $Revision: 1.28 $  $Date: 2002/03/28 17:30:19 $
```

```
%  References:
%    [1] Petre Stoica and Randolph Moses, Introduction To Spectral
%        Analysis, Prentice-Hall, 1997, pg. 15
%    [2] Monson Hayes, Statistical Digital Signal Processing and
%        Modeling, John Wiley & Sons, 1996.

error(nargchk(1,6,nargin));
error(nargoutchk(0,2,nargout));

x = x(:);
isreal_x = isreal(x);
M = length(x);

if nargin < 3,
  noverlap = [];
  if nargin < 2,
    win = [];
  end
end

% Obtain the necessary information to segment X
[L,noverlap,win,msg] = segment_info(M,win,noverlap);
error(msg);

% Parse optional args nfft, fs
[options,msg] = pwelch_options(isreal_x,L,varargin{:});

% Compute the number of segments
k = (M-noverlap)./(L-noverlap);

% Uncomment the following line to produce a warning each time the data
% segmentation does not produce an integer number of segements.
%if fix(k) ~= k),
%  warning('The number of segments is not an integer, truncating data.');
%end

k = fix(k);

% Compute the periodogram power spectrum of each segment and average
% always compute the twosided power spectrum, we force Fs = 1 to get
% a spectrum not a spectral density
Sxx = zeros(options.nfft,1); % Initialize
xindx = 1;
for i = 1:k,
  Sxx = Sxx + periodogram(x(xindx:xindx+L-1),win,options.nfft,1,'twosided');
  xindx = xindx + L - noverlap;
end
Sxx = Sxx./k; % Average the sum of the periodograms

% Generate the frequency vector in [rad/sample] at which Sxx was computed
% If Fs is not empty, w will be converted to Hz in computepsd below
```

```
w = 2.*pi.*(0:options.nfft-1)./options.nfft;

% Compute the one-sided or two-sided PSD [Power/freq].
% Also compute the corresponding one-sided or two-sided power spectrum [Power],
% the frequency at which the psd is computed and the corresponding frequency units
[Pxx,Sxx,w,units] = computepsd(Sxx,w,options.range,options.nfft,options.Fs);

if nargout==0, % Plot when no output arguments are specified
  yscale = 'db';
  titlestring = 'Welch PSD Estimate';
  psdplot(Pxx,w,units,yscale,titlestring);
elseif nargout == 1,
  varargout = {Pxx};
elseif nargout == 2,
        varargout = {Pxx,w};
end
%-------------------------------------------------------------------------------------
function [L,noverlap,win,msg] = segment_info(M,win,noverlap)
%SEGMENT_INFO  Determine the information necessary to segment the input data.
%
%  Inputs:
%    M       - An integer containing the length of the data to be segmented
%    WIN     - A scalar or vector containing the length of the window or the window
respectively
%              (Note that the length of the window determines the length of the segments)
%    NOVERLAP - An integer containing the number of samples to overlap (may be empty)
%
%  Outputs:
%    L       - An integer containing the length of the segments
%    NOVERLAP - An integer containing the number of samples to overlap
%    WIN     - A vector containing the window to be applied to each section
%    MSG     - A string containing possible error messages
%
%
%  The key to this function is the following equation:
%
%    K = (M-NOVERLAP)/(L-NOVERLAP)
%
%  where
%
%    K       - Number of segments
%    M       - Length of the input data X
%    NOVERLAP - Desired overlap
%    L       - Length of the segments
%
%  The segmentation of X is based on the fact that we always know M and two of the set
%  {K,NOVERLAP,L}, hence determining the unknown quantity is trivial from the above
%  formula.

% Initialize outputs
L = [];
```

```
msg = '';

% Check that noverlap is a scalar
if any(size(noverlap) > 1),
  msg = 'You must specify an integer number of samples to overlap.';
  return
end

if isempty(win),
  % Use 8 sections, determine their length
  if isempty(noverlap),
    % Use 50% overlap
    L = fix(M./4.5);
    noverlap = fix(0.5.*L);
  else
    L = fix((M+7.*noverlap)./8);
  end
  % Use a default window
  win = hamming(L);
else
  % Determine the window and its length (equal to the length of the segments)
  if ~any(size(win) <= 1) | ischar(win),
    msg = 'The WINDOW argument must be a vector or a scalar.';
    return
  elseif length(win) > 1,
    % WIN is a vector
    L = length(win);
  elseif length(win) == 1,
    L = win;
    win = hamming(win);
  end
  if isempty(noverlap),
    % Use 50% overlap
    noverlap = fix(0.5.*L);
  end
end

% Do some argument validation
if L > M,
  msg = 'The length of the segments cannot be greater than the length of the input signal.';
  return
end

if noverlap >= L,
  msg = 'The number of samples to overlap must be less than the length of the segments.';
  return
end

%-----------------------------------------------------------------------
function [options,msg] = pwelch_options(isreal_x,N,varargin)
%PWELCH_OPTIONS   Parse the optional inputs to the PWELCH function.
```

```
%   PWELCH_OPTIONS returns a structure, OPTIONS, with following fields:
%   options.nfft        - number of freq. points at which the psd is estimated
%   options.Fs          - sampling freq. if any
%   options.range        - 'onesided' or 'twosided' psd

% Generate defaults
options.nfft = max(256,2^nextpow2(N));
options.Fs = []; % Work in rad/sample
if isreal_x,
  options.range = 'onesided';
else
  options.range = 'twosided';
end
msg = '';
[options,msg] = psdoptions(isreal_x,options,varargin{:});
% [EOF] pwelch.m
```

Appendix E: MATLAB® scripts of Rotor Fault Separation

The m1.m file computes the mean values of the positive- and negative-sequences of stator currents after aligning with a rotating synchronous reference frame.

```
% motor performance parameter: hp=5; volts=460; rpm=1200; P=6; Is=6.5;
% intialize
time=[0];
helpdqm=[0;0;0;0;0;0];
helpdqtpdem=[0;0;0;0;0;0];
%Input healthy motor tabulated current data:
%The data are stored into a file, which is read by MATLAB

input_current_data_phase-a;
ia=input_current_data_phase-a;

input_current_data_phase-b;
ib=input_current_data_phase-b;

input_current_data_phase-c;
ic=input_current_data_phase-c;

%Input faulty motor tabulated current data:
%The data are stored into a file, which is read by MATLAB

input_current_data_phase-af;
iaf=input_current_data_phase-af;

input_current_data_phase-bf;
ibf=input_current_data_phase-bf;

input_current_data_phase-cf;
icf=input_current_data_phase-cf;
```

```
% Positive- and negative-sequence currents transformation:
    K1_2 =[ 1/3     0      -1/6          sqrt(3)/6     -1/6          -sqrt(3)/6;
            1/3     0      -sqrt(3)/6    -1/6          sqrt(3)/6     -1/6;
            1/3     0      -1/6          -sqrt(3)/6    -1/6          sqrt(3)/6;
            1/3     0      sqrt(3)/6     -1/6          -sqrt(3)/6    -1/6;
            1/3     0      1/3           0             1/3           0;
            0       1/3    0             1/3           0             1/3];

m=RL;          % Record length
for t=1:1:RL
step=1/RL;     % Step size
time = [time (t)*step];
fe=60;
thetaf = 2*pi*fe*time;
costhetaf =cos(thetaf(t));
sinthetaf =sin(thetaf(t));
Ke =[ 2*costhetaf      0                    0;
            -2*sinthetaf      0                    0;
            0             2*costhetaf          0;
            0             -2*sinthetaf         0;
            0             0            2*costhetaf;
            0             0            -2*sinthetaf];
ihelp_abc= [ia(t);
            ib(t);
            ic(t)];
  helpdq  = Ke*ihelp_abc;
  helpdqm=[helpdqm helpdq];

end
  iqa=mean(helpdqm(1,:));
  ida=mean(helpdqm(2,:));
```

```
iqb=mean(helpdqm(3,:));
idb=mean(helpdqm(4,:));
iqc=mean(helpdqm(5,:));
idc=mean(helpdqm(6,:));
  helpdqf=[iqa;
       ida;
       iqb;
       idb;
       iqc;
       idc];
helpdq2f = K1_2*helpdqf;
 ids2fq=helpdq2f(1,:);
Normal_Q_axis_positive_sequence=ids2fq;
ids2fd=helpdq2f(2,:);
Normal_D_axis_positive_sequence=ids2fd;
 ids2fq=helpdq2f(3,:);
Normal_Q_axis_negative_sequence=ids2fq;
ids2fd=helpdq2f(4,:);
Normal_D_axis_negative_sequence=ids2fd;
for t=1:1:m
time = [time (t)*step];
fe=60;
thetaf = 2*pi*fe*time;
costhetaf =cos(thetaf(t));
sinthetaf =sin(thetaf(t));
Ke =[ 2*costhetaf      0                    0;
          -2*sinthetaf      0                    0;
           0            2*costhetaf          0;
           0            -2*sinthetaf         0;
           0            0          2*costhetaf;
           0            0          -2*sinthetaf];
```

```
ihelp_abcf= [iaf(t);
             ibf(t);
             icf(t)];

 helpdqf  = Ke*ihelp_abcf;
 helpdqfm=[helpdqfm helpdqf];
end
 iqaf=mean(helpdqfm(1,:));
 idaf=mean(helpdqfm(2,:));
 iqbf=mean(helpdqfm(3,:));
 idbf=mean(helpdqfm(4,:));
 iqcf=mean(helpdqfm(5,:));
 idcf=mean(helpdqfm(6,:));
  helpdqff=[iqaf;
                idaf;
                iqbf;
                idbf;
                iqcf;
                idcf];
 helpdq2ff = K1_2*helpdqff;
 ids2ffq=helpdq2ff(1,:);
 tp_Q_axis_positive_sequence= ids2ffq;
 ids2ffd= helpdq2ff(2,:);
 tp_D_axis_positive_sequence=ids2ffd;
  ids2ffq=helpdq2ff(3,:);
 tp_Q_axis_negative_sequence=ids2ffq;
 ids2ffd=helpdq2ff(4,:);
 tp_D_axis_negative_sequence=ids2ffd;
%delta_Q_negative=abs(Normal_Q_axis_negative_sequence-
tp_Q_axis_negative_sequence)
```

```
delta_D_negative=abs(Normal_D_axis_negative_sequence-
tp_D_axis_negative_sequence)
delta_Q_positive=abs(Normal_Q_axis_positive_sequence-tp_Q_axis_positive_sequence)
%delta_D_positive=abs(Normal_D_axis_positive_sequence-
tp_D_axis_positive_sequence)
```

The m2.m file integrates the power spectrum density with m1.m:

```
% intialize arrays:
time=[0];
idq2=[0;0;0;0;0;0];
%Input tabulated current data:
%The data are stored into a file, which is read by MATLAB

input_current_data_phase-a;
ia=input_current_data_phase-a;

input_current_data_phase-b;
ib=input_current_data_phase-b;

input_current_data_phase-c;
ic=input_current_data_phase-c;

step=1/RL;  % Step size
m=RL;       % Record length

for t=1:1:RL
time = [time (t)*step];
fe=60;      % frequency of stator (Hertz)
thetaf = 2*pi*fe*time;
costhetaf =cos(thetaf(t));
sinthetaf =sin(thetaf(t));
% Synchronous dq-phasor currents transformation:
```

```
Ke =[ 2*costhetaf      0                    0;
          -2*sinthetaf      0                    0;
          0                 2*costhetaf          0;
          0                 -2*sinthetaf         0;
          0                 0                    2*costhetaf;
          0                 0                    -2*sinthetaf];


% Positive- and negative-sequence currents transformation:
K1_2 =[ 1/3     0      -1/6          sqrt(3)/6     -1/6          -sqrt(3)/6;
              1/3     0      -sqrt(3)/6    -1/6          sqrt(3)/6     -1/6;
              1/3     0      -1/6          -sqrt(3)/6    -1/6          sqrt(3)/6;
              1/3     0      sqrt(3)/6     -1/6          -sqrt(3)/6    -1/6;
              1/3     0      1/3           0             1/3           0;
               0      1/3    0             1/3           0             1/3];

ihelp_abc= [ia(t);
            ib(t);
            ic(t)];
 helpdq  = Ke*ihelp_abc;
 helpdq2 = K1_2*helpdq;
 idq2=[idq2 helpdq2];
 ids2=idq2(4,:);
 end
% power Spectrum density of the fault indicator current (id):
x=ids2(1:RL);
window1=hamming(m);
noverlap1=m/2;
pwelch(x,window1,noverlap1,nfft,fs);
```